



Electron transfer reactions in trinuclear complexes and
redox active molecular monolayers

(Elektronentransferreaktionen in dreikernigen Komplexen und redox-
aktiven molekularen Monolagen)

Von der Fakultät für Mathematik und Naturwissenschaften
der Carl von Ossietzky Universität Oldenburg
zur Erlangung des Grades und Titels eines

Doktors der Naturwissenschaften (Dr. rer. nat.)
angenommene Dissertation

von Frau Aleksandra Marković, MSc.
geboren am 17. Mai 1991 in Užice, Serbia

Oldenburg, March 2019

This work was carried out from April 2015 to December 2018 at the Carl von Ossietzky University of Oldenburg, Faculty of Mathematics and Natural Science, Institute of Chemistry under the supervision of Prof. Dr. Gunther Wittstock. The research was enriched by different collaborations, particularly with Prof. Dr. Rüdiger Beckhaus and Jens Christoffers from the Institute of Chemistry as well as their PhD students Pia Sander and Leon Buschbeck. The project was part of the Graduate Programme "Nanoenergy" funded by the Ministry for Science and Culture of the State of Lower Saxony.

Gutachter: Prof. Dr. Gunther Wittstock

Zweitgutachter: PD Dr. habil. Izabella Brand

Tag der Disputation: 17.06.2019

“God made the bulk; surfaces were invented by the devil.”

Wolfgang Pauli

Abstract

In this thesis, electron transfer reactions were investigated in molecular systems with extended π -electron system that can serve as part of light harvesting devices. In the first part of the thesis redox activity and electronic transitions in absorption spectra of $[(\text{Cp}_2\text{Ti})_3\text{HATN}(\text{Ph})_6]$ complex were studied. This type of complex molecular systems are one of the model compounds that will eventually provide enough information about the synthesis of molecular systems that mimic electron transfer reactions with similar accuracy as in nature. This complex includes formally three titanocene(II) fragments. The voltammogram of $[(\text{Cp}_2\text{Ti})_3\text{HATN}(\text{Ph})_6]$ shows six oxidation and three reduction waves. Solution spectra of $[(\text{Cp}_2\text{Ti})_3\text{HATN}(\text{Ph})_6]$ and of the electrochemically formed oxidation products show electronic transition in the UV, visible and the NIR ranges. In the second part of the thesis, derivatives of 2,5-diaminoterephthalate (DAT) were investigated as redox-active molecules that can be functionalized with up to 4 effector groups. The electrochemical behaviour of seven DAT derivatives was studied by cyclic voltammetry in dichloromethane. In the absence of a proton donor, DATs should be oxidized in two one-electron steps. The first step is usually quasi-reversible while the second step is either quasi-reversible or irreversible. Some electrochemical properties such as the formal potentials and the ratio between the anodic and the cathodic current were determined from the cyclic voltammograms. Correlation between the formal potential of first oxidation and the absorption or the fluorescence emission wavelengths are established for this specific type of dyes. In the last part of the thesis four derivatives of DATs, which were functionalized with lipoic acid, were assembled on the Au surface together with 1-decanethiol or 1-hexanethiol. Interestingly, layers of two derivatives are not redox-active in the potential range of 0-0.9 V (SHE). However, by a potential excursion to 1.15 V and 1.10 V, the layer can be activated. Subsequently, they show a surface-immobilized redox couple ($E^\circ = 0.66$ V and 0.65 V). Slightly different mechanisms of electrochemical activation were proposed for two derivatives of the DATs which are in agreement with the spectroscopic analysis. The activation of the surfaces can enable binding of an effector groups. As demonstrated by the addition of 3-(trifluoromethyl)aniline and XPS analysis of the modified monolayers.

Zusammenfassung

In dieser Arbeit wurden Elektronentransferreaktionen in molekularen Systemen mit ausgedehnten π -Elektronensystemen untersucht, die als Lichtsammelinheiten dienen können. Im ersten Abschnitt der Arbeit wurden die Redox-Aktivität und elektronische Übergänge in Absorptionsspektren des $[(\text{Cp}_2\text{Ti})_3\text{HATN}(\text{Ph})_6]$ -Komplexes untersucht. Derartige komplexe, molekulare Systeme gehören zu den Modellverbindungen, die hinreichend Informationen über die Synthese von molekularen Systemen, die Elektronentransferreaktionen in der Natur imitieren, liefern können. Dieser Komplex beinhaltet formal drei Titanocen(II)-Fragmente. Das Cyclovoltammogramm von $[(\text{Cp}_2\text{Ti})_3\text{HATN}(\text{Ph})_6]$ weist sechs Oxidations- und drei Reduktionssignale auf. Spektren von gelöstem $[(\text{Cp}_2\text{Ti})_3\text{HATN}(\text{Ph})_6]$ und dessen elektrochemisch gebildeten Oxidationsprodukte zeigen elektronische Übergänge im UV, sichtbaren und NIR-Bereich. Im zweiten Teil der Arbeit wurden Derivate des 1,2-Diaminoterephthalats (DAT) als redox-aktive Moleküle, die mit bis zu vier Effektorgruppen modifiziert werden können, untersucht. Das elektrochemische Verhalten von sieben DAT-Derivaten wurde mit zyklischer Voltammetrie in Dichlormethan studiert. Ohne einen Protonendonor sollten DATs in Zweielektronenschritten oxidiert werden. Während der erste Schritt gewöhnlicherweise quasi-reversibel ist, ist der zweite Schritt entweder quasi-reversibel oder irreversibel. Elektrochemische Eigenschaften, wie die Formalpotentiale und das Verhältnis anodischer und kathodischer Ströme, wurden aus den Cyclovoltammogrammen bestimmt. Das Formalpotential der ersten Oxidation dieser Farbstoffe konnte mit den Absorptions- oder Fluoreszenzemissionswellenlängen korreliert werden. Im letzten Teil dieser Arbeit wurden vier DAT-Derivate, welche mit Liponsäure funktionalisiert wurden, auf einer Goldoberfläche zusammen mit 1-Decanthiol oder 1-Hexanthiol assembliert. Zwei dieser Schichten sind im Potentialbereich von 0.9-1.1 V (vs. SHE) nicht redox-aktiv, können jedoch bei einem Potentialscan bis 1.15 V bzw. 1.10 V aktiviert werden. Folglich weisen sie ein an der Oberfläche immobilisiertes Redox-Paar auf ($E^{\circ'} = 0.66$ V und 0.65 V). Geringfügig unterschiedliche Mechanismen für die elektrochemische Aktivierung wurden in Übereinstimmung mit den spektroskopischen Daten für zwei DAT-Derivate postuliert. An die durch Oxidation aktivierten DAT-Monolagen kann ein Effektor aus der Lösung mittels Additionsreaktion gekoppelt werden, wie am Beispiel von 3-Trifluoromethylanilin und der XPS-Analyse der modifizierten Monolagen demonstriert werden kann.

Acknowledgement

My special thanks to Prof. Dr. Gunther Wittstock for providing me an interesting research topic and supervision of my work. His comprehensive critical discussions, great insight and encouragement have contributed significantly to the success of this work. I would like to thank PD Dr. habil. Izabella Brand for accepting the position of second examiner.

I would like to thank Prof. Dr. Rüdiger Beckhaus and Prof. Dr. Jens Christoffers and their PhD students Pia Sandler and Leon Buschbeck for synthesis of compounds used in this thesis as well as the detailed and rigorous analysis and good ideas during our collaboration. Also, I would like to thank Prof. Dr. Thorsten Klüner for the in-depth and critical discussions and good suggestions.

My gratitude also goes to PD Dr. habil. Carsten Dosche for the support with spectroelectrochemical setup and interpretation of spectra (UV-vis-NIR and XPS) and PD Dr. habil. Izabella Brand for the support with the PM IRRAS setup and the interpretation of spectra.

I would like to acknowledge my colleagues and friends, who were always there when I needed them and who contributed to a wonderful working atmosphere and brought me to new ideas through professional discussions.

My thanks also go to my Nanoenergy project partners for their willingness to intensively discuss my research findings and for offering me a deep insight into their research.

I would like to express deep appreciation to my family for the unconditional support without which my studies and this work would not have been possible.

I am also grateful to the Ministry for Science and Culture of the State of Lower Saxony for funding the project.

Table of content

1	INTRODUCTION	1
2	APPLIED CHARACTERIZATION TECHNIQUES FOR EXTENDED π-SYSTEMS	5
2.1	COMPONENTS OF ELECTROCHEMICAL CELL	5
2.2	VOLTAMMETRY	6
2.2.1	<i>Cyclic Voltammetry</i>	7
2.2.2	<i>Differential pulse voltammetry</i>	10
2.3	SIGNATURES OF ELECTROCHEMICAL REACTION MECHANISMS IN VOLTAMMOGRAMS	12
2.3.1	<i>EE and EEE mechanism</i>	12
2.3.2	<i>Mechanisms with coupled chemical reactions</i>	13
2.4	SPECTROELECTROCHEMISTRY	16
2.4.1	<i>Experimental setup</i>	16
2.4.2	<i>Electronic transitions in multinuclear metal complexes</i>	16
3	ASSEMBLY OF MOLECULES ON SURFACE	19
3.1	CHEMICALLY MODIFIED ELECTRODES AND SELF-ASSEMBLED MONOLAYERS (SAMs)	19
3.2	ELECTROCHEMISTRY OF SAMs	22
3.2.1	<i>Voltammetry of SAMs</i>	22
3.2.2	<i>Electrochemical modification of the surfaces</i>	24
3.3	X-RAY PHOTOELECTRON SPECTROSCOPY	28
3.3.1	<i>Basic principle</i>	28
3.3.2	<i>Binding energy</i>	30
3.3.3	<i>Photo electron intensities</i>	32
3.3.4	<i>Splitting of the energy levels</i>	34
3.3.5	<i>Radiation damage</i>	36
3.3.6	<i>Quantification of XP spectra</i>	39
3.4	PM IRRAS OF SAMs	39
3.4.1	<i>Principle</i>	40
4	EXPERIMENTAL DETAILS	45
4.1	CHEMICALS	45
4.2	ELECTROCHEMICAL MEASUREMENTS	47
4.2.1	<i>Electrochemical measurements of the trinuclear titanium complexes</i>	47
4.2.2	<i>Electrochemical measurements of DATs in solution</i>	47
4.2.3	<i>Determination of formal potentials</i>	47
4.2.4	<i>Electrochemical measurements on surfaces</i>	48
4.2.5	<i>Spectroelectrochemistry</i>	48
4.2.6	<i>Absorption and fluorescent spectroscopy of DATs</i>	49
4.3	GENERAL CLEANING PROCEDURE	49
4.4	PREPARATION OF GOLD SURFACES	50
4.5	PREPARATION OF SAMs	50
4.6	CHARACTERIZATION OF SURFACES	50
4.6.1	<i>X-ray photoelectron spectroscopy (XPS)</i>	50
4.6.2	<i>Polarization modulation infrared reflection adsorption spectroscopy (PM IRRAS)</i>	51
5	ELECTROCHEMICAL AND SPECTROELECTROCHEMICAL STUDIES ON ELECTRON TRANSFER REACTIONS OF $[(\text{Cp}_2\text{Ti})_3\text{HATN}(\text{PH})_6]$	52
5.1	ELECTROCHEMICAL STUDIES OF $[(\text{Cp}_2\text{Ti})_3\text{HATN}(\text{PH})_6]$	52
5.2	SPECTROELECTROCHEMICAL MEASUREMENTS	55
6	ELECTROCHEMICAL AND SPECTROSCOPIC CHARACTERIZATION OF DATS IN THE SOLUTION	62

6.1	ELECTROCHEMISTRY OF DATS	62
6.2	FLUORESCENCE AND UV-VIS SPECTROSCOPY OF DATS	72
7	SELF-ASSEMBLED MONOLAYERS OF DATS ON ELECTRODE SURFACE.....	75
7.1	ELECTROCHEMICAL ACTIVATION OF SAMs	75
7.2	SURFACE SPECTROSCOPIC CHARACTERIZATION	81
7.3	ELECTROCHEMICAL CHARACTERIZATION OF DAT DERIVATIVES WITH A FLUORINATED PROTECTING GROUP.....	94
7.4	SPECTROSCOPIC CHARACTERIZATION OF SURFACES.....	98
7.5	ADDITION REACTION ON SURFACE	106
8	SUMMARY AND OUTLOOK.....	109
8.1	SUMMARY OF INVESTIGATED SYSTEMS.....	109
8.2	CONCLUSION AND OUTLOOK	112
9	APPENDIX	114
10	OWN PUBLICATIONS AND CONFERENCE CONTRIBUTIONS	118
10.1	PUBLICATIONS	118
10.2	ORAL PRESENTATIONS IN NATIONAL AND INTERNATIONAL CONFERENCES	118
10.3	POSTERS IN NATIONAL AND INTERNATIONAL CONFERENCES	119
11	CURRICULUM VITAE.....	120
	PERSONAL DATA.....	120
	SCHOOL/STUDY/SCIENTIFIC QUALIFICATION.....	120
	SCIENTIFIC EMPLOYMENT WITHIN THE UNIVERSITY.....	120
	AWARDS.....	121
	OWN PARTICIPATION IN TEACHING.....	121
	OFFICES IN ACADEMIC SELF-ADMINISTRATION WITHIN THE UNIVERSITY	121
12	REFERENCES	122

1 Introduction

The electron transfer reactions are one of the most fundamental among all chemical transformations [1]. They are a crucial part of biological processes [1], like photosynthesis [1–3], organic synthesis [4], and occur in devices for energy storage [5], or in energy sources [6], etc. Because of its great importance, electron transfer reactions were the subject of numerous experimental studies devoted to mimic electron transfer processes in chemical [1] and biological [2] systems in the past few decades. In these studies, experimental results have been gathered on phenomena like reactions between molecules and electrodes [1], charge transfer spectra [7], photo induced electron transfers [8], chemiluminescent electron transfers [9], electron transfer through solid state [10] and electron transfer through thin films of molecular monolayers on electrodes [11].

Despite those efforts, many areas are not completely understood or cannot be controlled with sufficient precision in artificial systems.

Energy conversion from photons to electrons is nearly perfect in efficiency in biological systems such as photosynthesis, while artificial systems are nowhere near that efficiency. Understanding the mechanism of electron and energy transfers in natural light-harvesting systems can help develop highly efficient photovoltaic devices and artificial photosynthesis systems [12]. Also, energy conversion in biological light harvesting systems depends on structure and supramolecular orientation of molecular building blocks and can be influenced significantly by design of optimized building blocks. Because of this there is the necessity in developing new building blocks in science that can be part of highly efficient artificial light harvesting systems.

In the last few years, a variety of synthetic approaches have been developed for combining multiple light-absorbing and redox-active centres for developing homogeneous photocatalysts for multi-electron redox processes [13]. While good understanding has been deployed to study the electronic excited states in mononuclear complexes, obtaining a clear picture of the multinuclear complexes in the same manner is more complicated. The spectroscopic properties of those entities are more complicated

mainly because of the different metal sites and the charge transfer between those sites and the ligand.

In the first part of the thesis the electron transfer reactions were studied in the multinuclear transition metal complexes. The era of multinuclear transition metal complexes started with the work of Creutz and Taube [14] on mixed-valence compounds. They showed that the complexity of processes at binuclear complexes is conceptually similar to electron transfer reactions that happen in nature [3]. While a systematic understanding of the photochemical and electrochemical behaviour has been obtained for binuclear complexes [15–18], much less is known about trinuclear complexes [19]. Trinuclear complexes can be synthesized by using hexaazatriphenylene (HAT) [20], hexaazatrinaphthylene (HATN) ligands [21] or their backbone-substituted derivatives [22]. In this thesis the hexaphenyl substituted isomer (HATNPh₆) and the corresponding titanocene complex have been investigated [23].

This type of trinuclear transition metal complexes are particularly interesting for investigation because they have bridging ligands with extended π -acceptor properties [22]. This type of complexes have been intriguing for supramolecular building block studies because the ligands have three chelating sites for metal ions [22]. Secondly, the ligands have electron-deficient π -systems which encourages charge transfer between metal centres of the complex and/or metal-to-ligand charge transfer [22]. Thirdly, the C₃ symmetry axis is responsible for degeneration of π^* orbitals [22]. Fourthly, the ligands chemical and physical properties can be altered by modifying their substituent groups thereby changing their electronic structure of the ligand [22].

HAT, HATN and its derivatives also belong to the family of non-innocent ligands (ligands that are redox-active) [13]. One of the essential properties of the ligands is their capability to act as electron reservoirs, which allows electron transport from the metal to the ligand and the other way round [24]. This ability of the ligand is of great interest for the design of new homogeneous catalysts because many transformations involve the transfer of several electrons between the catalyst and the activated substrate. These transformations are common for noble metals such as Pd, Pt, Rh, etc. which are expensive, but almost impossible to achieve with cheaper and more abundant first-row transition metals. Non-innocent ligands actually allow first-row transition metals to mimic the catalytic properties of more noble metals [25–28].

Because of multifunctionalities of HAT, HATN and its derivatives, their metal complexes have opened up a new field of HAT-based trinuclear compounds [22]. Complexes with ruthenium [29], rhenium [30], cobalt [13] and titanium [19] have been investigated due to their interesting electrochemical, photophysical and magnetic properties.

In this thesis the redox properties and intramolecular charge transfer processes of the trinuclear titanium complexes with hexaphenyl-5,6,11,12,17,18-hexaazanaphthylene have been investigated [31]. The electrochemical results have been obtained by cyclic voltammetry and differential pulse voltammetry. Spectroscopic results of different oxidation states of the complex were obtained in this thesis by using spectroelectrochemistry in the ultraviolet (UV), visible (vis) and near infrared (NIR) spectral regions.

In the second part of the thesis the focus is on the surface modification of electrode with complex molecular monolayers and electron transfer reactions of those layers. In the recent years interest in surface (electrode) modification has led to the study of electron transfer using electrodes modified with molecular monolayers [32–35]. The molecular monolayers provide an excellent platform for surface modification and electrochemical systems to study electron transfer processes [36–41]. The advantages of this method include the substantial ordering that such chemisorbed layers can exhibit and the ability to control the distance between the electrode and the redox centre. Due to the biological importance in photosynthesis, the redox properties of thiol-functionalized redox-active molecules immobilized on gold electrodes have received increasing attention in recent years [40].

The modification of surfaces on a molecular level raised interest significantly in the last century [40]. Self-assembly of monolayers become a particularly attractive method for surface modification because of the simplicity of the surface modification step [42]. At the beginning modification of surfaces was only used to change physical properties of the surfaces (contact angle, wettability...) [43, 44]. From that time until present day, surface modification evolved to more and more complex layers. Today, not only physical surface properties and associated functionalities can be modified,

monolayers can be used as platform for studying electron transfer reactions or as anchor for attaching surface molecular devices that can be used for different purposes, commonly called today integrated molecular systems [40]. These molecular systems are mainly used for pH [45–47], inorganic [48–50], organic and biosensors [38, 39, 51].

In this thesis derivatives of 2,5-diaminoterephthalate (DAT) were assembled on electrode surfaces with self-assembly technique. The common structural motif of this class of compounds is a chromophore with two carboxylates and two amino groups. These compounds are obtained by reactions of succinyl succinates with amines, followed by aerobic oxidation [52]. Most DATs are deeply orange to red coloured compounds [53, 54] which usually exhibit strong fluorescence [55]. As consequence of their easy functionalization, this type of compounds found application in life science and material science [52]. However, they have never been assembled on an electrode surface before.

Of great interest is the possibility to functionalize chromophore with up to four different effector groups [52]. DATs can be functionalized with the fullerene (C_{60}) by cycloaddition reaction. Few dye-fullerene conjugates, called dyads, have been synthesised [56–60]. This dyads have been created with the purpose to mimic the photoinduced electron and energy transfer processes that occur in photosynthesis [61–63].

Firstly, electrochemical behaviour of DATs with different functional groups was investigated in order to find the best functionalized structure for assembly on electrode surface. Four different DATs with lipoic acid as one of the functional groups were assembled on the surface by self-assembly. Than electrochemical investigations were carried out using cyclic voltammetry. The surfaces were characterized with surface sensitive techniques like X-ray photoelectron spectroscopy (XPS) and polarization modulation infrared reflection-absorption spectroscopy (PM IRRAS). This system was investigated as good platform for molecular devices such as electrochemically controlled sensors, or as platform for investigation of electron transfer reactions in integrated systems for light harvesting.

2 Applied characterization techniques for extended π -systems

Electroanalytical methods provide information about electron transfer reactions in a molecular system with high specificity and selectivity. The detection limit is also low [64]. Chapter 2.1 covers components of the electrochemical cell. Basic electrochemical methods that are used for characterization of the extended π -systems will be introduced in Chapter 2.2. Signatures of electrochemical mechanisms in the voltammograms are discussed in Chapter 2.3. Furthermore, electrochemistry can be combined with other characterization methods. Chapter 2.4 covers the combination of electrochemical and spectroscopic methods.

Electrochemistry is a branch of chemistry that studies interrelation of chemical and electrical processes [64]. Modern electrochemistry started in 18th century when the first electrochemical experiment was conducted by Luigi Galvani [65, 66], in which he established the relation between electricity and chemical reaction in his famous experiment with the frog. Around the same time Alessandro Volta developed the “voltaic pile”. In the following years electrochemistry was developed for more practical purposes, such as power source and for metal plating.

In this thesis the reactions that are happening at electrodes in electrochemical systems are commonly called the redox reaction. These reactions can be enforced by the application of an external voltage.



where O is the oxidized species and R is the reduced species.

2.1 Components of electrochemical cell

Most electrochemical measurements are performed in specifically designed electrochemical cells. Depending of the type of the measurement and the measured

system, there is a variety of electrochemical cells. The simplest cell is a glass beaker where three electrodes are immersed in electrolyte solution:

1. The working electrode (WE) - this is electrode at which the electrochemical reaction of interest is observed. It can be made of inert metals like gold or platinum, carbon-based materials like glassy carbon, pyrolytic carbon or it can be a mercury drop.
2. The reference electrode (RE) - has a constant and well-known electrode potential that is not affected by the electrolysis current. Most commonly, silver chloride or calomel electrodes are used as reference electrodes for aqueous solution. For non-aqueous solution, pseudo-reference electrodes or Ag/Ag^+ is used. These electrodes do not have a known potential. Moreover, it varies with the measured system. The relation to the thermodynamic electrochemical scale is found by measuring the potential of the electron transfer between ferrocene (Fc) and the ferrocenium (Fc^+). The standard redox potential of this couple is 0.40 V vs. SHE and assumed to depend little on the solvent [67].
3. The counter electrode (CE) or auxiliary electrode (Aux) - is used for carrying the current flow through the cell. Usually, it has a large surface area and is made of well conductive and inert material like platinum. Typically, the reaction at that electrode is not known and it may involve solvent electrolysis.

The choice of the electrodes mostly depends on the nature of the investigated systems. In addition, some other parameters of the measurement need to be adjusted like the choice of the most suitable electrochemical technique, electrochemical cell, appropriate solvent, supporting electrolyte, pH, temperature etc.

2.2 Voltammetry

In a voltammetric experiment a potential program is applied between the working and the reference electrode and the resulting current is measured between the working and auxiliary electrode. The current in the electrochemical cell results from two different processes:

1. Faradaic current - The signal is caused by redox reaction (electrolysis) of the analyte in the solution, which can be described by Faraday's law.
2. Non-Faradaic signal - The signal is caused by other effects like charging of the electrical double layer of the electrode adsorption, desorption or reorientation.

2.2.1 Cyclic Voltammetry

In cyclic voltammetry (CV), a triangular potential programme $E_1-E_2-E_1$ (Fig. 1b) is applied between the working and the reference electrode, while the current is followed between working and auxiliary electrode. When the potential is swept only from value E_1 to E_2 (Fig. 1a) it is called linear sweep voltammetry (LSV). Typically, the data are plotted in diagrams called cyclic voltammograms where the potential is plotted on the abscissa and the current on the ordinate. Oxidation or reduction of the electrochemically active species are recorded as a current peak at the specific potential which corresponds to the potentials, at which species are oxidized or reduced. A typical cyclic voltammogram is shown in Fig. 2.

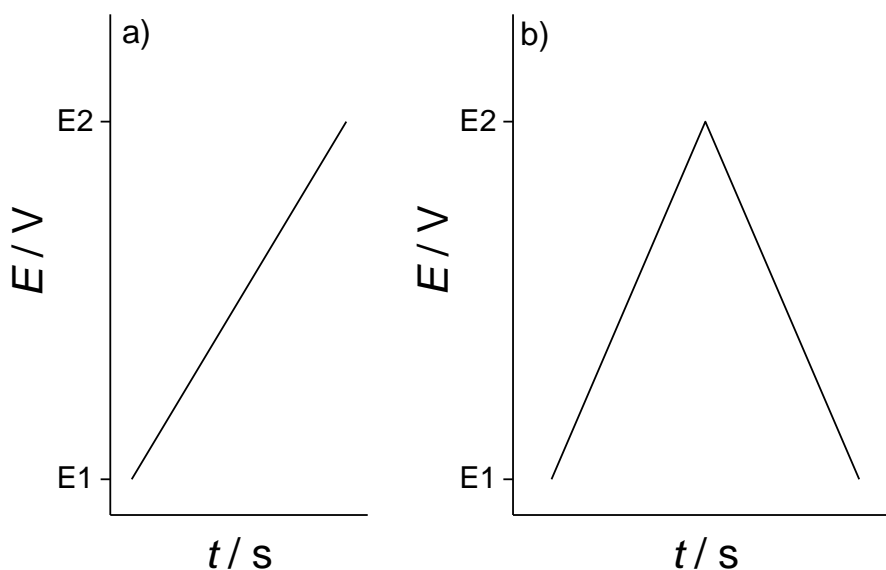


Fig. 1: Potential program for a) linear sweep voltammetry where the potential is swept from value E_1 to E_2 and b) cyclic voltammetry where the potential is swept from value E_1 to E_2 and back to E_1 .

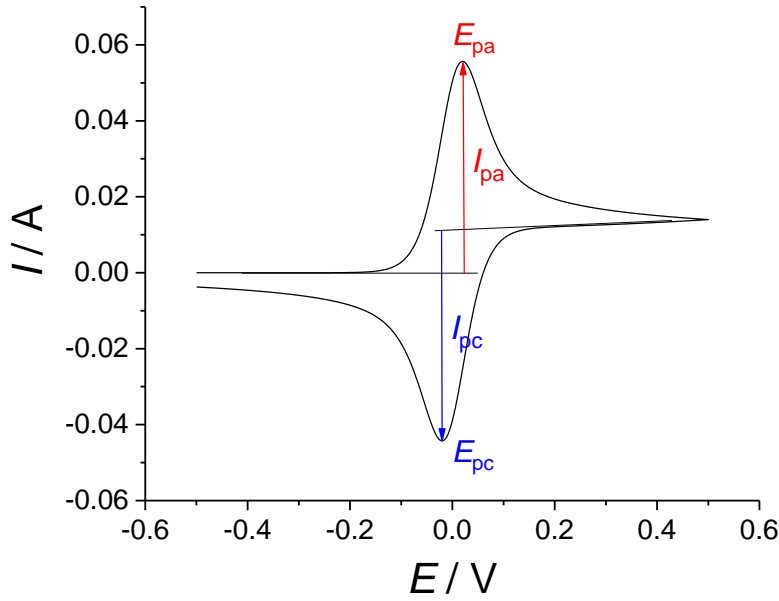


Fig. 2: Cyclic voltammogram of a reversible reaction where E_{pc} and E_{pa} are the cathodic and the anodic peak potentials, I_{pc} and I_{pa} are the cathodic and the anodic peak current (simulated cyclic voltammogram).

The cyclic voltammogram of a reversible electrochemical reaction can be characterized with following parameters:

1. Formal potential can be calculated as arithmetic mean between the anodic E_{pa} and the cathodic E_{pc} potential:

$$E^{o'} = \frac{E_{pa} + E_{pc}}{2} \quad (2)$$

2. Separation between two peak potentials is expected for a reversible redox couple as:

$$\Delta E_p = E_{pa} - E_{pc} = 2.218 \frac{RT}{nF} \quad (3)$$

Here, R is the gas constant ($R = 8.314 \text{ J}\cdot\text{mol}^{-1}\cdot\text{K}^{-1}$), T is the temperature (K), n is the number of electrons involved in the Faradaic reaction and F is the Faraday constant ($F = 96485 \text{ A s mol}^{-1}$). The peak separation is ca. 57 mV when $n = 1$ and $T = 298 \text{ K}$.

3. The ration between the anodic I_{pa} and the cathodic I_{pc} current is equal to one:

$$\left| \frac{I_{pa}}{I_{pc}} \right| = 1 \quad (4)$$

Peak current I_p is proportional to square root of scan rate $\nu^{1/2}$, and is described by the Randles-Sevcik equation:

$$I_p = 0.4463nFcA \left(\frac{nF\nu D}{RT} \right)^{1/2} \quad (5)$$

where c is the bulk concentration (mol cm^{-3}), A is the electrode surface area (cm^2), ν is the scan rate (V s^{-1}), D is the diffusion coefficient ($\text{cm}^2 \text{s}^{-1}$) and I_p is the peak current (A).

Electrochemical reactions can also be irreversible or quasi-reversible. Criteria for all three types of reactions can be determined from cyclic voltammogram as summarized in Tab. 1.

Tab. 1: Criteria for reversible, irreversible or quasi-reversible electrochemical reaction

Reversible	Quasi-reversible	Irreversible
$I_{pa}, I_{pc} \sim \nu^{1/2}$		$I_{pa}, I_{pc} \sim \nu^{1/2}$
$ I_{pa} / I_{pc} = 1$	$ I_{pa} / I_{pc} = 1$	No reversible peak
$\Delta E_p = 59\text{mV}/n$ ($T = 298\text{ K}$)	$\Delta E_p = f(\nu)$	

In some cases, the baseline for determining the reverse peak current cannot be determined. Nicholson [68] suggested that for determining the ratio I_{pa}/I_{pc} and I_{pc} value first $I_{pc,0}$ (the uncorrected cathodic peak currents to the zero-current baseline) should be used. and the current I_λ at E_λ (the vertex potential) as described in the following equation and shown in Fig. 3:

$$\frac{|I_{pc}|}{|I_{pa}|} = \frac{|I_{pc,0}|}{|I_{pa}|} + \frac{0.485 I_\lambda}{|I_{pa}|} + 0.086 \quad (6)$$

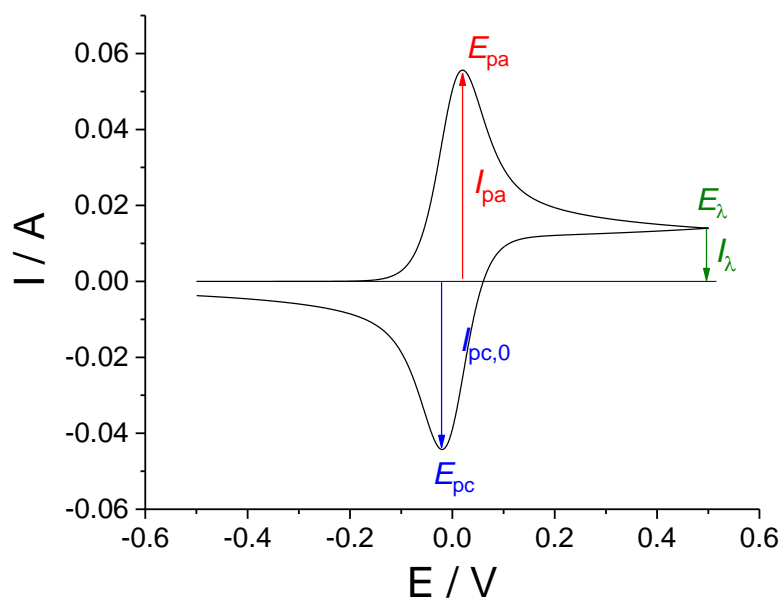


Fig. 3: Determination of the cathodic peak current I_{pc} using $I_{pc,0}$, the uncorrected cathodic peak currents to the zero-current baseline and current I_{λ} at E_{λ} (simulated cyclic voltammogram).

2. 2. 2 Differential pulse voltammetry

Differential pulse voltammetry (DPV) is an electrochemical method derived from staircase voltammetry, which is useful to detect trace levels of organic and inorganic analytes. A series of rectangular voltage pulses is superimposed on the potential stairsteps (Fig. 4). The current is measured twice immediately before each pulse t_1 and at the end of the pulse t_2 . The current at t_1 is instrumentally subtracted from current at t_2 . This current difference ΔI is plotted as a function of staircase potential. Typical differential pulse voltammogram is shown in Fig. 5. DPV has a better potential resolution than CV and can be detected down to concentration of $10^{-8} \text{ mol dm}^{-3}$ [69].

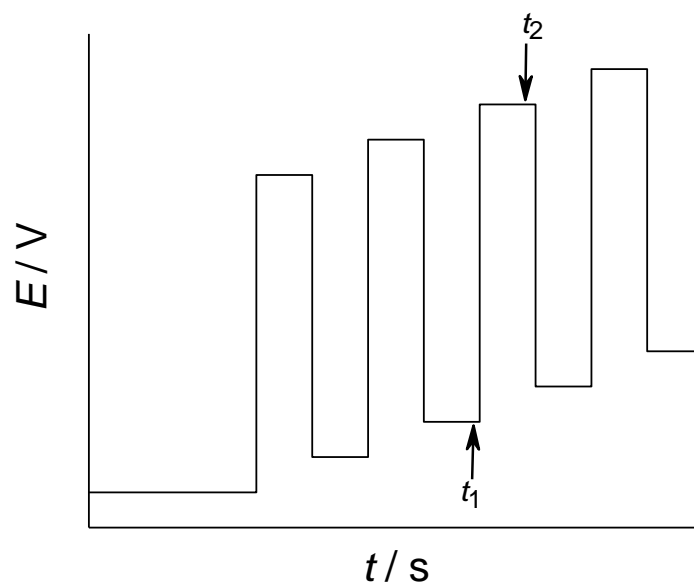


Fig. 4: Potential program for differential pulse voltammetry where with t_1 is marked first current sample (immediately before each pulse) and with t_2 second current sample (the end of the pulse).

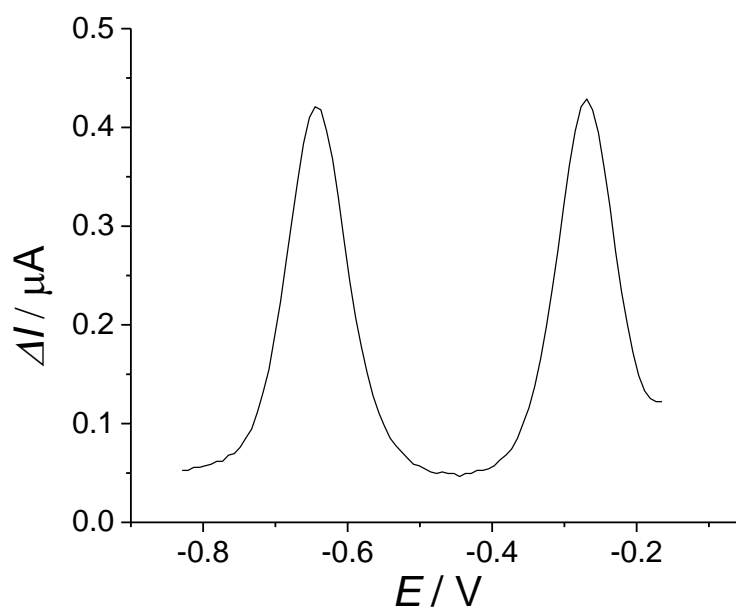


Fig. 5: Differential pulse voltammogram of 0.3 mM $[(Cp_2Ti)_3HATN(Ph)_6]$ at an Au working electrode in 0.2 M $TBAPF_6$ in THF.

2.3 Signatures of electrochemical reaction mechanisms in voltammograms

2.3.1 EE and EEE mechanism

In Chapter 2.2 only reaction with the transfer of one electron were considered. This is commonly called E reaction mechanism. In the electrochemical measurements more than one electron can be transferred in consecutive one electron transfers reactions from/to one molecule. This mechanism is called EE when two electrons are transferred, EEE for three electrons, etc. In Fig. 6 a cyclic voltammogram is shown for an oxidation according to the EEE mechanism.

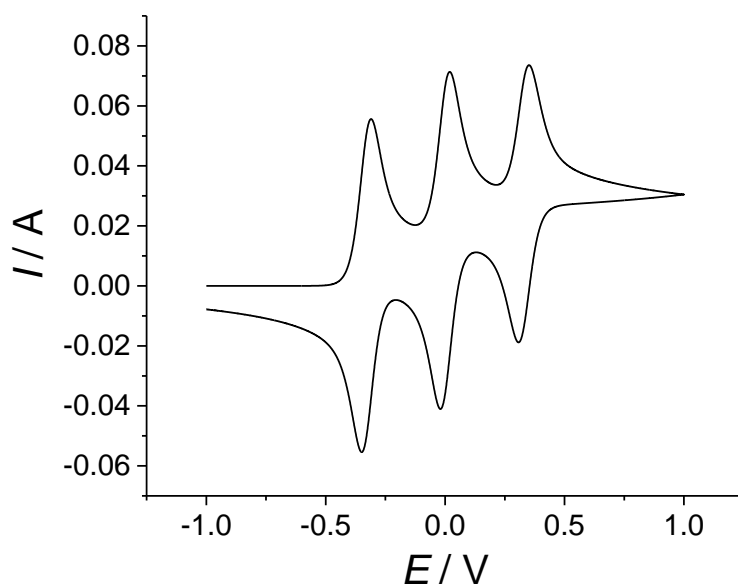


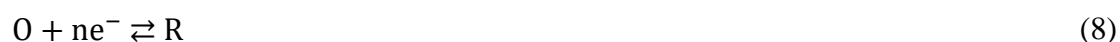
Fig. 6: Simulated cyclic voltammogram of the EEE mechanism where three electrons are transferred in consecutive one electron transfers.

Fullerenes [70] and the multi-nuclear transition metal complexes are examples of molecules that have many consecutive one-electron transfer reactions. Ghuamaan and co-authors have shown that trinuclear bis(2,4-pentanedionato)ruthenium complexes with substituted diquinoxalino[2,3-a:20,30-c]phenazine ligands can have between six and seven one electrons transfers depending on the chemical modification of the ligand [29]. Piglosiewicz and co-authors found eight electron transfers in trinuclear 5,6,11,12,17,18-hexaazatrinamethylene (HATNMe₆)-bridged titanium complexes [19].

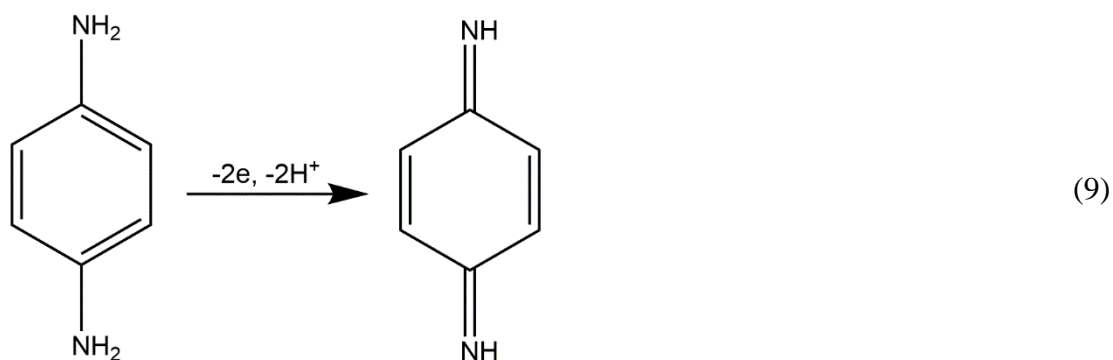
2.3.2 Mechanisms with coupled chemical reactions

Electrochemical electron transfer processes can be perturbed by a chemical reaction (C) that occurs in the solution close to the electrode. By coupling the electron transfer of the electrode with chemical reactions, an electrochemical reaction becomes a complicated electrode reaction. As a consequence, the concentration of reacting species on the surface of an electrode is changed. Numerous examples can be found in literature where electrochemical reactions are coupled with chemical reaction steps. These processes can be described with mechanisms such as CE, EC, ECE, and ECEC [71–76]. The solution composition (solvent, electrolyte ions, impurities or deliberately added compounds) exerts a large influence on the mechanism of electron transfer and coupled chemical reaction step.

The CE mechanism describes a process where a chemical reaction precedes the electrochemical reaction. The mechanism of CE reaction can be described as:



This is typical for electrochemical reactions happening in acidic aqueous electrolyte where $\text{pH} = 0$. The behaviour of *N,N*-dimethyl-*p*-phenylene-diamine in $\text{pH} = 0$ is an example for this mechanism, where firstly the molecule undergoes protonation followed by 2-electron, 2-proton oxidation [72]. *N,N*-dimethyl-*p*-phenylene-diamine is a derivative of *p*-phenylenediamine (PPD), this family of compounds should have a similar electrochemical behaviour as DATs which are investigated in Chapter 6. In neutral aqueous solution PPD undergoes one 2-electron, 2-proton oxidation described by reaction (9) [74–76]:



Interestingly N,N-dimethyl-p-phenylene-diamine changes its mechanism of electrochemical oxidation in aqueous solution when the pH of the solution is changed. In pH from 3-6, oxidation can be described by the EE mechanism. In cyclic voltammogram one can see two peaks which represent two one-electron transfer steps [72].

In basic solution this compound is oxidized in one step 2-electron, 2-proton oxidation. After the oxidation, the product is hydrolysed to the quinone-imine [72]. This process is a typical example of ECE mechanism, in which after electrochemical reaction, chemical reaction occurs, and the product of the chemical reaction can be electrochemically oxidized and reduced. The redox-active product of the chemical reaction is oxidized or reduced at a different potential than the starting compound. The ECE mechanism can be described as:



The ECE mechanism can be employed for the addition reaction of molecular species onto oxidized product of redox-active compound [73–76]. For example, 4-methyl-1,2-benzoquinone is generated electrochemically, the oxidized compound performs 1,4-addition reaction with amines in acidic solution (0.1 M HClO₄). The product of the chemical reaction is electrochemically active [73]. The cyclic voltammogram of an ECE mechanism is shown in Fig. 7. In the first scan of the cyclic voltammogram, the reduction peak is smaller than the oxidation peak because O is chemically converted to Z on the surface and it cannot be converted to R. In the first cycle one can see another reduction peak appearing at different potential value because Z, the product of chemical reaction, is electrochemically reduced to Y. In the second scan oxidation of Y to Z can be seen, as well as oxidation of R to O because diffusion resupplies R to the electrode surface.

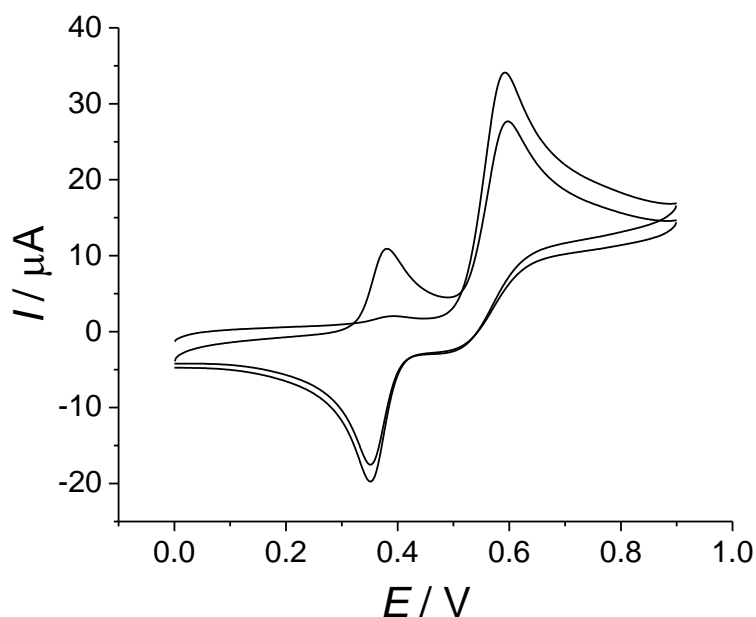


Fig. 7: Cyclic voltammogram of ECE mechanism (0.1 mM 4-methyl-1,2-benzoquinone in 0.1 M HClO₄ as supporting electrolyte on GC working electrode with 1 mM amionbenzoic acid as nucleophile).

Compton and co-authors [75] used the ECE mechanism to investigate electrochemically induced reaction of N,N'-diphenyl-p-phenylenediamine (DPPD) and sodium sulphide in aqueous solutions (pH 1–7). The DPPD forms a thin film on the electrode surface capable of an addition reaction with sulphide. Firstly, the DPPD film is oxidized in one 2-electron, 2 proton step. The oxidized compound undergoes 1,4-addition reaction with sulphide. The product of the chemical reaction is electrochemically active.

The EC mechanism describes a reaction, where electrochemical modification is followed by a chemical reaction, but the product is not electrochemically active:



The cyclic voltammogram of this mechanism will display a smaller reverse peak similar to the ECE mechanism. Because Z is not electrochemically active, the second reduction peak does not appear in the cyclic voltammogram of the EC reaction.

From all said above, one can conclude that cyclic voltammetry can be used to study intermediate, unstable and exotic species.

2.4 Spectroelectrochemistry

2.4.1 Experimental setup

The term *spectroelectrochemistry* is used in general for spectroscopic methods conducted simultaneously with electrochemical experiments. The ability to follow the transformation of chemical species over the course of a reaction time is a crucial aspect for the study of chemical dynamics or characterization of electrochemically oxidized and reduced species which cannot be synthesized as stable compounds by bulk synthesis. Frequently, the electrochemical and the spectroscopic measurements are done in the same cell. The setup used in this thesis has an optically transparent working electrode, through which a light beam is passed. Examples are glass coated with layer of indium-doped tin oxide (ITO) which is optically transparent but electrochemically conductive, or metal grid electrode that transmits the optical beam (Fig. 8).

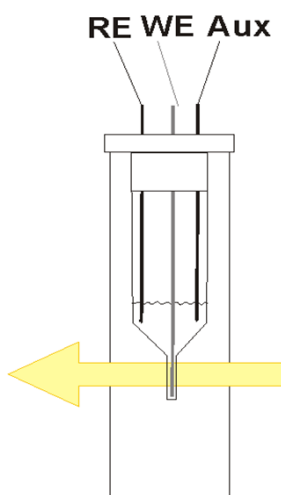


Fig. 8: Scheme of the spectroelectrochemical cell: WE - optically transparent working electrode, RE - reference electrode, CE - counter electrode, yellow arrow - path of light beam.

2.4.2 Electronic transitions in multinuclear metal complexes

In the UV-vis and NIR regions, electronic transitions can be observed in transition metal ions coordinated in complexes of widely varying structure and complexity. For transition metal complexes that involve the HATN systems, which are studied in this thesis, ligand field transitions and charge transfers can be observed in this spectral region.

Most intra-ligand (also called ligand-centred) transitions will also occur upon coordination of the ligand to the metal centres, although their energies may be somewhat

perturbed, and the rates of intersystem crossing may be strongly affected by the metal centre due to the heavy atom effect. Examples of intra-ligand transitions are $\pi \rightarrow \pi^*$ or $n \rightarrow \pi^*$ transitions.

There are few types of charge transfers characteristic for these compounds: charge transfer between the ligand and the metal centre (LMCT), charge transfer between the metal centre and the ligand (MLCT) or - in the case of multinuclear complexes - between various metal centres. If the participating metal centres have different oxidation states, this transfer is equal to an intervalence charge transfer (IVCT).

LMCT. This type of transition occurs from an occupied, low-lying, ligand-localised orbital to a vacant orbital of the metal centre. It is most common if the metal centre is highly oxidized, and the ligand is a strong electron donor.

MLCT. This type of transitions is common when the metal centre has a relatively low oxidation potential, and a relatively low-lying vacant molecular orbital is localised on the electron-accepting ligand. Thus, the metal centre acts as an electron donor, and the ligand as an electron acceptor, to give a charge-transfer excited state with an oxidized metal centre and a reduced ligand.

IVCT. Intervalence charge transfer is an electron transfer between two metal centres that differ in oxidation states. Often this type of the electron transfer reverses the oxidation states of the centres. The phenomenon is observed in mixed-valence bi-, tri- and polymetallic coordination complexes. The IVCT band is usually broad and observed in UV-vis and NIR region of the spectral region. The strength of electronic interaction between the metal centres can be determined by analysis of the IVCT band [77]. The mixed valence complexes can be classified by Robin–Day classification into three groups:

1. Class I - there is no interaction between the metal centres. The IVCT band is not observed.
2. Class II - there is intermediate interaction between the metal centres. The IVCT band is observed in the spectra. The oxidation states of the two metal centres

are distinct, but they interchange. This represents the most common class of mixed valence complexes.

3. Class III - there is very strong interaction between the metal centres. Usually these metal centres are considered one unit. The IVCT band is observed. The oxidation states of the two metal centres are equivalent.

3 Assembly of molecules on surface

3.1 Chemically modified electrodes and self-assembled monolayers (SAMs)

In the last century, the interest for developing chemically modified electrodes (CMEs) was stimulated by the success of the first amperometric biosensors [11, 78]. CMEs can be modified by adsorbing, coating or attaching specific molecules on electrode surface. Today this method allows modification of electrodes for sensitive and selective analytical application [36] in electrochemistry and for devices of molecular electronics [79]. Over time, a variety of methods for modification of electrodes became available [80].

One of the most popular methods for modification of electrodes are self-assembled monolayers [42]. SAMs are ordered molecular assemblies that are formed spontaneously on a surface. The popularity of layers can be explained by the simplicity of their formation. In literature, the first report of SAMs was in 1980, when Sagiv published a paper about molecular monolayer chemically attached to silicon dioxide [81]. In 1983, Nuzzo and co-workers published the preparation of thiolated SAMs on gold by the interaction between sulphur and gold [82]. The methods established by these two scientists resulted in spontaneously formed, highly ordered molecular monolayers on surfaces. A substrate is dipped in a solution containing the self-assembling molecules. With time, a monolayer is assembled on the surface in an ordered manner (Fig. 9) [42].

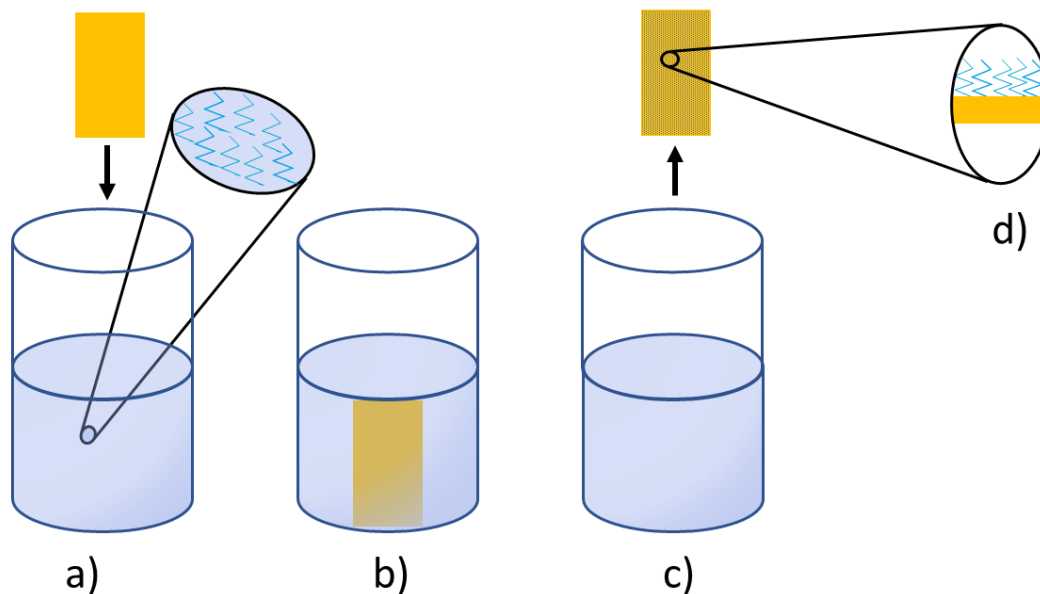
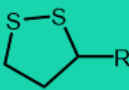


Fig. 9: Preparation of SAMs: a) a substrate is immersed in a solution containing the self-assembling molecules, b) the substrate remains immersed in solution for more than 15 h in order that molecules achieve a dense packing on the surface, c) after taking out the substrate from the solution, the SAM adsorbed on substrate is ready for further modification or characterization d) a schematic representation of an assembled densely packed SAM.

Molecules need to be constructed on special way to form SAMs (Fig. 10). They need to have a headgroup, a spacer and a tailgroup [42]:

1. The function of **headgroup** is to bind molecules to the surface of substrate. The molecules are immobilized on the surfaces via the chemical bond formed between the headgroup and the substrate. Until today a wide variety of the headgroups is known that can bind to metals, metal oxides, and semiconductors [42]. For example, molecules which have thiols, disulfides, cyclic disulfides and sulfides can be bound to gold [42] and silanes on silicon dioxide or ITO [83].
2. The **spacer** or **backbone** has function to connects headgroup and tailgroup. This part also stabilizes the SAM because of van der Waals interactions between different molecules that cause a dense packing of the molecules. The spacer can influence the electronic conductivity of the layers.
3. The **tailgroup** is the group that gives special functionality to the surface. In the simplest case it is a methyl- group. However, a lot of SAMs with other functionalized groups have been prepared so far [84–86]. The fact that the tailgroup of SAMs can be modified chemically or electrochemically makes them an extraordinary powerful system [85].

Surface	Head group	Spacer	Tail group
Au	HS-R		Function
	R-S-S-R'		
			
ITO	H ₃ Si-R		
SiO ₂			

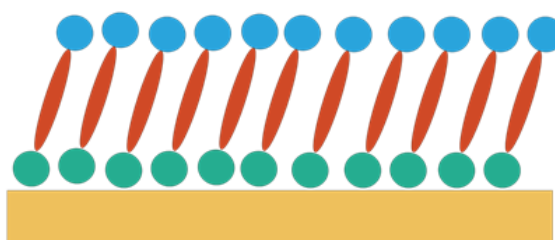


Fig. 10: Structure of the molecule that can be self-assembled on surfaces where colours in the table correspond to colours in the scheme below table: yellow represents the most common surface for self-assembly of molecules, green are headgroups that can create a chemical bond with the surface. With red are marked the most common groups that spacer is built of, blue coloured is a head group that can be designed to provide any specific functionality of the surface.

Since its discovery, SAMs found application in molecular sensing and production of nanodevices, like sensors [45–50], biosensors [38, 39, 51], molecular motors [87], as coating against corrosion [88, 89], in electronic devices [79, 90], and as inks in dip-pen lithography [91, 92].

The integration of multiple functionality in SAMs can lead to integrated molecular system [40]. These are complicated molecular systems on the surfaces, which are often built in several different steps [36] that include chemical and electrochemical modification [36, 40]. It is essential to characterize intermediate steps with various surface characterization methods. As stated in a review by Gooding and co-authors “characterise, characterise and characterise to really prove the molecular construct has been prepared as intended (that is, as the cartoons suggest). Good luck” [36]. This characterization is a substantial challenge compared to the structural characterization of dissolved organic molecules because different compounds potentially present on the surface cannot be separated. Some powerful techniques, especially nucleus magnetic

resonance and mass spectroscopy with soft ionization cannot be applied and finally the total amount of substance is extremely small (i. e. about 10^{-9} mol cm^{-2}).

3. 2 Electrochemistry of SAMs

Voltammetry and various spectroscopic techniques are suitable for characterization of SAMs. Also, SAMs are powerful system for studying electron transfer properties. In this work, voltammetry was used to characterize and to modify SAMs and spectroscopic techniques as XPS (Chapter 3.3) and PM IRRAS (Chapter 3.4) were used for further analysis.

3. 2. 1 Voltammetry of SAMs

A significant amount of information can be obtained from a cyclic voltammogram of the surface-bound redox-active species. A typical cyclic voltammogram, of redox-active immobilised species is shown in Fig. 11. The electrochemical response of the surface-immobilised redox-active species is different from that of the same molecule diffusing in solution (described in Chapter 2.2.1). Firstly, immobilised redox systems show a linear dependence of the peak current I_p on the scan rate ν as can be determined from equation (15). The charge under the anodic and the cathodic peak is proportional to the number of the redox-active species contributing to the electron transfer reaction on surface. The interfacial concentration Γ of the redox-active species can be calculated from charge Q underneath the anodic or the cathodic peak using equation (16).

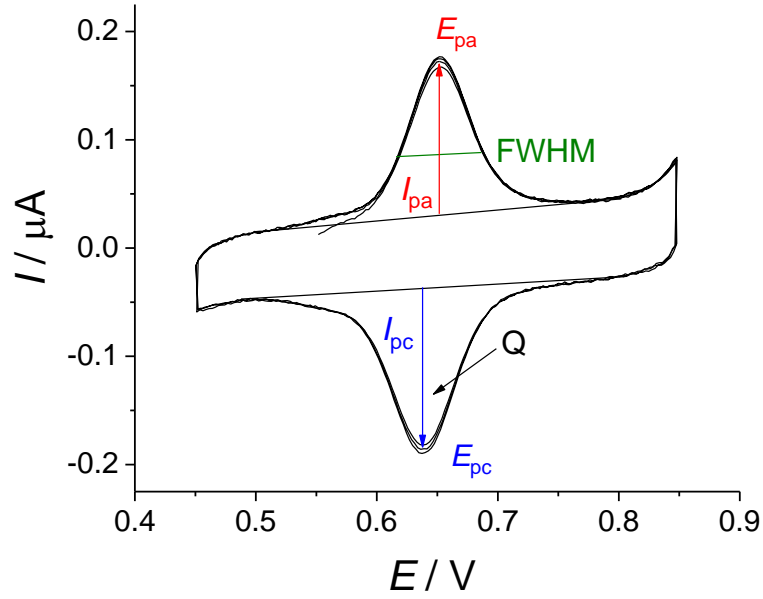


Fig. 11: Cyclic voltammogram of the surface immobilised diethyl 2-((3-(5-(1,2-dithiolan-3-yl)pentanamido)propyl)amino)-5-((tert-butoxycarbonyl)amino)terephthalate in 0.1 M HClO₄, scan rate 0.01 Vs⁻¹ (E_{pc} and E_{pa} are the cathodic and the anodic peak potentials, I_{pc} and I_{pa} are the cathodic and the anodic peak current, FWHM is full width at half maximum of the peak and Q is charge underneath the peak)

$$I_p = \frac{F^2 n^2}{4RT} v A \Gamma \quad (15)$$

$$\Gamma = \frac{Q}{nFA} = \frac{1}{nFA} \int_{E_2}^{E_1} I(E) dE \quad (16)$$

From the full width at half maximum (FWHM) of the peak, the homogeneity of monolayer can be evaluated by equation (17). Values of FWHM that are larger or smaller than theoretical value of surface bound reversible system can be attributed to electrostatic effects caused by neighbouring molecules in layer [93]. Separation between the potential of the anodic peak E_{pa} and the cathodic peak E_{pc} at slow scan rates is 0 because diffusion does not play a role (redox-active centres are adsorbed on surface of the electrode). With the increase of the scan rate, peak separation can be observed due to limitation of the electron transfer rate [64, 94].

$$FWHM = 3.53 \frac{RT}{nF} = \frac{90.6}{n} \quad (17)$$

In 1979, Laviron published an experimental method to determine k_{ET} of the species adsorbed to an electrode using potential sweep methods [94]. Equation (18) includes the transfer coefficient α , which is ideally $\alpha = 0.5$, however, in many cases deviates from this value. It can be determined as slope when the peak potential E_{pa} and E_{pc} are plotted versus the logarithm of scan rate $\log \nu$ [94]. An example is shown in Fig. 53. Then k_{ET} can be determined from the following equation:

$$k_{ET} = \frac{\alpha n F v_c}{RT} = \frac{(1 - \alpha) n F v_a}{RT} \quad (18)$$

Where v_a and v_c are the intercepts of regression lines for the anodic and the cathodic branches from $E_p = f(\log \nu)$.

3. 2. 2 Electrochemical modification of the surfaces

Except for characterization of SAMs described in previous Chapters, voltammetry can be used to trigger reactions on the surfaces. This “dynamic” type of monolayers has been developed recently where activities of molecular monolayers can be “turned on” from an inactive state to an active state just by applying potential. Example for electrochemically triggered reactions on the surfaces is deprotection of SAMs. This method is quantitative, rapid, and mild. Also, SAMs can have protective groups that are photodeprotectable [95] and acid/base-labile [96]. The limitations of those methods are that the quantification of the deprotection processes is not easy and the treatments for removal of the protecting groups can have severe physical and chemical steps that may cause a degradation of molecules on the surface.

Kim and co-authors have electrochemically deprotected SAMs in what they called “electrochemical activation” for site-selective immobilization of biomolecules [97]. They have developed a system with monocarboxylic ester of hydroquinone as the electrochemically removable protecting group of SAMs on gold surfaces. Firstly, hydroquinone is electrochemically oxidized to quinone and this process is followed by chemical nucleophilic acyl substitution of quinone by H_2O (Fig. 12). Electrochemically activated surfaces that are carboxylic acid terminated have be used as specific binding sites for amine-containing molecules. In cyclic voltammograms electrochemical

activation can be seen as an irreversible anodic peak at 0.2 V vs. Hg/Hg₂SO₄ in the first scan which disappears in the second cycle. This indicates fast and almost complete release of quinones from the surfaces. Electrochemical quartz crystal microbalance data recorded simultaneously with cyclic voltammogram supported the claim of deprotection of SAMs. Grazing angle Fourier transform infrared spectra also proved the electrochemical activation of SAMs. In the spectra the positions and intensities of the C-H vibrations revealed no significant change, the C=C stretch of 1509 cm⁻¹ from hydroquinone was diminished.

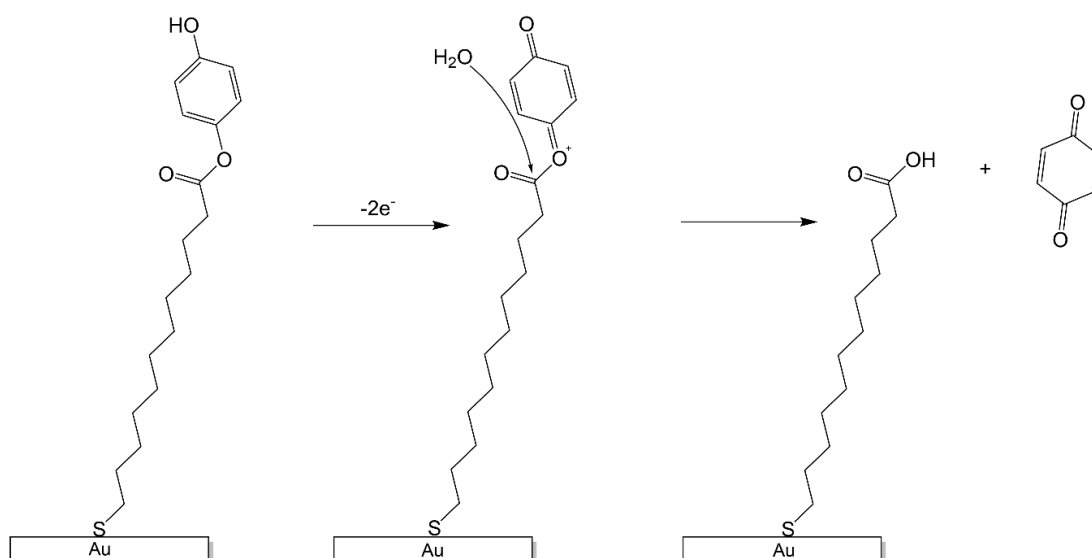


Fig. 12: Schematic representation of electrochemical activation of a SAM containing monocarboxylic esters of hydroquinone where ω -carboxylic acids is generated. In the first step hydroquinone is electrochemically oxidized to quinone and this process is followed by chemical nucleophilic acyl substitution of quinone by H₂O.

The same authors also used electrochemical activation for bioinactive surfaces with hydroquinone-caged biotin [98]. In this work the same mechanism of activation was used as in previous study, the hydroquinone was firstly oxidized (converted to a benzoquinonium cation). After the nucleophilic acyl substitution by H₂O occurred, benzoquinone and CO₂ are released, and the bioactive biotin surface is generated (Fig. 13). Again, electrochemical activation was seen as an irreversible anodic peak at 0.20 V vs. Hg/Hg₂SO₄ in the first scan of a cyclic voltammogram which disappears in the second scan. The grazing angle Fourier transform infrared spectra of SAM surfaces showed no changes in intensity, as well as in the position of the C-H stretching region. The aromatic C=C stretching at 1511 cm⁻¹ decreased in intensity, and the peak intensity at 1796 cm⁻¹

(C=O stretching in urethane) was reduced to half of the initial intensity, which proves a mild electrochemical activation reaction.

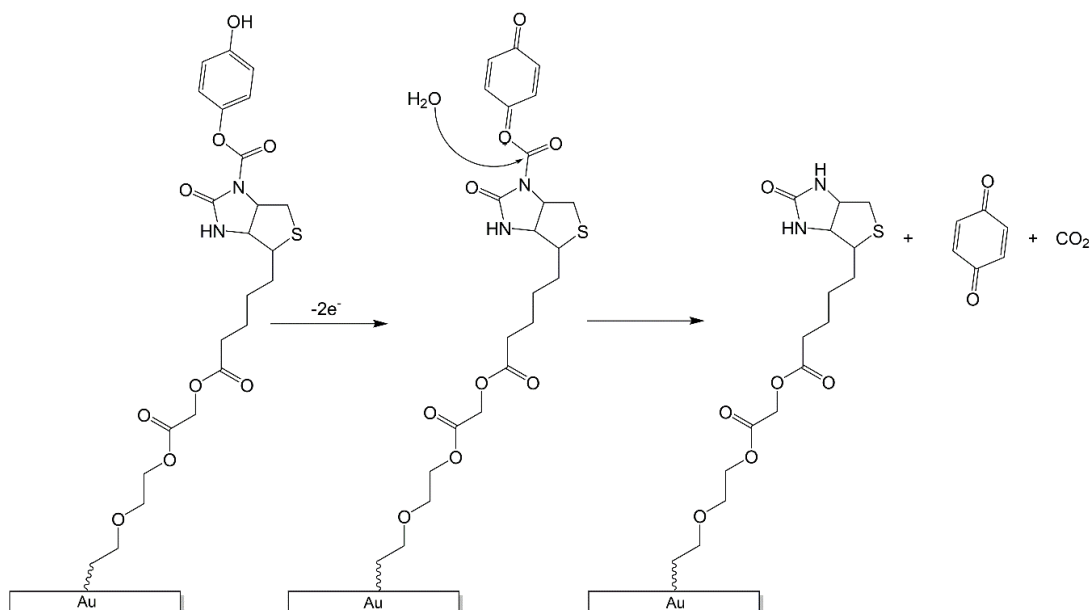


Fig. 13: Schematic representation of the electrochemical activation of hydroquinone-caged biotin-modified gold surface where bioactive biotin is generated. Firstly, the hydroquinone was oxidized, after the nucleophilic acyl substitution by H_2O occurred where benzoquinone and CO_2 are released from the surface.

Electrochemistry can be also used for addition of various molecules on surfaces modified with redox-active SAMs. Yousaf and Mrksich [99] used a quinone tailgroup-terminated SAMs as platform for the Diels-Alder (D-A) reaction for the immobilisation of cyclopentadiene onto SAMs (Fig. 14). The design of surfaces allows the electrochemical control of the reactivity of the surfaces. The oxidized state of the molecule on the surfaces (quinone) is reactive and when the molecule is reduced on the surface to the hydroquinone, the SAM becomes inactive and D-A reaction cannot be performed. After the D-A addition of cyclopentadiene to the SAM, a decrease of the peak currents in cyclic voltammograms for the reduction and oxidation of the hydroquinone/quinone couple is indicative of the reaction progress. The reaction can be described with the EC mechanism on surfaces.

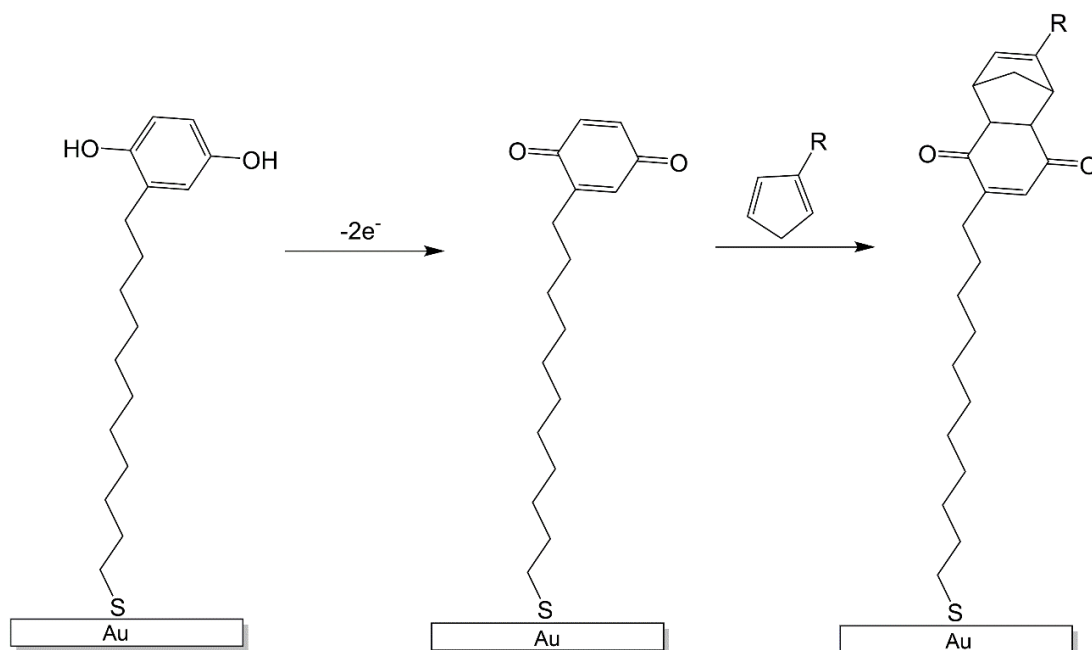


Fig. 14: Schematic representation a quinone tailgroup terminated SAMs as platform for the Diels-Alder (D-A) reaction. In the first step electrochemical oxidation of hydroquinone to quinone occurs. After electrochemical oxidation quinone react with cyclopentadiene to give the D-A adduct.

Kwon and Mrksich [100] further investigated the influence of the steric environment around the reacting molecules on the D-A surface reaction. Their results showed that the activation parameters of the quinone groups that were positioned in a crowded environment and below the SAM | solution interface reacted with an enthalpy of activation that was 4 kcal/mol higher than that of quinones accessible at the interface.

Furthermore Gawalt and Mrksich [101] measured rate constants for the D-A reaction of a series of dienes with a monolayer presenting benzoquinone groups at 10% density among hydroxyl-terminated alkanethiolates. A series of dienes were used that comprised molecules of different steric and electronic character: cyclopentadiene (Cp), methylcyclopentadiene (MeCp), 1,2,3,4,5-pentamethylcyclopentadiene (Me₅Cp), *tert*-butylcyclopentadiene, 5,5-dimethoxy-1,2,3,4-tetrachlorocyclopentadiene and 1,2,3,4,5,5-hexachlorocyclopentadiene were studied. Three of the dienes (Cp, MeCp, and Me₅Cp) reacted efficiently with the immobilized mercaptobenzoquinone. They found that the dienes with electron-withdrawing groups or with the sterically demanding *tert*-butyl group did not undergo reaction with the quinone over the time course of a typical experiment. The molecules that reacted efficiently, Cp, MeCp, and Me₅Cp, have a similar kinetic behaviour.

Shamsipur and co-authors [102] studied electrochemical Michael-addition reaction on surfaces of hydroquinone terminated SAMs with glutathione. When a suitable potential was applied to the SAM, the hydroquinone moiety of SAM generates o-benzoquinone. This active intermediate undergoes a Michael-addition reaction with glutathione. This mechanism is a representation of the reversible oxidation of hydroquinone moiety to quinone followed by an interfacial chemical nucleophilic addition which can be described with the EC mechanism. In voltammograms the peak of oxidation and reduction of benzoquinone is diminishing with time, which is not the case when glutathione is not present in solution. In the interfacial IR spectra, a new absorption band appeared at 1725 cm^{-1} which is attributed to the C=O stretching of the immobilized glutathione on surface, which is evidence of the interfacial reaction on the surface.

3.3 X-ray photoelectron spectroscopy

X-ray photoelectron spectroscopy (XPS) or electron spectroscopy for chemical analysis (ESCA) is a popular method for characterization of the surfaces [103]. The technique is enabled by key scientific achievement, five of them were honored by Nobel prizes. The first one was given to Wilhelm Conrad Röntgen for discovery of X-rays [104]. Max von Laue was the second recipient for “his discovery of the diffraction of X-rays by crystals” [105]. The third one was awarded to Kai Siegbahn, the inventor of XPS, “for his contribution to the development of high-resolution electron spectroscopy“ [106]. His son Karl Manne Georg Siegbahn was honoured by the fourth one for “developed apparatus and methods for improving accuracy when mapping x-ray spectra” [107]. The fifth one was actually given to Albert Einstein “for his services to theoretical physics, and especially for his discovery of the law of the photoelectric effect” which is the main principle of XPS [108].

3.3.1 Basic principle

Today, XPS allows chemical identification and quantification of atoms on surfaces. The basic principle of XPS can be described as interaction of the photon with electrons of a specific atomic orbital. In this process, the photon transfers all its energy to the core level electron. If the photon energy is high enough, the electron is emitted. The kinetic energy E_{kin} is analyzed, it is the difference between the photon energy $h\nu$ and the

binding energy E_B of the electron. Although, the kinetic energy E_{kin} of the electron is the experimentally measured by the spectrometer, this energy is dependent on the photon energy of the X-rays. The source of the primary radiation of X-rays are most commonly Al K_α or Mg K_α anode. Al K_α provides photons of 1486.6 eV and Mg K_α of 1253.6 eV. Because of this in spectra the binding energy of the electron E_B is the parameter which identifies the electron specifically, and it can be calculated as:

$$E_B = hv - E_{kin} - \varphi \quad (19)$$

φ is the work function and is specific to the spectrometer. Work function is described as the minimum energy necessary to remove an electron with the assumption that a conductive sample which is in physical contact with the instrument is analysed.

The process of photoemission is shown schematically in Fig. 15 (1), where an 1s electron is ejected from the atom. The spectrum will reproduce the electronic structure of an investigated system because all electrons with a binding energy lower than the photon energy will be detected in the spectrum. The electrons which are excited and escape without energy loss contribute to the characteristic peaks in the spectrum. The electrons which suffer energy loss because of inelastic scattering contribute to the background of the spectrum. Once an electron has been emitted, the ionized atom that was created in this process must relax. This can be achieved by the emission of an X-ray photon, known as X-ray fluorescence shown in Fig. 15 (2). The other possibility is the ejection of an Auger electron, the process is shown in Fig. 15 (3). Thus, Auger electrons are produced as a consequence of the photoemission, these electrons can yield valuable chemical information about the investigated atom. The technique that uses Auger electrons for analysis is called X-AES (X-ray induced Auger electron spectroscopy). X-AES will not be further discussed in this thesis.

With XPS is possible to identify the elemental composition of any solid (all elements from Li to U can be detected if their atomic % is above 0.05 and within a depth of 10 nm from the surface), as well as the chemical environment of elements in investigated sample.

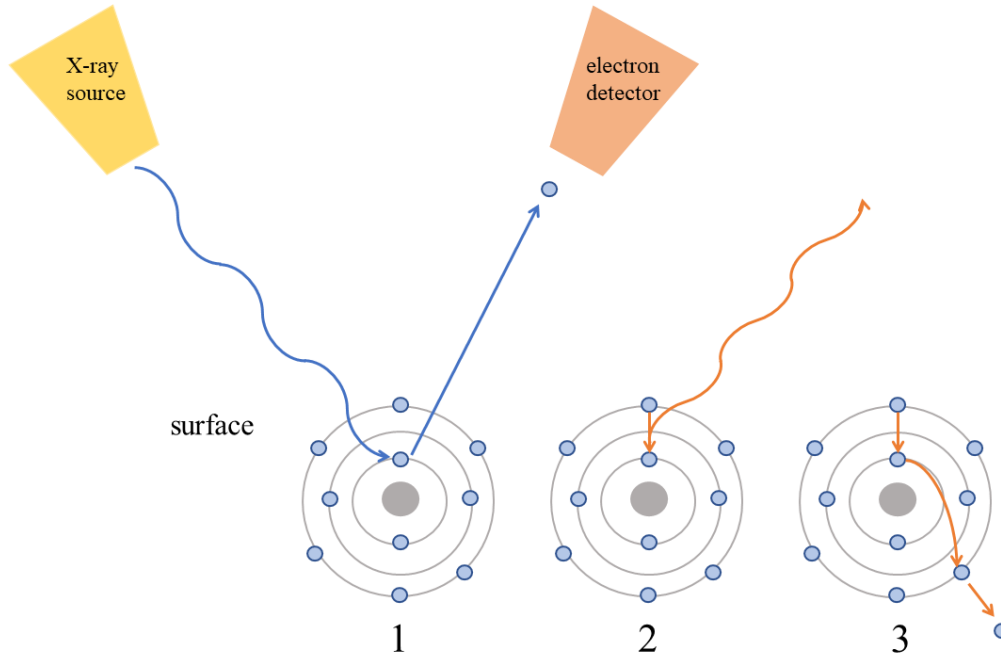


Fig. 15: Processes happening in XPS: 1) photoelectron emission 2) X-ray emission 3) photoemission followed by emission of an Auger electron.

3.3.2 Binding energy

Binding energy is described as the difference of the final state E_{N-1} with $N-1$ electrons and the initial state E_N with N electrons:

$$E_B = E_{N-1} - E_N \quad (20)$$

According to the Koopmans' theorem [109], the binding energy would be equal to the negative orbital energy, $-\varepsilon_k$, for the ejected photoelectron if there would be no rearrangement of the electrons in the atom or material during the photoemission process in the final state. This claim is written as:

$$E_B = -\varepsilon_k \quad (21)$$

The values of ε_k in equation (21) can be calculated with the Hartree–Fock method. Values of ε_k deviate 10–30 eV from the actual E_B values. The deviation between E_B and $-\varepsilon_k$ comes from the fact that in Koopmans' theorem and the Hartree–Fock calculation method it is assumed that the other electrons “freeze” during the photoemission process, which is not the case. During emission of the photoelectron, the other electrons in the sample will

respond to the creation of the core hole by rearranging to minimize the energy of the ionized atom. The reduction in energy caused by this rearrangement of electrons is called the ‘relaxation energy’. Except relaxation, electron correlation and relativistic effects are also neglected by the Koopmans theorem. Both terms are typically small and usually can be neglected.

The initial state is the ground state of the atom before the photoemission process. The energy of the initial state of the atom can exhibit variation that result from the chemical environment of the atom (by forming chemical bonds with other atoms). The binding energy of electrons in the analysed atom will change for ΔE_B and is commonly called the chemical shift. It is defined with equation (22):

$$\Delta E_B = E_{B(\text{compound})} - E_{B(\text{element})} \quad (22)$$

Almost all elements in the periodic table exhibit a chemical shift. Therefore, XPS allows not only to identify elements but also its binding states.

This chemical shift can be a fraction of an eV to few eV depending of chemical species. If one takes carbon as an example, the C-O bond in an organic molecule is shifted 1.6 eV [103] relatively to the carbon in graphite, while both C=O and O-C-O are shifted for 3.1 eV [103]. In principle, if there are bonds with electronegative atoms, the chemical shift in XPS is to higher binding energies. Said in simple words, the lower the electron density of the emitted atom the higher is E_B .

The final state is significantly impacted by relaxation effects, therefore also the measured E_B . During photoemission the electron rearrangements lowers E_B . The atom from which the electron is emitted (atomic relaxation) and its surrounding atoms (extra-atomic relaxation) contribute to the relaxation energy. Most of the atomic relaxation comes from rearrangement of outer shell electrons. The inner shell electrons have a small contribution to the atomic relaxation energy and can be in most of the cases neglected. The extra-atomic relaxation depends on the nature of examined material. In the case of electrically conducting samples (metals), valence band electrons can move from one atom to the other to screen the core hole. For ionically bonded solids (for example alkali

halides), electrons cannot move freely from one atom to another. In these materials the electrons can be polarized by the presence of a core hole. The reduction of binding energy caused by extra-atomic relaxation in ionic materials is smaller than in metallic samples. Other types of final state effects such as shake-up satellites can contribute to E_B . Shake-up satellites originate from the photoelectron which lose part of its kinetic energy to excite a valence electron into an unoccupied orbital (e.g. $\pi \rightarrow \pi^*$ transition).

3. 3. 3 Photo electron intensities

The intensities of photoelectrons depend on several parameters and they can be divided into three main groups. The first group of parameters depends on the physics of photoelectron production. The second group of parameters depends on the interaction of the photoelectrons with the surrounding solid and the third group of parameters is dependent on the instrument geometry and will not be discussed further in this thesis.

Photoelectron Cross Sections. The first parameter of a specific energy that is dependent on the physics of the photoemission process is the photoelectron cross section. The cross section describes the probability that a photon will cause a photoemission from a specific core level of a specific element. Scofield calculated the values for the photoelectron cross sections for all elements from Li to U when irradiated with Al K_α and Mg K_α [110]. They do not vary with the chemical environment of the emitter atom. This parameter is especially important for systems such as molecular monolayers assembled on surfaces. In these systems, the number of emitter atoms is small and sensitivity can be an issue. Therefore, atoms with larger cross sections like fluorine and chlorine are often included in the tailgroup of the molecule for easier XPS detection. Also, when specific reactions are followed on surfaces with XPS like addition of molecules and cleavage of specific groups this feature is especially employed as seen in Chapter 7.

Attenuation length in SAMs. The parameters that describe the interaction of photoelectrons with the surrounding environment are those that result in a loss of the intensity of photoelectrons. While X-rays penetrate in the sample within few μm , only electrons that do not suffer energy loss contribute to peaks in the spectrum. Those electrons originate from a surface layer of a few nm thickness. This effect must be considered for precise application of electron spectroscopies in quantitative analysis of

molecular monolayers. For an accurate quantification, the attenuation length (λ) of electrons as a function of their kinetic energy E_{kin} and the density of the matrix must be known. Experimentally, it is often the escape depth of electrons which is measured. The escape depth is defined as the distance normal to the surface at which the probability of an electron escaping without significant energy loss due to inelastic scattering processes drops to e^{-1} of its original value (Fig. 16). This attenuation can be described with the following equation:

$$I(A) = I_0(A)e^{-d/\lambda \sin \theta} \quad (23)$$

Where $I(A)$ is the intensity of a photoelectron peak from an element A in a substrate covered with a film of thickness d , $I_0(A)$ is the intensity of the same peak from a clean substrate, and θ is the angle between the plane of the substrate and the detector. If $\theta = 90^\circ$, the escape depth is equivalent to the attenuation length.

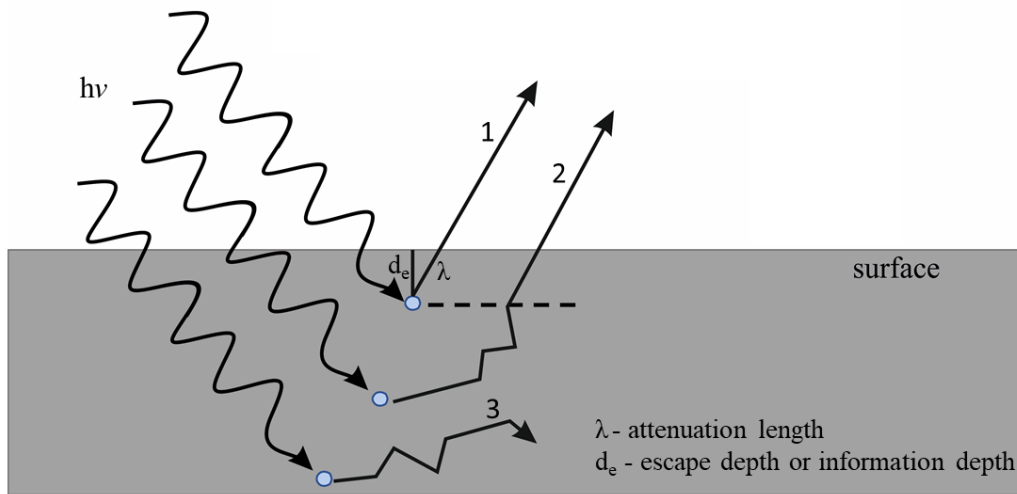


Fig. 16: Schematic representation of the depth dependence of signal attenuation: 1) photoelectrons are emitted without kinetic energy loss, where $d_e = \lambda \cos \alpha$ (α is angle between d_e and λ), 2) photoelectrons are emitted from a larger depth, they reach the detector with a loss of kinetic energy and contribute to the background, 3) photoelectrons that are emitted from larger depths lose all their kinetic energy before reaching the surface.

Attenuation length of photoelectrons in SAMs can also be used to evaluate the layer thickness [111–113]. For the application of this method, one has to assume that the value of λ in SAMs is equal to that of the bulk material. This is not always correct since λ is dependent of the substrate roughness, the crystallinity and the orientational order of

the molecular monolayers. This can be executed using equation (23) if one takes the intensity from the gold photoelectrons attenuated by the monolayer as $I(A)$, the intensity from clean gold substrate as $I_0(A)$ and the film thickness, d , can be approximated by nl , where n is the number of carbon atoms in the chain, and l is the height equivalent to one C–C bond perpendicular to the surface.

Laibinis et al. [114] have measured the attenuation of the photoelectrons from a gold substrate as a function of the thickness of an alkanethiol film in the kinetic energy range 500-1500 eV. Lamont et al. used the same method to estimate λ in the 140-1100 eV energy range [115]. Their results [115] give values lower by 25% compared to those determined by Laibinis et al. [114] at comparable energies. This difference could be attributed to differences in preparation of SAMs or to the difference in the used substrates. The values of λ are only valid for a specific thiol for which they were determined (alkane chains in case of this two studies) and may vary with packing of molecules on the surface, which is influenced by preparation method [116]. Layers containing specific groups will show different organization and packing on the surfaces as a function of chain length [113]. To estimate λ by this method, the attenuation of the gold signal has to be measured for several layers with different chain lengths. This is not always possible, particularly when the investigated layers contain more complicated chemical species (like the ones used in Chapter 7) for which several chain lengths are not necessarily available.

3.3.4 Splitting of the energy levels

One more important characteristic of XP spectra is splitting of the energy levels that is caused by spin-orbit coupling. Core levels in XPS are given by the notation as nl_j , where n is the principal quantum number, l is the angular momentum quantum number and $j = l+s$, where s is the spin angular momentum number with values $\pm 1/2$. Only s levels have no splitting because l is 0. For the 2p spectra, n is 2 and l is 1, so j can be 1/2 and 3/2. The peaks have areas proportional to $2j+1$. For $p_{3/2}$ ($j = 1.5$) and $p_{1/2}$ orbitals ($j = 0.5$), and the ratio between the peak area is 4:2 or 2:1. These ratios must be considered when the p, d and f core levels are analyzed. The splitting is detected in the high resolution XP spectra. Splitting of the S 2p photoemission line is shown in Fig. 17. The value of splitting is rather constant, for S 2p it is ≈ 1.15 eV.

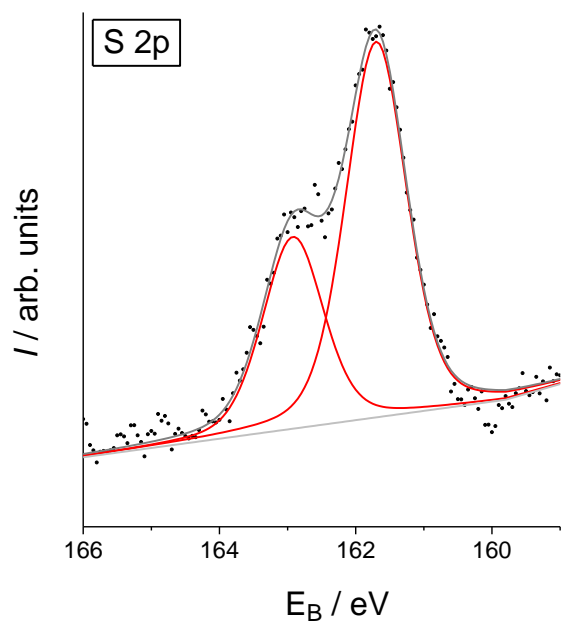


Fig. 17: S 2p XPS spectra of self-assembled monolayer of diethyl 2-(5-(1,2-dithiolan-3-yl) pentanamido) 5-((tert-butoxycarbonyl)amino)terephthalate on gold substrate.

The survey spectra of the fluorinated self-assembled monolayer on gold is shown in Fig. 18. Most commonly, the intensity is plotted against the binding energy, which is recalculated from the measured kinetic energy. The strongest signals in the spectra are the signals of the gold substrate underneath the molecular monolayer. Carbon, sulphur, oxygen and fluorine can be also seen in Fig. 18 as low intensity signals. For the analysis of this small signals, high-resolution spectra such as that in Fig. 17 must be recorded.

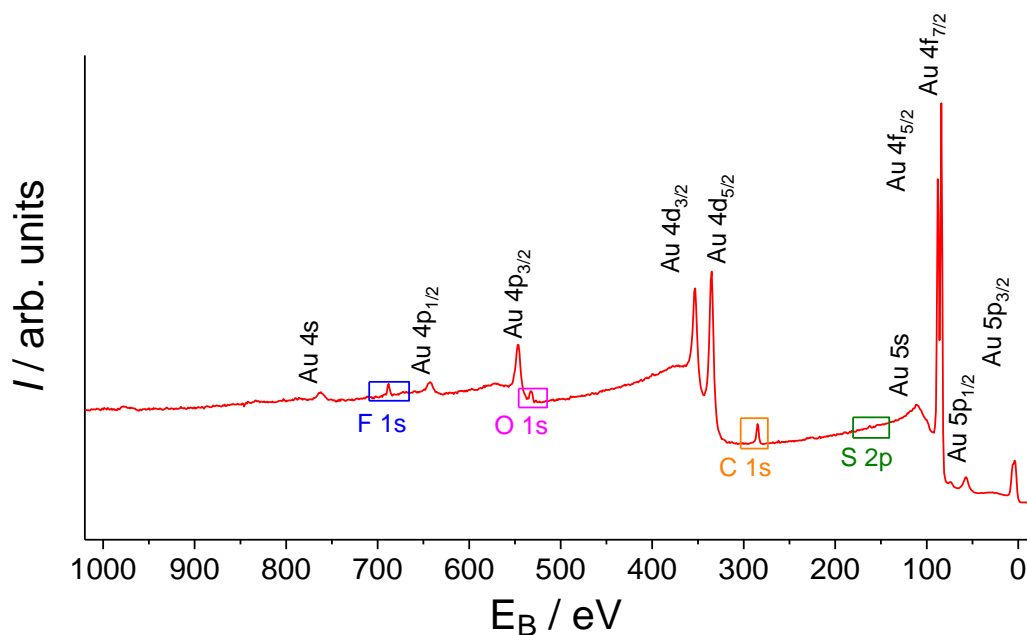


Fig. 18: Survey spectra of SAM of diethyl 2-(5-(1,2-dithiolan-3-yl)pentanamido)-5-((4-(trifluoromethyl)benzyl)amino)terephthalate on gold substrate.

3.3.5 Radiation damage

One of the common misconceptions associated with XPS is that it is a non-destructive technique. In many cases, samples are damaged during analyses. X-ray irradiation can induce desorption of the species bound to the surfaces, reduction or oxidation of atoms or ions of the sample by low energy electrons, phase changes in analysed area, migration of the specific elements in samples induced by an electric field.

Molecular monolayers are the example of systems where radiation-induced damage occurs when analysed by XPS. It includes chemical and structural change that are caused by the X-ray photons and the emitted photoelectrons. The appearance of radiation-induced damage is well documented in literature [117–126].

Until today it has been shown that damage done by X-ray irradiation of alkanethiol monolayers can induce new spectral components, line broadening and change in intensity. These spectral modifications have been attributed to a lower level orientation and conformation, modification of sulphur on the surface and desorption of parts of chains in molecular monolayers. The change in the sulphur spectra is assigned to a change in

bonding between sulphur and gold by photoelectrons that were slowed down by inelastic scattering.

The new sulphur species generated from radiation-induced damage of alkanethiols have been assigned as disulphide species in some studies [117, 121, 127]. A photoelectron S 2p spectrum that contains species produced by radiation damage of X-ray beam of self-assembled monolayer is presented in Fig. 19. A shoulder is observed at 164.5 eV, which is characteristic of the S 2p_{1/2} signal from a radiation induced species [127]. The associated S 2p_{3/2} orbital (163.3 eV) is hidden by the S 2p_{1/2} peak of the sulphur bound to the gold. To evidence these two species, the S 2p spectrum needs to be fitted using two doublets with 2:1 peak area ratio and 1.15 eV spin-orbit splitting. The amount of radiation induced species increases when the X-ray power is increased. This occurrence of radiation-induced species is always observed in XP spectra after a longer accumulation time.

In their study, Zubragel et al. [128] found two chemically different sulphur species in a *n* docosanethiol monolayer. The difference in binding energy in S 2p spectra was interpreted as the presence of dialkyldisulphide species where one S atom interacts with the Au substrate and the other one is located slightly higher. In this study, it was proposed that either both S atoms were at different heights with respect to the surface or that the conformation of the chains was different for the two species.

Lamont et al. [115] attempted to assign the species produced by radiation damage by analysis of Au 4f, C 1s, and S 2p spectra from a tetradecanethiol monolayer after 1 min exposure to zero-order synchrotron radiation. They found an increase in the S 2p and Au 4f peak intensities and a decrease in the C 1s peak after irradiation. This was interpreted as a fission of the chains in the region of C–S bond. Even though they saw a new S 2p species at 163 eV, they excluded that this species could be disulphide species. This was based on the fact that production on disulphide would only cause a shift in the S 2p spectra, without any changes in the of C 1s and Au 4f spectra. In this paper the new sulphur species was assigned to atomic sulphur on gold, resulting from desorption of the parts of the chains. They concluded that 2–3% of the monolayer decompose in 10 min.

Heister et al. have shown in their research that the sulphide species are distributed over the alkyl chains [129]. In their study distribution of sulphide species is not in agreement with a fission of C–S bonds which results in atomic sulphur that was proposed by Lamont et al. [115]. The observations in these two papers agree very well, but the interpretation differ. The observations of Lamont et al. [115] can be explained by the model of sulphur incorporation into the alkyl chains.

Zharnikov et al. [124, 125, 129] proposed an alternative interpretation for the new sulphur species at higher binding energies. They explain it as incorporation of sulphur into the alkyl chains via bonding to irradiation-induced carbon radicals in the chains [124, 125, 129]. They have assigned the increase of the Au 4f intensity and broadening of the C 1s peak to desorption of film fragments. The FWHM of the fitted peaks for the irradiation-damaged film was about 30% larger than that of the C 1s peak from the intact film. Also, the FWHM of the S 2p peak continuously increased with the X-ray irradiation. They also observed an increase of the FWHM of the Au 4f peaks and interpreted it as a dissociation of S–Au bonds.

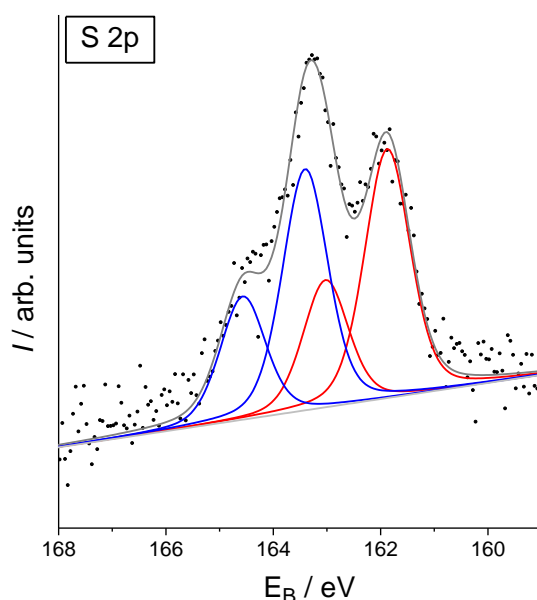


Fig. 19: S 2p spectra of 1-hexanethiol monolayer on gold substrate. There are two S 2p_{3/2} signals with binding energies at 161.9 eV (red) and 163.5 eV (blue). The second signal, coloured blue represents XPS-induced radiation damage of sulphur in SAMs.

Even though the effects of the induced damage by XPS analysis have been extensively characterized, as it can be seen from the previous text, the assignment of species produced during XPS analysis of SAMs is still controversial.

In order to minimise or avoid radiation damage in SAMs the method proposed in Ref. [130] can be used. In this method separate spots were measured for every scan to prevent the samples from becoming damaged by X-rays, each at minimum acquisition time. All spectra were finally added to one single spectrum. This method provides spectra as in Fig. 17 on the expense of a lower than optimal signal-to-noise ratio. In this work, this method was not applied because of the small electrochemically modified surface area due to construction of the electrochemical cell (Fig. 23).

3.3.6 Quantification of XP spectra

XPS is widely applied for the characterization and quantification of molecular monolayers. For quantification in software that is used for the XP spectra analysis the peak areas are divided by standard sensitivity factors and normalized to obtain “raw” concentrations. These raw concentrations give only a rough indication of the relative amounts of elements that are present in the sample. For a more exact consideration, the heterogenous composition in analysed samples must be considered. The composition varies as a function of depth. This is even problematic with homogeneous materials because the concentrations determined from XPS results can be different from the actual concentrations because the XPS signal also depends on the inelastic mean free path (IMFP) of the photoelectrons. The IMFP is dependent of the E_{kin} and on the composition of the analysed material. The consequence is that the standard sensitivity factors from software packages are valid only for the material for which these factors have been determined. Even though XPS is not the most precise method for quantification, in this thesis, the quantity of different elements in SAMs are estimated from this data and the precision of this method is sufficient for the necessity of this thesis.

3.4 PM IRRAS of SAMs

Polarization-modulated infrared reflection absorption spectroscopy (PM IRRAS) is a method for characterization of the molecules adsorbed on IR reflective surfaces [131]. The measured spectra provide information about the composition, structure and orientation of the adsorbed molecules.

3. 4. 1 Principle

Infrared reflection absorption spectroscopy (IRRAS) has been developed in the 1960s [132, 133] as one of the most surface-sensitive methods. The method allows investigation of surface structures [134], chemical states of adsorbates [134] and the orientation of the adsorbates on the surface [135]. However, the sensitivity of these measurements is often limited because the signals of interest from surface adsorbates are often camouflaged with atmospheric background absorption. Therefore, IRRAS is mostly applied under ultra-high vacuum (UHV). The IRRAS technique was significantly improved by the use of a photoelastic modulator, PEM [136]. A photoelastic modulator is a CaF or ZnSe crystal which is periodically compressed and expanded so that s- or p-polarized light beam passes through the crystal. The main advantage of IRRAS with PEM - polarization modulation infrared reflection absorption spectroscopy (PM IRRAS) is the compensation of the background signal, which allows measurements under ambient conditions and even in liquids.

PM IRRAS uses reflection of IR light from surfaces for investigation of the molecular monolayers [103, 134]. When electromagnetic radiation passes the border between two media, a portion of radiation is reflected and the other portion passes through the second medium (Fig. 20). Snell's law describes the relationship as:

$$n_2 \sin \gamma_2 = n_1 \sin \gamma_1 \quad (24)$$

Here γ_1 is the angle between the incident light and the surface normal as well as the angle of the reflected light to the surface normal, γ_2 is the angle of the transmitted light and the surface normal. n_1 and n_2 are the refractive indices of the two media. The ratio between reflected and transmitted IR radiation is represented by Fresnel's law [137].

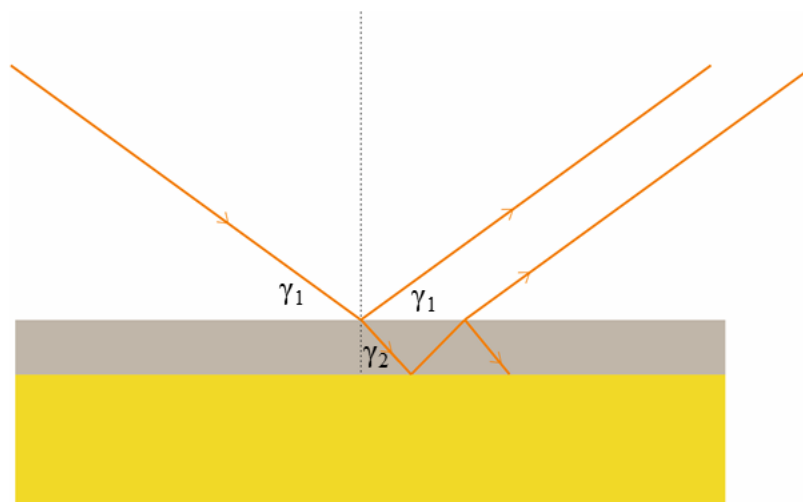


Fig. 20: Reflection and transmission of light on a layered system. The gray part is a molecular monolayer, the yellow one is the reflective gold surface and white is air.

Another important property of electromagnetic radiation which is the base of PM IRRAS the polarization. Polarized light can be separated into two orthogonal components of the electric field, p- and s-polarizations. In the case of p-polarization, the electric field vector is oscillating parallel to the plane of incidence. While, the electric field of s-polarized light oscillates perpendicular to the plane of incidence. When an electric field vector of light beam is reflected from a metallic surface a phase shift of 180° occurs between the incident and reflected electric field vector of light. Also, electric field vectors of the light beam are mirror imaged at the interface. After reflection of p-polarized light a constructive interference with the incident light beam occurs (Fig. 21a), which results in an increased intensity of the electric field perpendicular to the surface. Phase-shift for s-polarized light is about 180° at the time of reflection and a destructive interference cancels the electric field directly at the surface (Fig. 21b). Consequently, only vibrational transition can be observed, whose transition dipole moment has a component perpendicular to the surface. This phenomenon is called the surface selection rule. Therefore, only p-polarized light can interact with a sample at the surface. The phase shift of the p-polarized light depends on the grazing angle which is maximized near grazing angle ($>80^\circ$) due to the large z-component of the electric field. This angle for a gold surface is 85° .

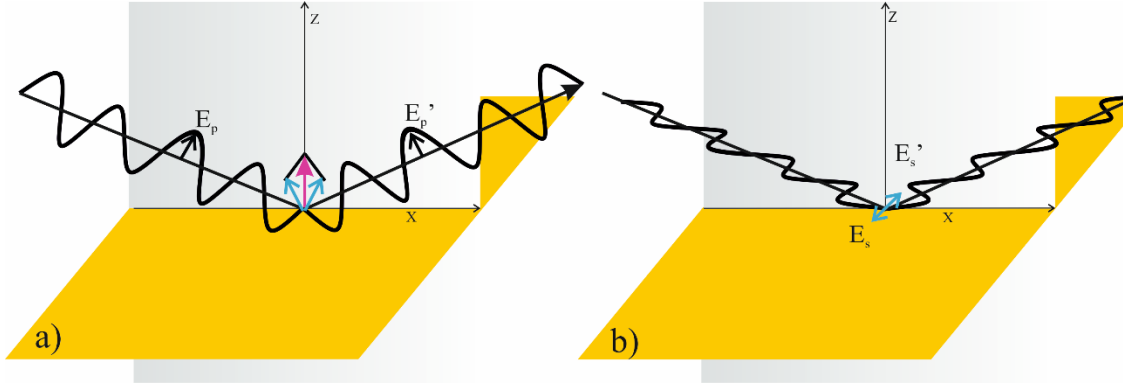


Fig. 21: Reflection of a) p- and b) s- polarized light at the interface.

In PM IRRAS both p- and s-polarized light beams are measured. PEM switches quickly between p- and s-polarized light beams, so the spectrum (with p-polarized light) and a reference spectrum (with s-polarized light) are measured simultaneously with a lock-in amplifier. The two components are used to compensate the background.

At the detector p- and light are not measured separately. The ratio of the difference of the reflected s- and p-polarized light and the average of both signals are measured [138]. This can be described as:

$$\frac{\Delta I}{\langle I \rangle} = \frac{I_s - I_p}{(I_s + I_p)/2} \quad (25)$$

Where $\Delta I = I_s - I_p$ is the signal difference and $\langle I \rangle = (I_s + I_p)/2$ is the averaged signal. The detected signal has to be demodulated to gain two intensities as a function of frequency ω_m of the PEM. They are linked to the Bessel functions of first $J_1(\Psi_0)$ and second $J_2(\Psi_0)$ order where Ψ_0 is the maximum shift of incident light produced by PEM.

$$I_D(2\omega_m) = \Delta I J_2(\Psi_0) \quad (26)$$

$$I_D(0) = \langle I \rangle + \frac{\Delta I}{2} J_1(\Psi_0) \quad (27)$$

Where ω_m is the excitation frequency of the PEM. The Bessel function describes how well the PEM can switch between the s- and p-polarized light. It also influences the background.

In this surface sensitive method, the absorption is dependent on the orientation of the transition dipole moments of adsorbed molecules with respect to the surface normal. The infrared radiation can interact only with the molecules that have a component of the transition dipole moment $\vec{\mu}$. The interaction between infrared radiation and the sample becomes stronger the larger the overlap of \vec{E} and $\vec{\mu}$. The intensity of the absorption A (equation (28)) depends on the angle θ between its transition dipole moment and the electric field vector of the light:

$$A \propto |\vec{E}_z|^2 |\vec{\mu}|^2 \cos^2 \theta \quad (28)$$

The absorption is at a maximum when the above-described vectors are parallel. The intensity of absorption spectra allows determination of the molecular orientation of the studied molecular monolayers.

Typical PM IRRAS spectra are shown in Fig. 22. The ordinate shows the absorption, the abscissa the wavenumber in cm^{-1} . The two regions of interest in PM IRRAS spectra are the CH stretching mode (from 2700 cm^{-1} to 3100 cm^{-1}) in which orientation of the layers can be determined and the fingerprint region (1500 cm^{-1} to 900 cm^{-1}) where mainly vibrations of specific functional groups of SAMs are found. Both regions require different settings of half-wave retardation at the PEM.

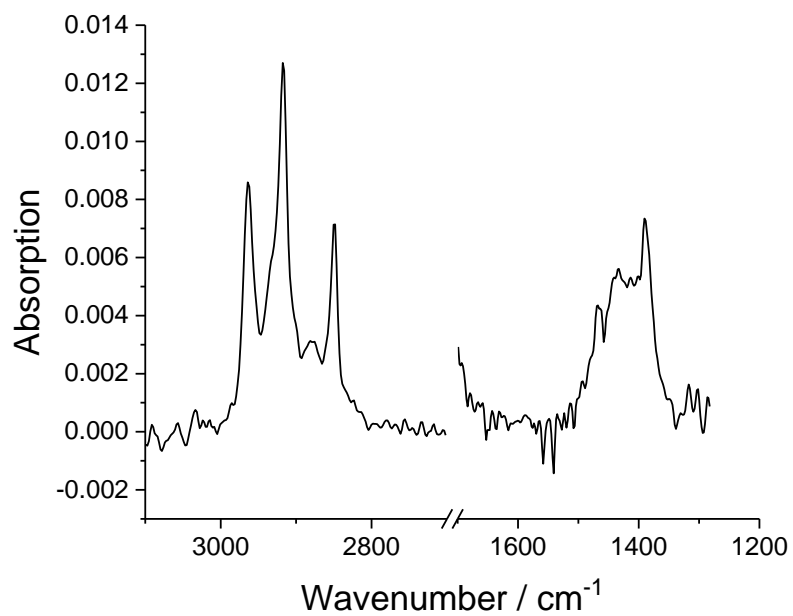


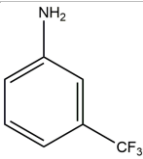
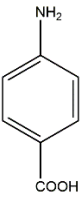
Fig. 22: PM-IRRAS spectra of arachidic acid molecular monolayer on gold substrate in CH stretching and fingerprint region.

4 Experimental details

4.1 Chemicals

In Tab. 2 are listed chemicals used in this thesis. If not stated otherwise, all chemicals were of analytical grade and were used without further purification. Aqueous solutions were prepared using deionized water (ELGA LabWater, Celle) with a resistance of 18.3 M Ω cm at room temperature. All used solutions were freshly prepared from thoroughly dried solvents. Argon was used for deaeration of the solution. Tetrabutylammonium hexafluorophosphate and tetrabutylammonium perchlorate were dried in an oven at 100 °C overnight. Acetonitrile and tetrahydrofuran were dried according to standard procedures [139] prior to use and stored under nitrogen. Ferrocene was resublimated two times.

Tab. 2: Chemicals used for surface preparation as well as for sample treatment and characterization.

Product	Formula	Supplier	Grade
tetrabutylammonium hexafluorophosphate	$(\text{CH}_3\text{CH}_2\text{CH}_2\text{CH}_2)_4\text{N}(\text{PF}_6)$	Sigma Aldrich	99.0%
silver perchlorate	AgClO_4	Sigma Aldrich	98.0%
acetonitrile	MeCN	Fisher Chemicals	HPLC grade
tetrahydrofuran	$\text{C}_4\text{H}_8\text{O}$	Fisher Chemicals	HPLC grade
tetrabutylammonium perchlorate	$(\text{CH}_3\text{CH}_2\text{CH}_2\text{CH}_2)_4\text{N}(\text{ClO}_4)$	Sigma Aldrich	99.0%
ferrocene	$\text{Fe}(\text{C}_5\text{H}_5)_2$	Alfa Acer	99.0%
dichloromethane	CH_2Cl_2	Fisher Chemicals	analytical grade
silver nitrate	AgNO_3	Carl Roth	99.9%
ethanol	EtOH	Fisher Chemicals	analytical grade
perchloric acid	HClO_4	ACS reagent	70.0-72.0 %, p.a.
potassium hydroxide	KOH	Riedel-de Haen	analytical grade
3-(trifluoromethyl)aniline		Sigma Aldrich	99.0%
4-aminobenzoic acid		Sigma Aldrich	99.0%
1-decanethiol	$\text{C}_{10}\text{H}_{22}\text{S}$	Sigma Aldrich	96.0%
1-hexanethiol	$\text{C}_6\text{H}_{14}\text{S}$	Fluka	95.0%

[(Cp₂Ti)₃HATN(Ph)₆] was synthesized as reported [31]. Compound **1**, **2**, **3**, **4**, **5**, **6**, **7**, **8**, **9**, **10** and **11** were prepared by Leon Buschbeck and Lena Freimuth as reported in [140, 141].

4.2 Electrochemical measurements

4.2.1 Electrochemical measurements of the trinuclear titanium complexes

Electrochemical setups have been installed in a glovebox and connected to instruments outside the box via gas-tight integration of cables into a flange connector (M. Braun). Cyclic voltammograms and differential pulse voltammograms were recorded at 295 K using a potentiostat (Compactstat, Ivium Technologies, Eindhoven, The Netherlands) with a three-electrode assembly with an Au disc as working electrode (WE, diameter $d = 2$ mm), a Pt plate as auxiliary electrode (Aux, $A = 1$ cm²) and a Ag/Ag⁺ reference electrode filled with 0.01 M AgClO₄ and 0.1 M Bu₄NClO₄ in THF.

4.2.2 Electrochemical measurements of DATs in solution

The electrochemical experiments were carried out in a custom-made electrochemical cell that was air sealed. All solutions were purged with argon 45 min before measurements. Cyclic voltammograms were recorded at 295 K using a potentiostat (Metrohm Autolab, Utrecht, Netherlands) with a three-electrode assembly comprising a GC disc as working electrode (WE, diameter $d = 3$ mm), a Pt plate as auxiliary electrode (Aux, $A = 1$ cm²) and an Ag/Ag⁺ reference electrode filled with 0.01 M silver nitrate and 0.1 M Bu₄NClO₄ in MeCN.

4.2.3 Determination of formal potentials

The formal potentials E° were obtained from cyclic voltammograms using eq. (2). They are quoted with respect to the ferrocene/ferrocenium redox couple (Fc/Fc⁺) which was measured in the solution with the same concentration of supporting electrolyte and the concentration of the Fc (0.3 mM) as the compound under investigation.

4. 2. 4 Electrochemical measurements on surfaces

The electrochemical experiments were carried in a custom-made electrochemical cell (Fig. 23). All solutions were purged with argon 45 min before measurements.

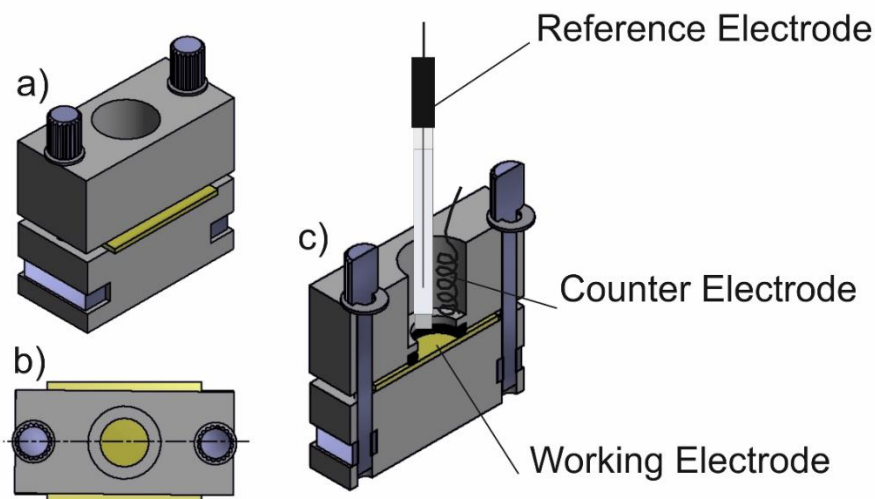


Fig. 23: Electrochemical cell made from Teflon in three different views a) from the front, b) from the top and c) the vertical cross-section area showing the arrangement of the reference, counter and working electrode. (prepared by the mechanical workshops of Carl von Ossietzky University of Oldenburg)

Measurements were recorded at 295 K using a potentiostat (Metrohm Autolab, Utrecht, Netherlands) with a three-electrode assembly comprising a gold sample as working electrode pressed against an O-ring for sealing (WE, diameter of O-ring $d = 6$ mm), a Pt plate as auxiliary electrode (Aux, $A = 1$ cm²) and a mercury sulphate reference electrode. All potentials in the cyclic voltammograms were recalculated to standard hydrogen electrode (SHE).

4. 2. 5 Spectroelectrochemistry

Spectroscopic setups have been installed in a glovebox and connected to instruments outside the box via gas-tight integration of cables and optical fibres into a flange connector (M. Braun). NIR spectra were measured with a fiber-coupled Matrix-F FT-NIR spectrometer (Bruker Optik GmbH, Ettlingen, Germany) equipped with a halogen lamp as NIR source and an InGaAs detector. Spectra were taken in the range from 12000 to 4000 cm⁻¹ with a resolution of 8 cm⁻¹. For each measurement 16 scans were accumulated. UV-Vis spectra were taken with a GetSpec 2048 CCD array spectrometer (GetSpec,

Sofia, Bulgaria). The device configuration allowed a resolution of 2.4 nm in the range of 200 to 1000 nm. For the measurements, an integration time of 100 ms was used. Both spectrometers were coupled to a spectroelectrochemical cell (ALS Co., LTD, Tokyo, Japan) located inside an Ar-filled glove box (Fig. 24) using 600 μm -diameter N227 quartz fibers (Bruker Optik GmbH).

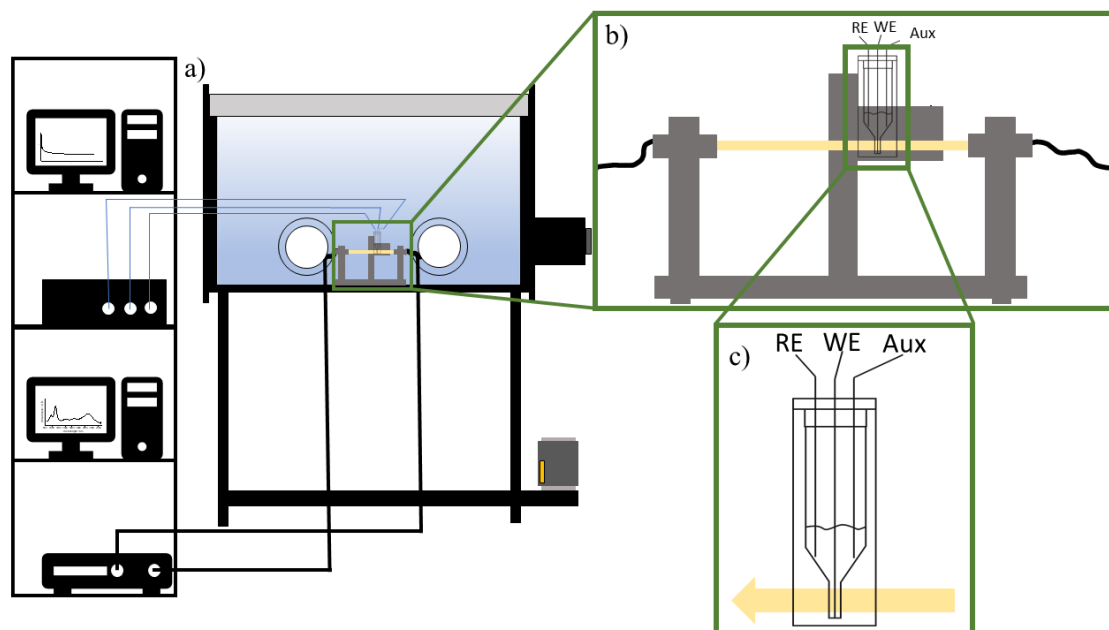


Fig. 24: Experimental setup for spectroelectrochemical measurement: a) scheme of setup in the glove box and their connection with spectrometer (black lines) and potentiostat (blue line), b) magnification of spectroelectrochemical setup, c) magnification of spectroelectrochemical cell where WE is an optically transparent working electrode, RE is the reference electrode, CE is the counter electrode, yellow arrow represents the path of light beam.

4. 2. 6 Absorption and fluorescent spectroscopy of DATs

The absorption spectra were measured at Spekol 2000 (Analytik Jena, Jena, Germany) and fluorescent emission spectra were measured at the FS5 spectrofluorometer (Edinburgh Instruments, Livingston, United Kingdom). All DAT compounds were dissolved in ethanol to a concentration of 0.9 μM . The reference spectra were taken from pure ethanol.

4. 3 General cleaning procedure

Glass slides were ordered from VWR International (Darmstadt, Germany). In order to remove contaminations, glass substrates were washed with ethanol and water and dried in an argon stream. Subsequently, the surfaces were oxidized by UV/O₃ for 15 min using the UV TipCleaner (UV.TC.EU.003, Bioforce Nanoscience, Inc. Ames, IA, USA).

4.4 Preparation of gold surfaces

Gold surfaces were prepared onto cleaned glass slides as the support by depositing 0.5 nm of chromium and 200 nm of gold using an evaporation chamber (minicoater, Tectra GmbH, Frankfurt, Germany) while monitoring the thicknesses of deposited layers with a quartz crystal microbalance (Tectra GmbH, Frankfurt, Germany). The gold substrates were freshly prepared prior to each experiment.

4.5 Preparation of SAMs

Freshly evaporated gold/glass slides without any cleaning were put in 0.1 mM solution containing DAT of choice in ethanol. They were left in solution for 48 h. Then gold/glass slides were put in 0.1 mM solution of 1-decanthiol or 1-hexanethiol in ethanol for 24 h (the choice of the thiol was dependent of the DAT derivative that was previously adsorbed on gold/glass slide). Afterwards, samples were washed with ethanol and dried under an argon stream.

4.6 Characterization of surfaces

4.6.1 X-ray photoelectron spectroscopy (XPS)

XPS was performed with an ESCALAB 250 iX (Thermo Fischer, East Grinstead, UK) using a monochromatized Al K_α excitation (1486.6 eV). Data acquisition and spectra processing were performed with the Advantage Software v.5.979. Au, O, F, N, C, S were detected in the samples, the most intense lines from those elements were obtained as high-resolution spectra. Measurements of the SAMs were performed before and after electrochemical treatment. The spectra were fitted by applying a smart background and a

sum of Gaussian and Lorentzian contributions in the software Avantage (v.5.979, Thermo Fisher, UK). The used parameters are listed in Tab. 3.

Tab. 3 Experimental parameters for the XPS measurement of SAMs

Element	Number of scans	Pass energy /eV	Spot size / μm	Step size /eV	Dwell time /ms
C	10	30	900	0.05	50
N	30	30	900	0.05	50
S	15	30	900	0.05	50
Au	3	30	900	0.05	50
O	15	30	900	0.05	50
F	15	30	900	0.05	50

4. 6. 2 Polarization modulation infrared reflection adsorption spectroscopy (PM IRRAS).

This technique was used to characterize mixed SAMs prepared from derivatives of DATs and 1-decanethiol or 1-hexanethiol. PM IRRAS spectra were acquired by the utilization of a Vertex 70 spectrometer and an external reflection setup (Bruker, Ettlingen, Germany) containing a photoelastic modulator (PEM) PMA 50 (Hinds Instruments, Hillsboro, OR, USA). The half wave retardation was set to 1600 cm^{-1} or to 2900 cm^{-1} . For each measurement 1200 scans were accumulated. The resolution of the spectra was 4 cm^{-1} . The PM IRRAS spectra were baseline corrected by a Bessel function using the OPUS software version 5.5 (Bruker, Germany). A detailed procedure is described in Ref. [142].

5 Electrochemical and spectroelectrochemical studies on electron transfer reactions of $[(\text{Cp}_2\text{Ti})_3\text{HATN}(\text{Ph})_6]$

The following chapter describes electrochemical and spectroelectrochemical characterization of the trinuclear 5,6,11,12,17,18- hexaazatrinaphthylene (HATNPh_6)-bridged titanium complex $[(\text{Cp}_2\text{Ti})_3\text{HATN}(\text{Ph})_6]$. This complex and corresponding ligand were prepared by Pia Sander of the group of Prof. Dr. Rüdiger Beckhaus from the University of Oldenburg. The first part of collaborative work was published in Inorganic chemistry [31]. The electrochemical measurement of the complex and the spectroscopic measurement of chemically oxidized species in UV-vis and NIR region were carried out by the thesis author. The second paper is in preparation, for which the entire experimental work was performed by the thesis author. The thesis author also prepared the manuscript draft, which was checked by the co-authors.

5.1 Electrochemical studies of $[(\text{Cp}_2\text{Ti})_3\text{HATN}(\text{Ph})_6]$

Trinuclear titanocene(II) complexes include formally three titanocene(II) fragments with two d-electrons, i.e. they potentially contain six d-electrons. Piglosiewicz and co-authors could electrochemically achieve six oxidations and two reductions in the compound $[(\text{Cp}_2\text{Ti})_3\text{HATN}(\text{Me})_6]$ [19]. They have also measured the cyclic voltammogram of the ligand and found two reductions [19]. Because of its low solubility, further spectroscopic investigations for a deeper understanding of mixed-valent titanium complexes were not possible. In the $[(\text{Cp}_2\text{Ti})_3\text{HATN}(\text{Ph})_6]$ the methyl groups are replaced by phenyl groups. This increases the solubility of the complex, especially in toluene and THF. Using ferrocenium salts, Sander et al. [31] were able to oxidize $[(\text{Cp}_2\text{Ti})_3\text{HATN}(\text{Ph})_6]$ to the 3^+ total charge, but chemical reduction of complex was not possible.

As $[(\text{Cp}_2\text{Ti})_3\text{HATN}(\text{Ph})_6]$ is very sensitive to air and moisture all measurements were done in the glovebox. Although the neutral compound is not stable in air, its oxidized products are not sensitive to air and moisture.

The cyclic voltammetry and the differential pulse voltammetry of $[(\text{Cp}_2\text{Ti})_3\text{HATN}(\text{Ph})_6]$ were recorded in THF with 0.2 M Bu_4NPF_6 as supporting electrolyte. The differential pulse voltammetry was started at the OCP in positive directions in order to record the oxidations. The signals are shown in pink. Another scan was conducted in negative direction in order to record the reduction current (shown in blue). The potential range, in which the neutral complex was stable, is coloured in orange, the potential range of the negatively charged species are marked in blue and potential ranges in which the positively charged species are stable are marked in pink. The differential pulse voltammograms are overlaid with the cyclic voltammogram because they show a better resolution of the redox processes. Differential pulse voltammogram and cyclic voltammogram have separated ordinates in Fig. 25.

The voltammogram of $[(\text{Cp}_2\text{Ti})_3\text{HATN}(\text{Ph})_6]$ shows multiple electron transfer reactions, three reduction waves and six oxidation waves. All steps are one electron processes (Fig. 25). The six oxidations correspond to the six valence electrons of the three Ti(II) centre. The half-wave potentials extracted from these voltammograms are shown in Tab. 4 and are compared to those of the $[(\text{Cp}_2\text{Ti})_3\text{HATN}(\text{Me})_6]$ [19]. The three reduction waves can be described as well-separated one-electron-reduction steps. In comparison to $[(\text{Cp}_2\text{Ti})_3\text{HATN}(\text{Me})_6]$ [19] one additional redox step is observed. The formal potential for the different redox processes of $[(\text{Cp}_2\text{Ti})_3\text{HATN}(\text{Me})_6]$ are more negative than their equivalents in $[(\text{Cp}_2\text{Ti})_3\text{HATN}(\text{Ph})_6]$ in $0 \rightarrow -1$ and $-1 \rightarrow -2$ steps. A third reduction step is not so unusual in this field of HAT or HATN complexes [22]. Until the $+3 \rightarrow +4$ oxidation step, the oxidation waves are well separated, while the couples $+4 \rightarrow +5$ and $+5 \rightarrow +6$ overlap slightly. In analogy to the reduction steps, also the formal potentials have higher values when compared to those of $[(\text{Cp}_2\text{Ti})_3\text{HATN}(\text{Me})_6]$ [19]. Therefore, $[(\text{Cp}_2\text{Ti})_3\text{HATN}(\text{Ph})_6]$ is more stable than $[(\text{Cp}_2\text{Ti})_3\text{HATN}(\text{Me})_6]$. Until today the nine reversible redox steps of $[(\text{Cp}_2\text{Ti})_3\text{HATN}(\text{Ph})_6]$ are unprecedented in literature.

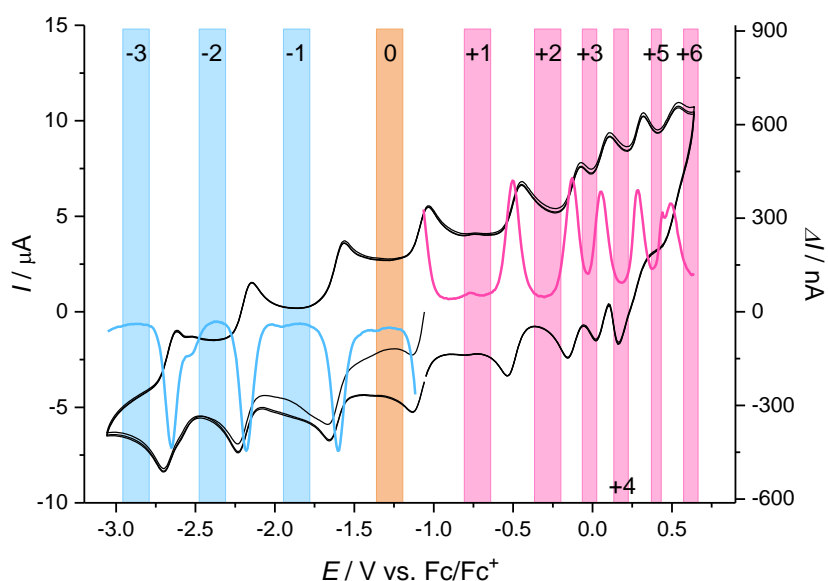


Fig. 25: Cyclic voltammogram (black) and differential pulse voltammogram (pink, blue) of 0.3 mM $[(\text{Cp}_2\text{Ti})_3\text{HATN}(\text{Ph})_6]$ at an Au working electrode in 0.2 M Bu_4NPF_6 in THF.

Tab. 4: Formal potentials (vs. Fc/Fc^+) for electron transfer reactions of $[(\text{Cp}_2\text{Ti})_3\text{HATN}(\text{Ph})_6]$ from the data in Fig. 25.

change of overall charge	E°/V $\text{Ti}_3\text{-HATN}(\text{Ph})_6$	E°/V $\text{Ti}_3\text{-HATN}(\text{Me})_6$ [19]
-3/-2	-2.66	
-2/-1	-2.19	-2.21
-1/0	-1.61	-1.74
0/1	-1.08	-1.27
1/2	-0.49	-0.54
2/3	-0.12	-0.30
3/4	+0.06	+0.11
4/5	+0.24	+0.18
5/6	+0.49	+0.40

Cyclic voltammogram and differential pulse voltammogram of ligand alone are recorded in a mixture 50% THF and 50% MeCN due to the low solubility of the ligand with 0.2 M Bu_4NPF_6 as supporting electrolyte. The ligand shows two reduction steps at -1.50 V and -1.66 V vs. Fc/Fc^+ . By comparison of the voltammetric data of the complex (Fig. 25) with the ligand $\text{HATN}(\text{Ph})_6$ (Fig. 26), the reductions $0 \rightarrow -1$ and $-1 \rightarrow -2$ can be tentatively assigned to the reduction of the ligand. The reductions in $[(\text{Cp}_2\text{Ti})_3\text{HATN}(\text{Ph})_6]$ occurs at more negative potentials than in the isolated ligand $\text{HATN}(\text{Ph})_6$ because the complexation increases the electron density at the ligand and

makes further reductions more difficult. For the reduction $-2 \rightarrow -3$, the assignment is not certain from voltammetric data alone.

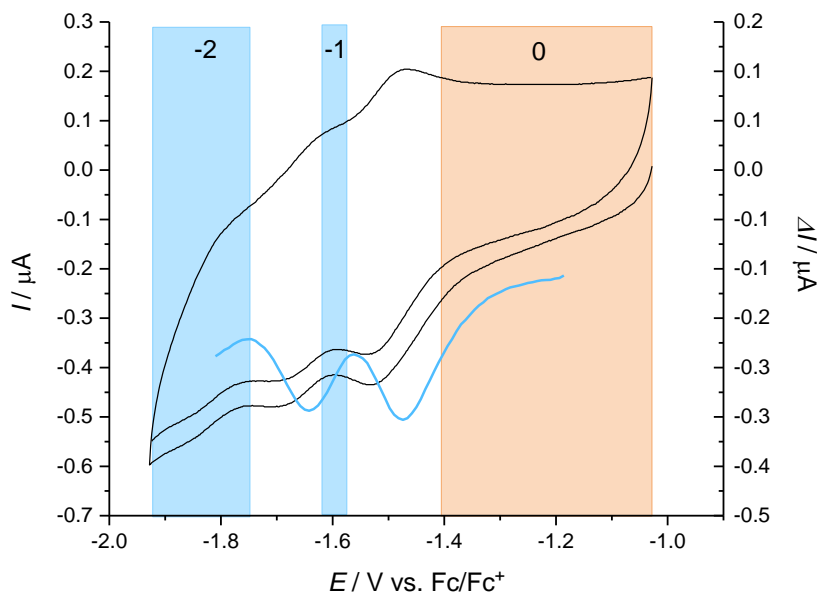


Fig. 26: Cyclic voltammogram (black) and differential pulse voltammogram (blue) of 0.1 mM [HATN(Ph)₆] at an Au disc working electrode in 0.2 M Bu₄NPF₆ in mixture of 50 vol-% THF and 50 vol-% MeCN.

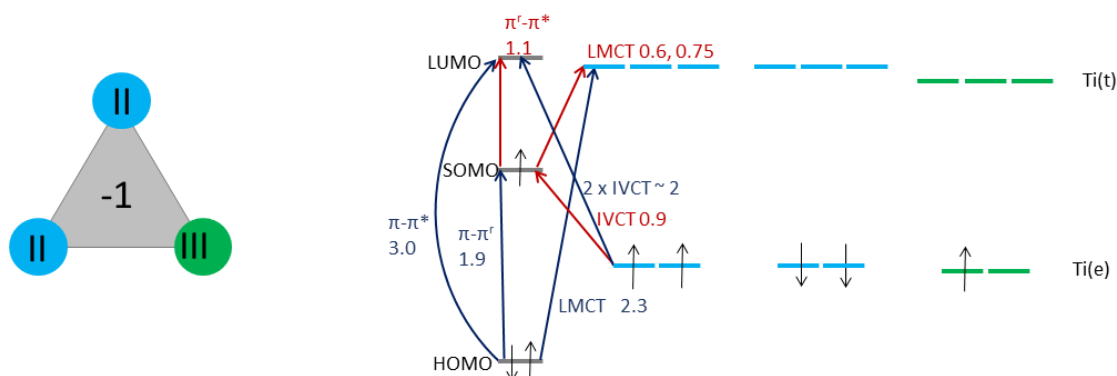
5.2 Spectroelectrochemical measurements

The solution spectra of [(Cp₂Ti)₃HATN(Ph)₆] (Fig. 27b) and its oxidation and reduction products [(Cp₂Ti)₃HATN(Ph)₆]³⁻ (Fig. 32b), [(Cp₂Ti)₃HATN(Ph)₆]²⁻ (Fig. 31b), [(Cp₂Ti)₃HATN(Ph)₆]¹⁻ (Fig. 30b), [(Cp₂Ti)₃HATN(Ph)₆]¹⁺ (Fig. 28b) and [(Cp₂Ti)₃HATN(Ph)₆]²⁺ (Fig. 29b) show electronic transitions in the UV, vis and NIR spectral ranges.

From the magnetic measurement of our collaboration partners and their conclusion based on the results from the magnetic measurement [31], there are two Ti(II) centers, one Ti(III) center and a single occupied molecular orbital (SOMO) of the ligand in the ground state of [(Cp₂Ti)₃HATN(Ph)₆]. The SOMO is populated by a single electron transferred from one of the Ti centers to the HATN(Ph)₆ ligand. This electronic structure allows several very characteristic electronic transitions. Spectra in UV-vis and NIR region are shown in Fig. 27b and the schematic representation of orbitals with the proposed transitions which is in correspondence with spectra is shown on the Fig. 27a. The assignment of the transitions for all states of charge was obtained by comparing spectra

and orbitals of the complex in the same charge state. For a confirmation of the assignment, theoretical calculations are necessary. In the ground state of the complex in the UV-vis part of the spectra one can see the π - π^* transition from the HOMO to the LUMO orbital of the ligand at around 3.0 eV. In this region, there are also the π - π^\dagger transition from the HOMO to the SOMO orbital at around 1.9 eV, ligand to metal charge transfer (LMCT) from the HOMO orbital of the ligand to Ti(t) at around 2.3 eV, and the degenerated intervalence charge transfer (IVCT) from the Ti(II)(e) to the LUMO orbital of the ligand at around 2 eV. For the same oxidation state, the NIR region of the spectra shows the π^\dagger - π^* transition from the SOMO to the LUMO orbital at 1.1 eV, LMCT at 0.6 eV and 0.75 eV and the IVCT from the Ti(II)(e) to the SOMO orbital of the ligand at around 0.9 eV which can be relaxed to the Ti(II)(e) or the Ti(III)(e) orbital. The signals at 0.50 eV, 0.68 eV and 0.90 eV are overtones of molecular vibration of the solvent, which are not fully compensated.

a)



b)

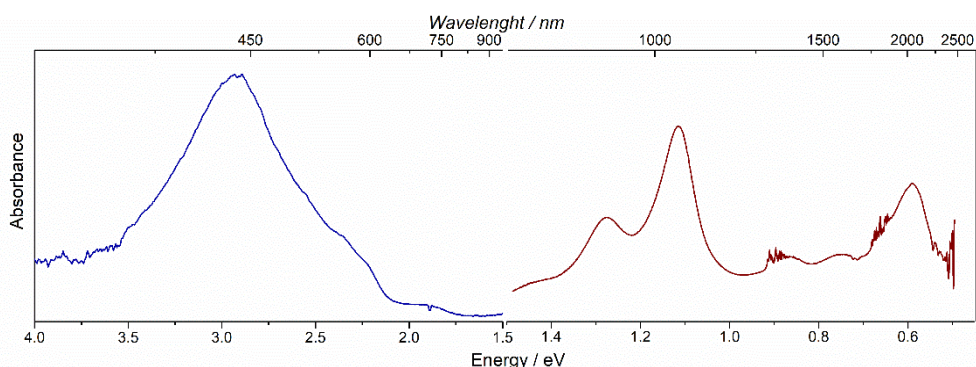


Fig. 27: a) orbital energy diagram and transitions (in eV) observed in electronic spectra in the visible and NIR range for $[(\text{Cp}_2\text{Ti})_3\text{HATN}(\text{Ph})_6]$, b) the spectra from the spectroelectrochemical measurements of $[(\text{Cp}_2\text{Ti})_3\text{HATN}(\text{Ph})_6]$ in THF; UV/Vis in blue and NIR in red.

In the first oxidation (change from overall charge 0 to +1), we assumed that an electron is removed from the SOMO orbital which becomes the new LUMO orbital

(denoted as LUMO' in Fig. 28a). This charge state has two π - π^* transitions from the HOMO to the LUMO' and the LUMO orbital at around 2.5 eV and 2.9 eV (Fig. 28b). The NIR part of the spectra is characterized by two IVCTs from the Ti(II)(t) and Ti(III)(t) to the LUMO' at 0.9 eV and 1.1 eV, and two IVCTs from the Ti(II)(t) and Ti(III)(t) to the LUMO at 1.05 eV and 1.25 eV.

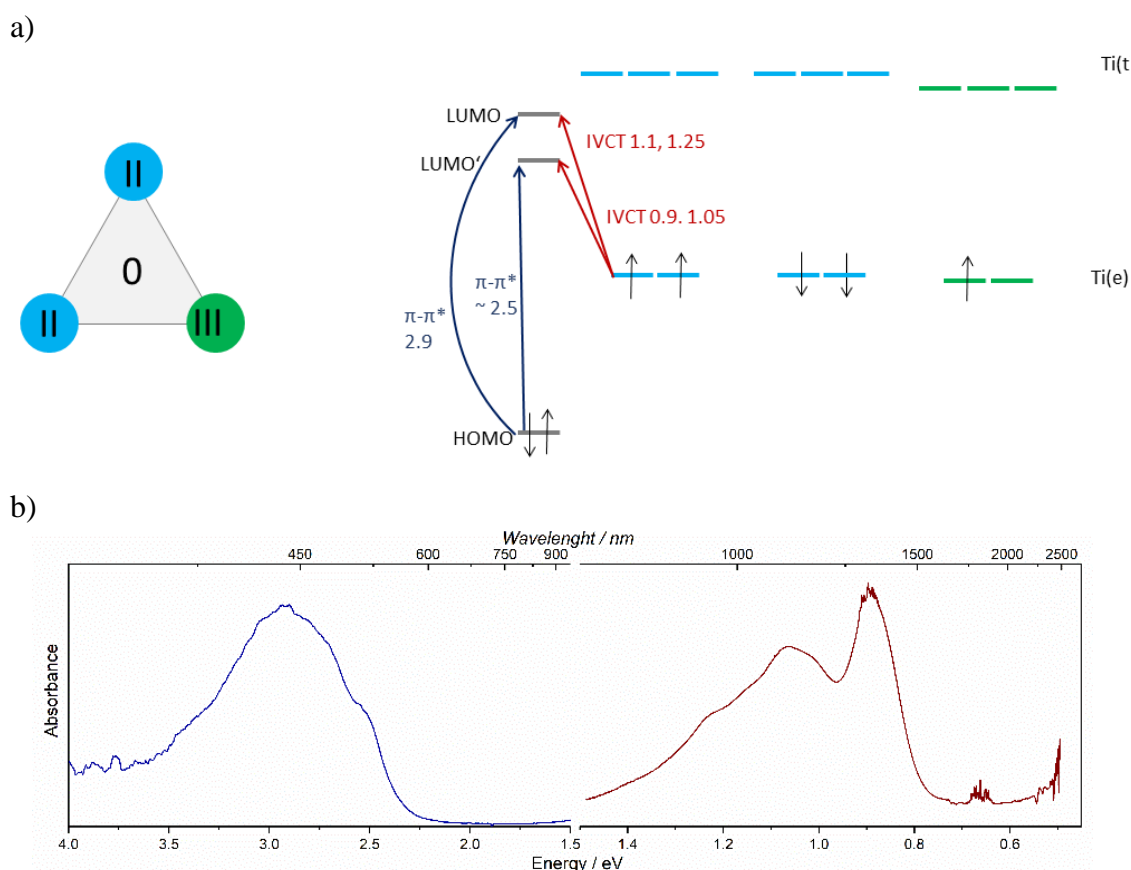


Fig. 28: a) orbital energy diagram and transitions (in eV) observed in electronic spectra in the visible and NIR range for $[(\text{Cp}_2\text{Ti})_3\text{HATN}(\text{Ph})_6]^{1+}$, b) the spectra from the spectroelectrochemical measurements of $[(\text{Cp}_2\text{Ti})_3\text{HATN}(\text{Ph})_6]^{1+}$ in THF; UV/Vis in blue and NIR in red.

In the next oxidation step (overall charge +1 to +2), an electron is removed from one Ti(II)(t) orbital (Fig. 29a). All transitions which are assigned in this charge states are also assigned in previously discussed one (Fig. 28a). Transitions in Fig. 29b are slightly shifted to lower energies. The IVCT cannot be seen clearly as in the previous charge state (Fig. 29b), there is only a general rise in absorption in the NIR part of the spectra which indicates those transitions.

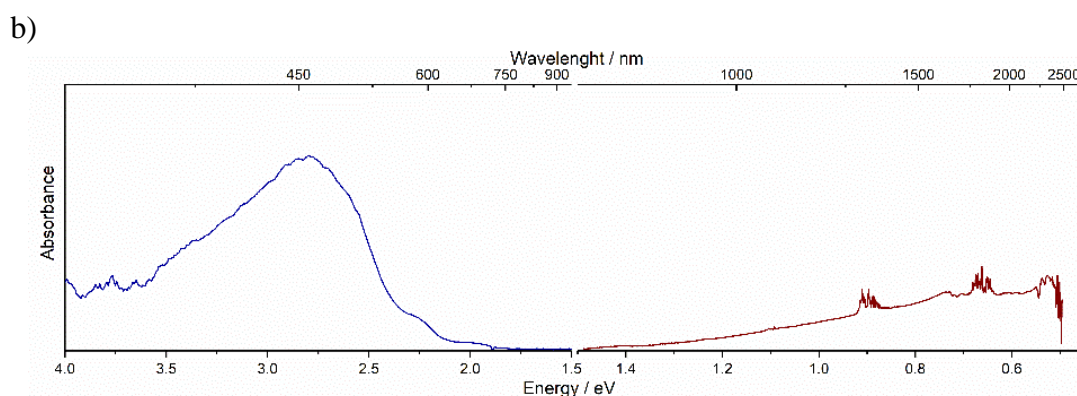
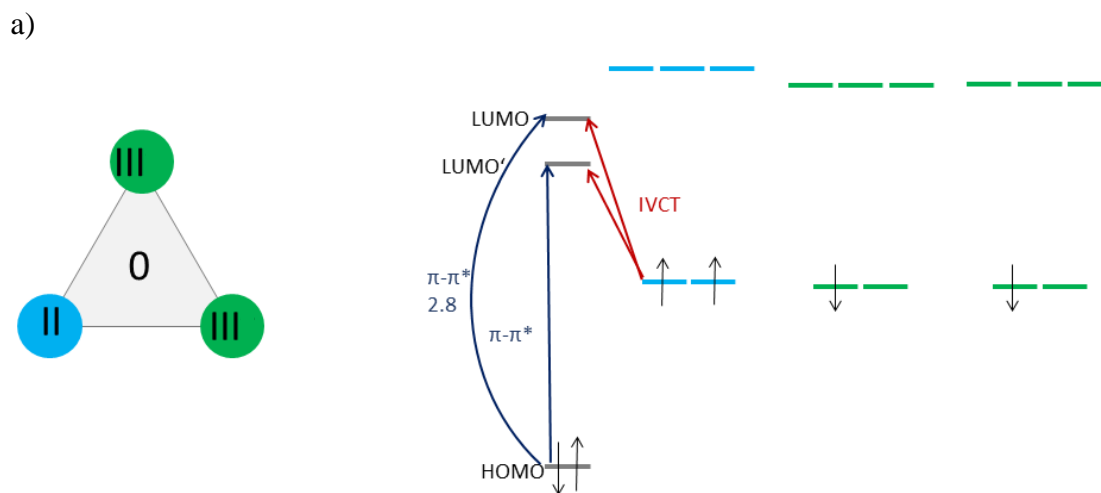


Fig. 29: a) orbital energy diagram and transitions (in eV) observed in electronic spectra in the visible and NIR range for $[(\text{Cp}_2\text{Ti})_3\text{HATN}(\text{Ph})_6]^{2+}$, b) the spectra from the spectroelectrochemical measurements of $[(\text{Cp}_2\text{Ti})_3\text{HATN}(\text{Ph})_6]^{2+}$ in THF; UV/Vis in blue and NIR in red.

In the first reduction (overall charge 0 to -1), an electron is added to the Ti(III)(t) orbital and as a consequence in this charge state the complex is not a mixed valence system (Fig. 30a). Therefore, all the IVCT are metal-ligand charge transfers (MLCT). In the NIR part of the spectra, one can see the MLCT at 0.75 eV, the $\pi^r-\pi^*$ at 1.1 eV. The LMCT from the SOMO orbital of ligand to the Ti(t)(II) orbital is not observed in the recorded wavelength range, but one can see the rise in absorption which indicates that there is a transition in the energy range below 0.5 eV (Fig. 30b). In the UV-vis range, one can see the $\pi-\pi^*$ transition at 2.8 eV, the $\pi^r-\pi^r$ at 1.7 eV and the LMCT from the HOMO orbital of the ligand to the Ti(t)(II) orbital at 2.4 eV.

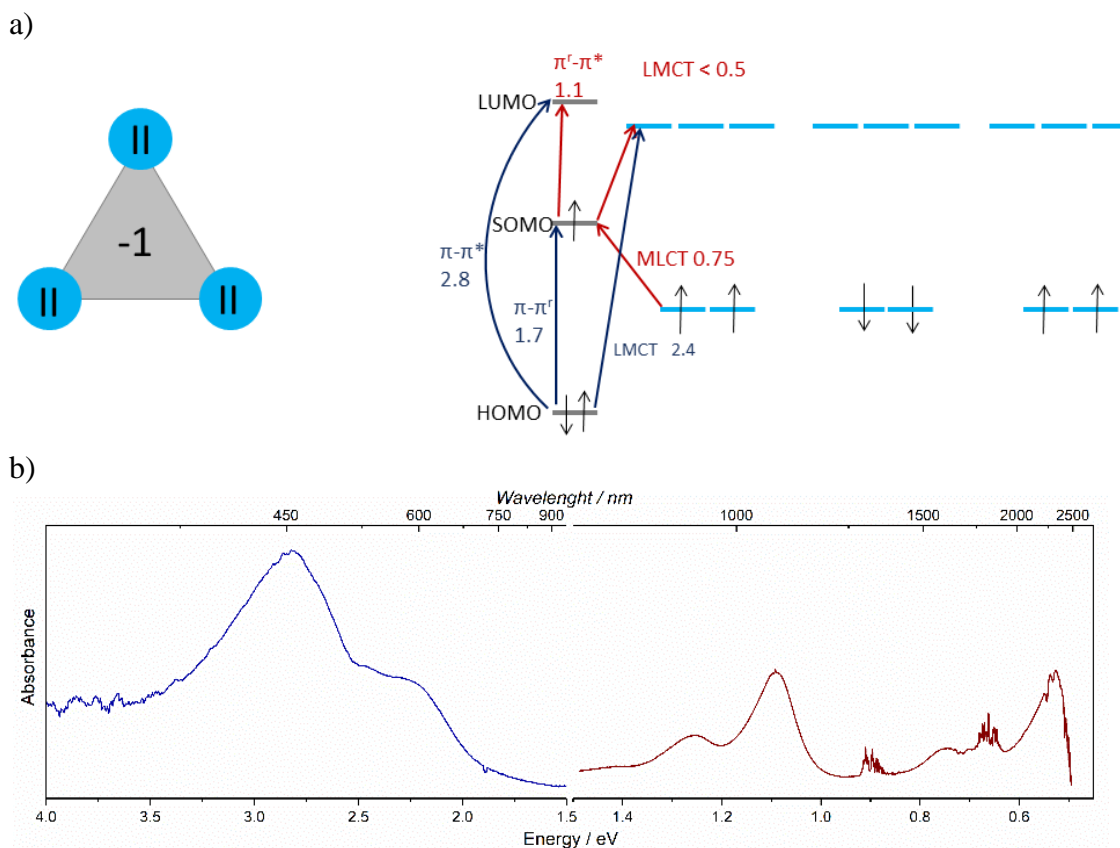


Fig. 30: a) orbital energy diagram and transitions (in eV) observed in electronic spectra in the visible and NIR range for $[(\text{Cp}_2\text{Ti})_3\text{HATN}(\text{Ph})_6]^{1-}$. b) the spectra from the spectroelectrochemical measurements of $[(\text{Cp}_2\text{Ti})_3\text{HATN}(\text{Ph})_6]^{1-}$ in THF; UV/Vis in blue and NIR in red.

In the second reduction (overall charge state -1 to -2), an electron is transferred into the SOMO orbital of the ligand and this orbital becomes the new HOMO orbital (denoted as HOMO' orbital in Fig. 31a). In this charge state, some transitions are lost (Fig. 31b). One can still see two $\pi-\pi^*$ transitions from the HOMO and the HOMO' to the LUMO orbital at 2.6 eV and 0.8 eV as well as the MLCT from the Ti(e)(II) to the LUMO orbital at 1.7 eV. The LMCT from the HOMO to the Ti(t)(II) is at 2.2 eV. However, the LMCT from the HOMO' to the Ti(t)(II) cannot be observed, yet there is a rise in absorption which indicate that there is the transition at energies below 0.5 eV.

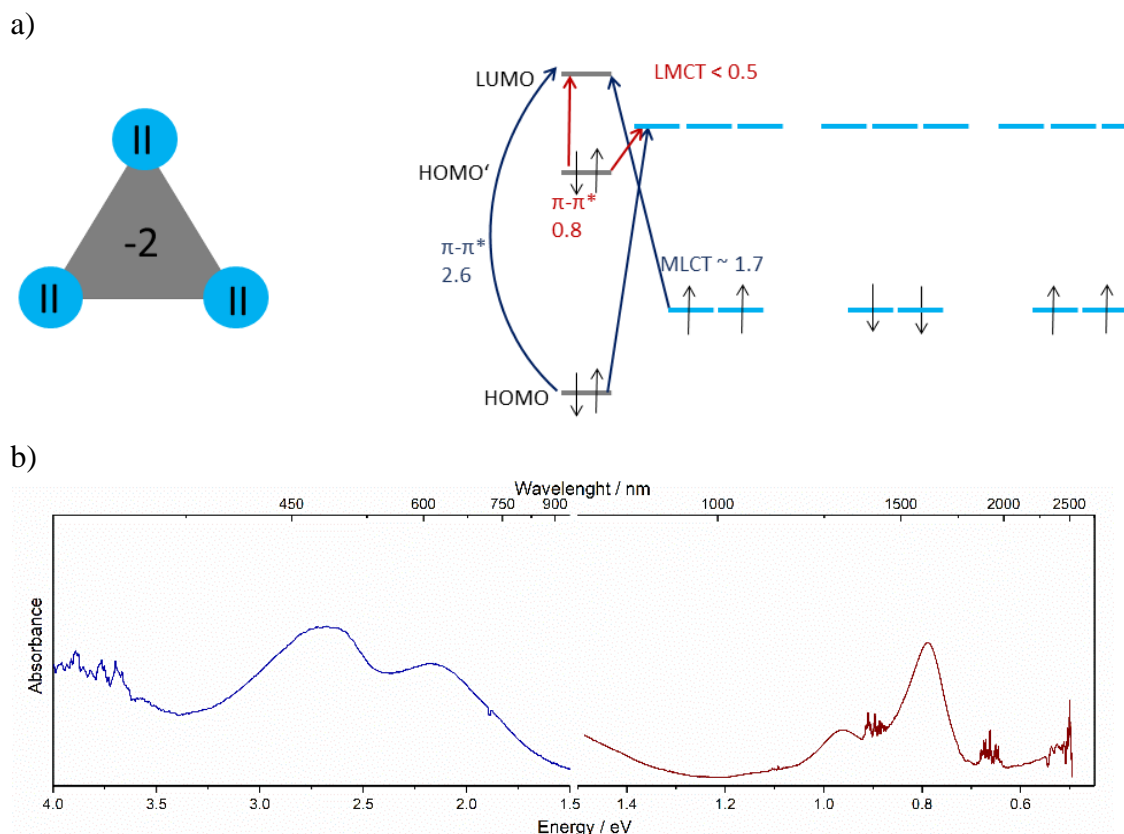


Fig. 31: a) orbital energy diagram and transitions (in eV) observed in electronic spectra in the visible and NIR range for $[(\text{Cp}_2\text{Ti})_3\text{HATN}(\text{Ph})_6]^{2-}$, b) the spectra from the spectroelectrochemical measurements of $[(\text{Cp}_2\text{Ti})_3\text{HATN}(\text{Ph})_6]^{2-}$ in THF; UV/Vis in blue and NIR in red.

In the third reduction, an electron is accepted by one of the Ti centers (Fig. 32a). In this charge state there are two Ti(II) and one Ti(I). The accepted electron in orbitals of Ti(I) can be in low or high spin configuration. A magnetic measurement for this charge state of the complex was not performed and because of that the exact placement of the electron cannot be determined. In literature the magnetic moment for tris-2,2'-dipyridylvanadin(0) ($[\text{VDipy}_3]$) [143] is known in which titanium is in Ti(I) state. This measurement suggests that the low spin configuration of $[\text{VDipy}_3]$ is preferable. From this literature data it can be tentatively concluded that for $[(\text{Cp}_2\text{Ti})_3\text{HATN}(\text{Ph})_6]$ the low spin state is also preferable. The assignment of transitions is similar to that of the -2 charge state. The only difference is the IVCT from the Ti(e)(II) to the LUMO orbital (Fig. 32b), which was in previous charge state MLCT because the complex again becomes the mixed valence system.

Because of the complexity of $[(\text{Cp}_2\text{Ti})_3\text{HATN}(\text{Ph})_6]$ and the spectroscopic data for confirmation of transition assignment theoretical calculations are necessary. Calculations would provide relatively accurately insight into the electronic properties of

such systems. Orbital diagrams constructed from theoretical calculation data could confirm the accuracy of the orbital diagrams in Fig. 27a, Fig. 28a, Fig. 29a, Fig. 30a, Fig. 31a and Fig. 32a that were constructed using experimental data of $[(\text{Cp}_2\text{Ti})_3\text{HATN}(\text{Ph})_6]$ and the orbital energy diagrams of similar compounds.

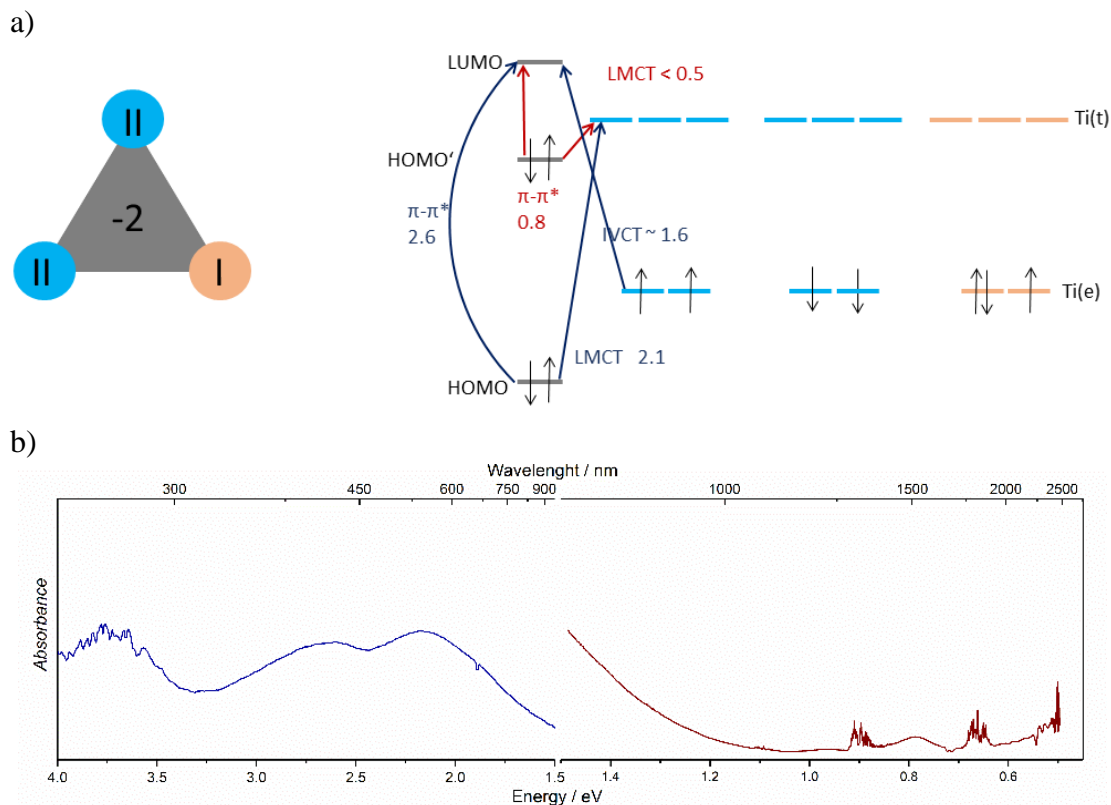


Fig. 32: a) orbital energy diagram and transitions (in eV) observed in electronic spectra in the visible and NIR range for $[(\text{Cp}_2\text{Ti})_3\text{HATN}(\text{Ph})_6]^{3-}$, b) the spectra from the spectroelectrochemical, measurements of $[(\text{Cp}_2\text{Ti})_3\text{HATN}(\text{Ph})_6]^{3-}$ in THF; UV/Vis in blue and NIR in red.

In paper published with our collaboration partners [31], the Hush formula for IVCT in trinuclear systems [144] was used for the calculation of the coupling constant $H_{\text{Ti(II)}-\text{Ti(III)}}$ for $[(\text{Cp}_2\text{Ti})_3\text{HATN}(\text{Ph})_6]$. The value of $H_{\text{Ti(II)}-\text{Ti(III)}}$ indicates delocalization between the metal centres but no full delocalization, which indicates that $[(\text{Cp}_2\text{Ti})_3\text{HATN}(\text{Ph})_6]$ is Robin–Day class II.

6 Electrochemical and spectroscopic characterization of DATs in the solution

The following Chapter describes the electrochemical characterization of derivatives of 2,5-diaminoterephthalate (DAT). Derivatives of DATs were prepared by Dr. Leon Buschbeck and Dr. Lena Freimuth from the group of Prof. Dr. Jens Christoffers from the University of Oldenburg. Different derivatives of DATs were electrochemically investigated in dichloromethane (DCM) due to their low solubility in other solvents. The electrochemical data were correlated to electronic spectra. The publication from this data is in preparation where all experimental work and writing of the manuscript was performed by this thesis author.

6.1 Electrochemistry of DATs

The DAT derivatives (Fig. 33) that are investigated in this Chapter have different substituents (marked in red in Fig. 33) that influence the electron density and modify the properties of the diamine/diimine group that is the redox-active group for this type of compounds. These molecules were used to uncover a systematic variation of the DAT electrochemical and spectroscopic properties with the variation of substituents. Compounds **2** and **7** were synthesized by Lena Freimuth [141], compounds **1**, **3**, **4**, **5** and **6** were prepared by Leon Buschbeck [140].

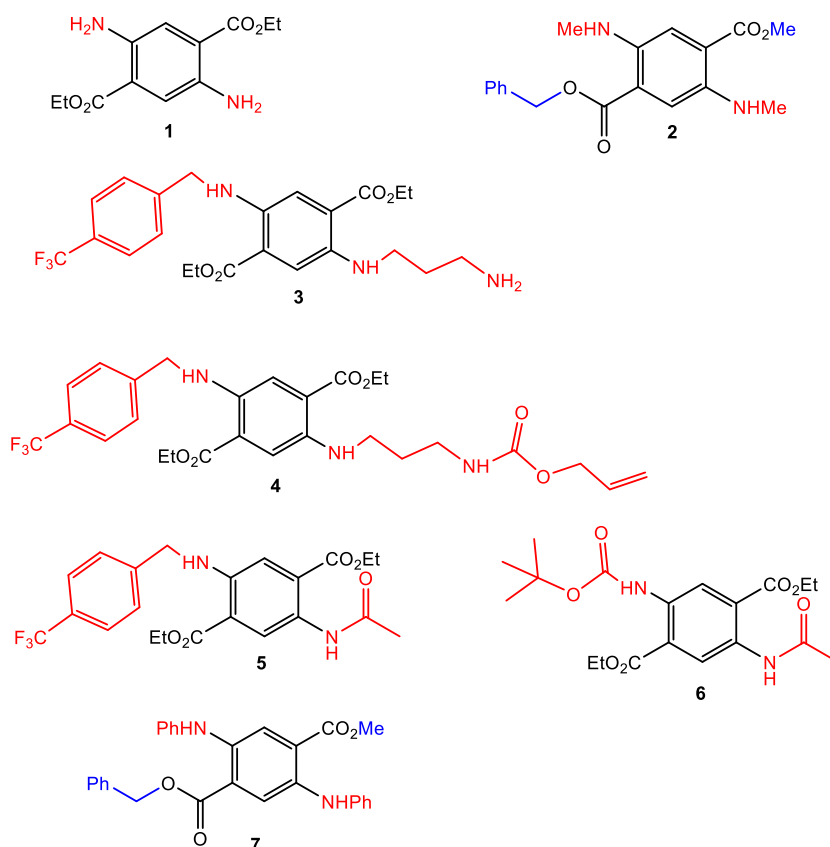


Fig. 33: Structures of DAT derivatives investigated in this study (differences in N-substitutions that influence the electrochemical behaviour are marked in red; differences at the ester groups are marked in blue).

Cyclic voltammetry was performed at the concentration of 0.3 mM of DAT derivatives in DCM solution with 0.1 M concentration of Bu_4NClO_4 as supporting electrolyte at glassy carbon (GC) working electrode. Formal potentials ($E^{\circ'}$) extracted from voltammograms recorded at the scan rate 0.1 V s^{-1} (Fig. 34, Fig. 36, Fig. 38, Fig. 40, Fig. 42, Fig. 44 and Fig. 45) are summarized in Tab. 5. The cyclic voltammograms of the DAT derivatives in all scan rates between 0.01 V s^{-1} and 1 V s^{-1} show different features of the cathodic and the anodic peaks that depend on the particular molecular structure (Fig. 35, Fig. 37, Fig. 39, Fig. 41, Fig. 43 and Fig. 46). From the recorded cyclic voltammograms, some voltammetric parameters including the peak potentials E_{pc} and E_{pa} , difference in peak potentials ΔE_{p} , the formal potential $E^{\circ'}$ and the ratio between the anodic and the cathodic current $I_{\text{pa}}/I_{\text{pc}}$ for the entire set of compounds at different scan rates were evaluated (Tab. 6). As is obvious from the data in Tab. 6, both the redox potentials and the redox behaviour of the DAT molecule are strongly dependent on the nature of the substituting groups on the mother molecule. In most cases, the first peak is quasi-reversible while the second peak is quasi-reversible or irreversible. This is

concluded from the dependence of ΔE_p on the scan rate as well as by the change of I_{pa}/I_{pc} with scan rate. The ratio of anodic to cathodic peak currents (I_{pa}/I_{pc}) is not constant in the most of the cases (Tab. 6). The formal potentials $E^{\circ'}$ are independent of the scan rate. In addition, absorption and emission spectra of the compounds are shown in Fig. 47.

Compound **1** has two unsubstituted aromatic amino groups as redox-active moiety (Fig. 33). In the potential range from -0.65 V to 0.45 V, there is one pair of oxidation and reduction peaks where a radical cation is formed and reduced to the initial compound in the negatively going scan (Fig. 34a). The value of the formal potential is 0.15 V. At slower scan rates, there is more time for the radical cation, created in oxidation peak, to enter in a chemical reaction. As a consequence, the reduction currents significantly decrease with lower scan rate (Fig. 35a). When the potential range is extended to 1.00 V vs. Fc/Fc⁺, a second oxidation peak appears at 0.82 V accompanied by a reduction peak at 0.43 V (Fig. 34b). With appearance of the second oxidation peak, the reduction current of the first redox couple are reduced indicating the consumption of the oxidation product by an irreversible reaction.

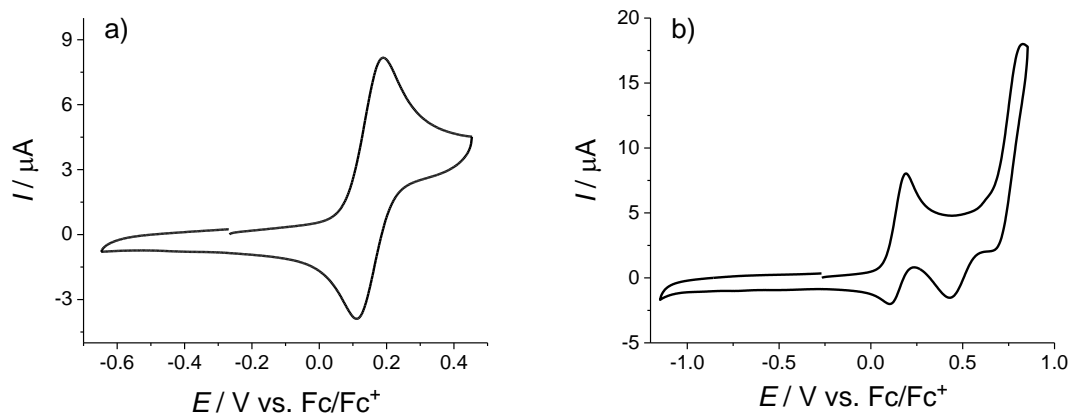


Fig. 34: Cyclic voltammetry of compound **1** (0.3 mM concentration) in DCM and 0.1 M Bu₄NClO₄ as supporting electrolyte, $\nu = 0.1 \text{ Vs}^{-1}$.

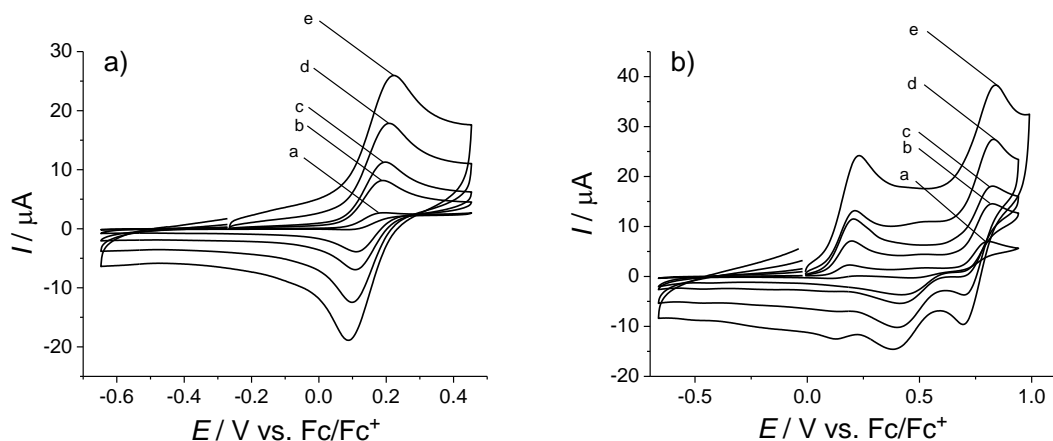


Fig. 35: Scan rate dependence for voltammetric signals for compound **1** (0.3 mM concentration) in DCM and 0.1 M Bu_4NClO_4 as supporting electrolyte, (a) $\nu = 0.01 \text{ Vs}^{-1}$, (b) $\nu = 0.1 \text{ Vs}^{-1}$, (c) $\nu = 0.2 \text{ Vs}^{-1}$, (d) $\nu = 0.5 \text{ Vs}^{-1}$, (e) $\nu = 1 \text{ Vs}^{-1}$.

In compound **2** the redox-active DAT is substituted by two methyl group. There is one oxidation peak ($E_{\text{pa}} = 0.11 \text{ V}$) in the potential range from -0.50 V to 0.30 V and the reduction peaks occurs at $E_{\text{pc}} = 0.03 \text{ V}$, the formal potential is at 0.07 V (Fig. 36a). Only one electron is transferred, i.e. a radical cation is formed and reduced to the initial compound in the negatively going scan. From the parameters in Tab. 6 it is obvious that this is a quasi-reversible reaction. When extending potential range to 1.00 V vs. Fc/Fc^+ , a second one-electron oxidation peak is observed at 0.69 V (Fig. 36b). At the lower scan rates, some side reaction occurs (additional reduction peak at 0.44 V , Fig. 37b), but at scan rate larger than 0.5 V s^{-1} this feature disappears.

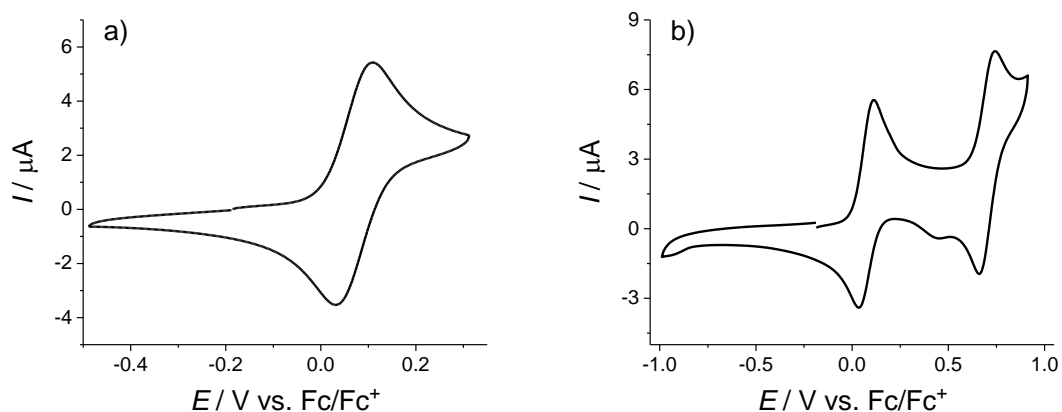


Fig. 36: Cyclic voltammetry of compound **2** (0.3 mM concentration) in DCM and 0.1 M Bu_4NClO_4 as supporting electrolyte, $\nu = 0.1 \text{ Vs}^{-1}$.

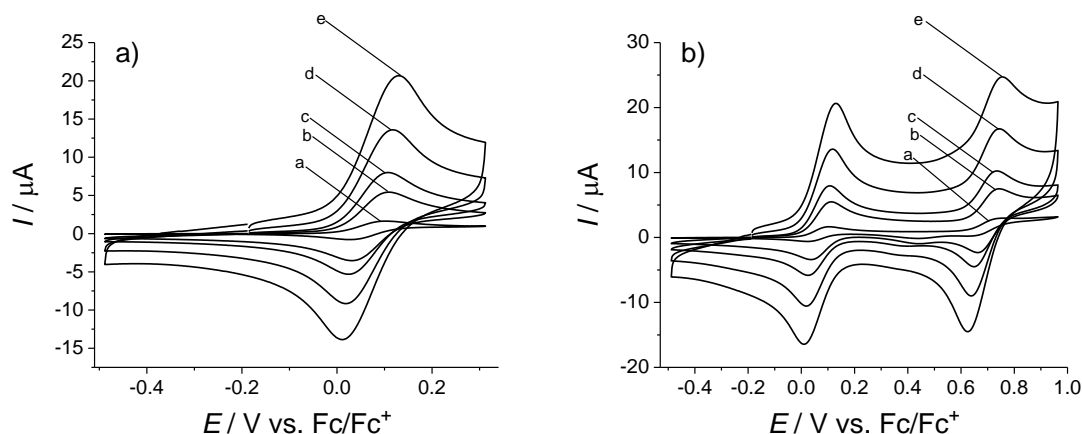


Fig. 37: Scan rate dependence for voltammetric signals for compound **2** (0.3 mM concentration) in DCM and 0.1 M Bu_4NClO_4 as supporting electrolyte (a) $\nu = 0.01 \text{ Vs}^{-1}$, (b) $\nu = 0.1 \text{ Vs}^{-1}$, (c) $\nu = 0.2 \text{ Vs}^{-1}$, (d) $\nu = 0.5 \text{ Vs}^{-1}$, (e) $\nu = 1 \text{ Vs}^{-1}$.

Compound **3** has trifluormethyl benzamide and 3-(aminopropyl)amino as substituents. This molecule shows two oxidation peaks (0.03 V and 0.18 V) and one reduction peak (0.11 V) in the potential range between -0.50 V and 0.40 V (Fig. 38a). When the potential range is extended to 1.10 V vs. Fc/Fc^+ , one more oxidation peak appears at 0.82 V and one narrow reduction peak at 0.63 V (Fig. 38b). At higher scan rates (Fig. 39b, $\nu > 0.2 \text{ Vs}^{-1}$), a second oxidation peak appears at 0.68 V and the narrow reduction peak becomes broader.

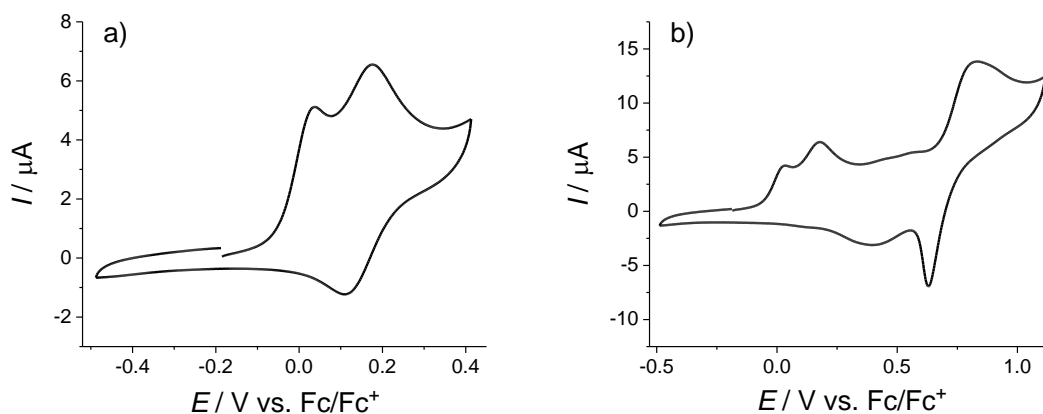


Fig. 38: Cyclic voltammetry of compound **3** (0.3 mM concentration) in DCM and 0.1 M Bu_4NClO_4 as supporting electrolyte, $\nu = 0.1 \text{ Vs}^{-1}$.

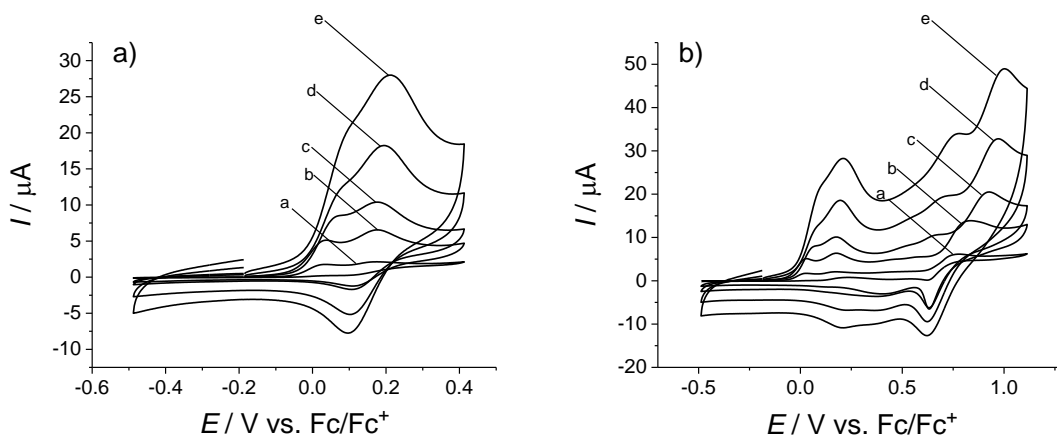


Fig. 39: Scan rate dependence for voltammetric signals for compound **3** (0.3 mM concentration) in DCM and 0.1 M Bu_4NClO_4 as supporting electrolyte, (a) $\nu = 0.01 \text{ Vs}^{-1}$, (b) $\nu = 0.1 \text{ Vs}^{-1}$, (c) $\nu = 0.2 \text{ Vs}^{-1}$, (d) $\nu = 0.5 \text{ Vs}^{-1}$, (e) $\nu = 1 \text{ Vs}^{-1}$.

Compound **4** has trifluoromethyl benzamide and 3-(allyloxycarbonylamino)propylamino as substituents. In the potential range from -0.65 V to 0.40 V, there is a quasi-reversible redox couple with the formal potential of 0.13 V vs. Fc/Fc^+ couple (Fig. 40a). As here amine groups have protection, the radical cation is not chemically consumed at lower scan rates and the ratio $I_{\text{pa}}/I_{\text{pc}}$ does not decrease with decreasing scan rate (Fig. 41a). When the potential range is expanded to 0.90 V, the molecule behaves very similar to compound **1** (Fig. 40b, Fig. 41b). All peaks of compound **4** are shifted by -0.02 V against the corresponding signals of compound **1**.

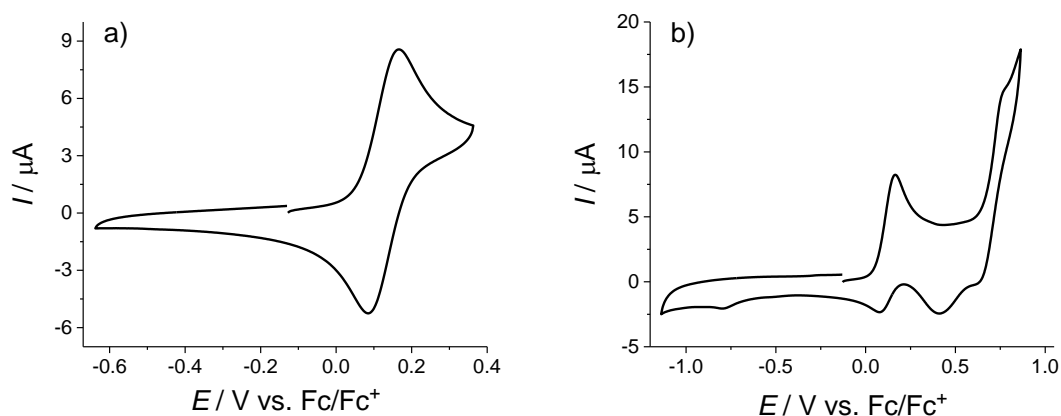


Fig. 40: Cyclic voltammetry of compound **4** (0.3 mM concentration) in DCM and 0.1 M Bu_4NClO_4 as supporting electrolyte, $\nu = 0.1 \text{ Vs}^{-1}$.

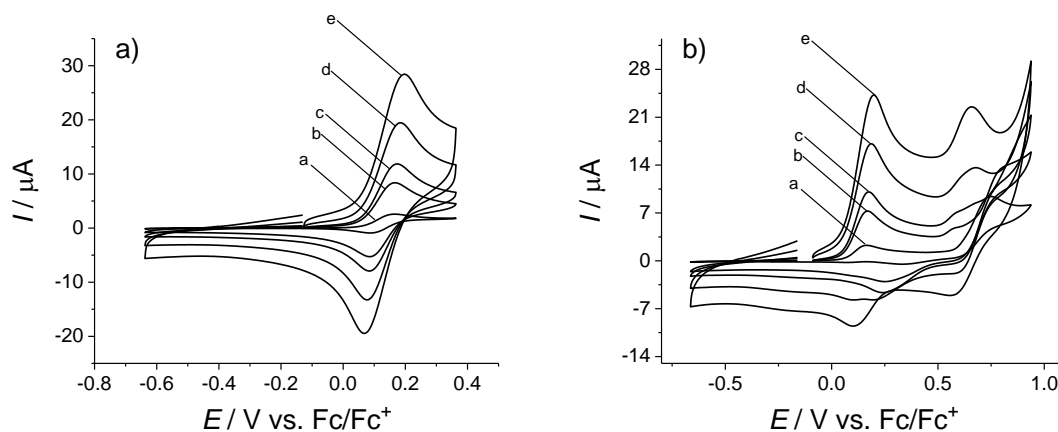


Fig. 41: Scan rate dependence for voltammetric signals for compound **4** (0.3 mM concentration) in DCM and 0.1 M Bu_4NClO_4 as supporting electrolyte, (a) $\nu = 0.01 \text{ Vs}^{-1}$, (b) $\nu = 0.1 \text{ Vs}^{-1}$, (c) $\nu = 0.2 \text{ Vs}^{-1}$, (d) $\nu = 0.5 \text{ Vs}^{-1}$, (e) $\nu = 1 \text{ Vs}^{-1}$.

Compound **5** is with trifluormethyl benzamide and acetyl group as substituent groups. There is one irreversible peak at 0.64 V in the potential range from -1.15 V to 0.76 V (Fig. 42a). When the range is extended to 1.05 V vs. Fc/Fc^+ , a second irreversible peak appears at 0.90 V, and one reduction peak appears at -0.54 V which disappears after one cycle in the potential range from -1.15 V to -0.15 V (Fig. 42b). Upon change the scan rate there is no significant change in features of cycle voltammogram (Fig. 43).

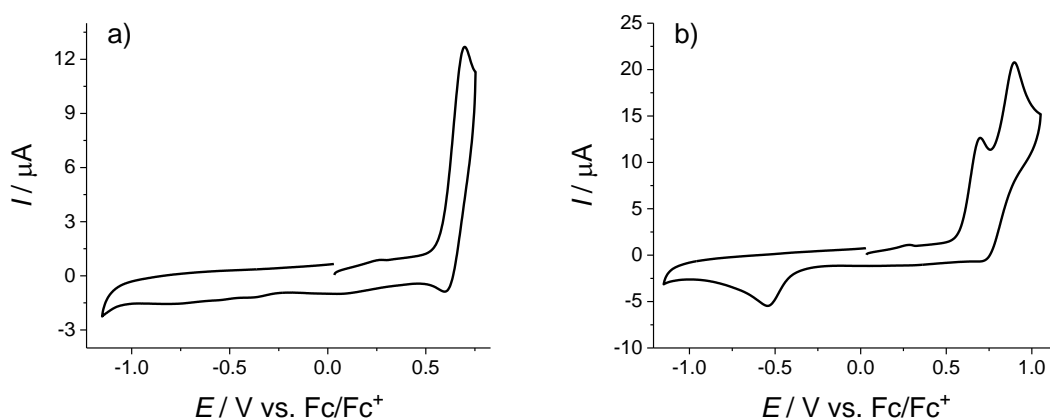


Fig. 42: Cyclic voltammetry of compound **5** (0.3 mM concentration) in DCM and 0.1 M Bu_4NClO_4 as supporting electrolyte, $\nu = 0.1 \text{ Vs}^{-1}$.

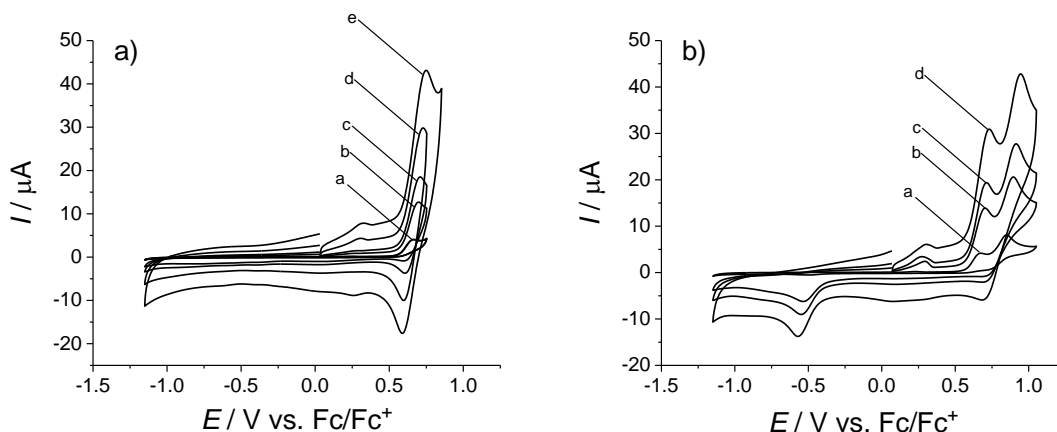


Fig. 43: Scan rate dependence for voltammetric signals for compound **5** (0.3 mM concentration) in DCM and 0.1 M Bu_4NClO_4 as supporting electrolyte, (a) $\nu = 0.01 \text{ Vs}^{-1}$, (b) $\nu = 0.1 \text{ Vs}^{-1}$, (c) $\nu = 0.2 \text{ Vs}^{-1}$, (d) $\nu = 0.5 \text{ Vs}^{-1}$, (e) $\nu = 1 \text{ Vs}^{-1}$.

Compound **6** is structurally related to compound **5**. The trifluoromethyl benzamide group is exchanged with the Boc group. This molecule has no oxidation or reduction peaks in the potential range from -1.00 V to 1.05 V. One can see a slight current increase at around 0.95 V (Fig. 44). This does not allow further conclusion as this potential range overlaps with the onset of solvent oxidation.

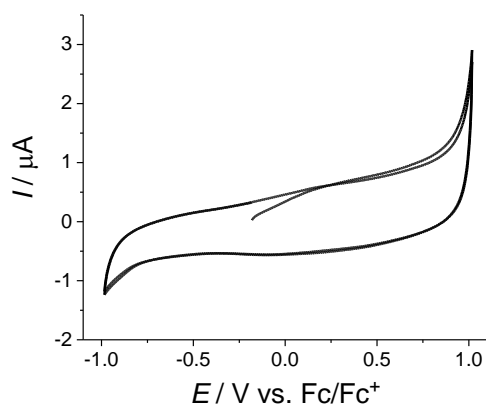


Fig. 44: Cyclic voltammetry of compound **6** (0.3 mM concentration) in DCM and 0.1 M Bu_4NClO_4 as supporting electrolyte, $\nu = 0.1 \text{ Vs}^{-1}$.

Compound **7** has phenyl substituents directly attached to the amino groups of the DAT scaffold. Here, one quasi-reversible pair of peak appears with a formal potential of 0.27 V in the potential range from -0.50 V to 0.50 V (Fig. 45a). When the range is extended to 1.00 V vs. Fc/Fc^+ , the second pair of peak appears at 0.69 V (Fig. 45b). The second peak is also quasi-reversible. With a change of scan rates there is no significant change in cyclic voltammograms (Fig. 46).

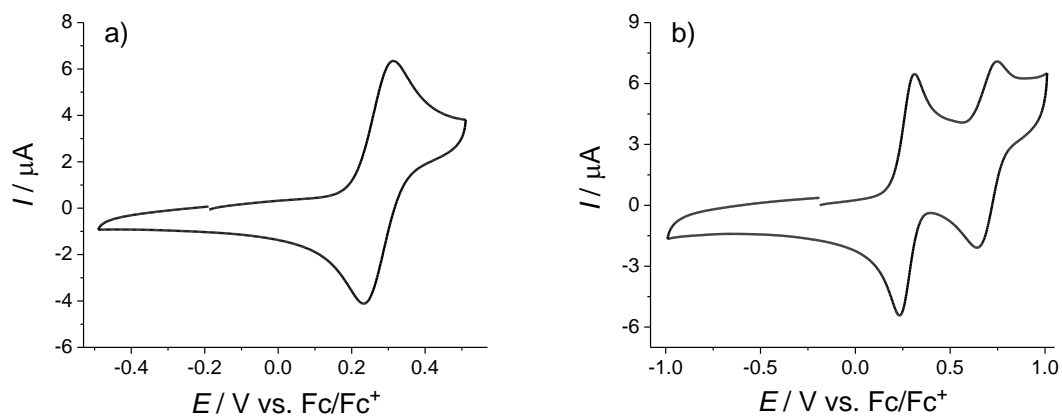


Fig. 45: Cyclic voltammetry of compound **7** (0.3 mM concentration) in DCM and 0.1 M Bu₄NClO₄ as supporting electrolyte, $\nu = 0.1 \text{ Vs}^{-1}$.

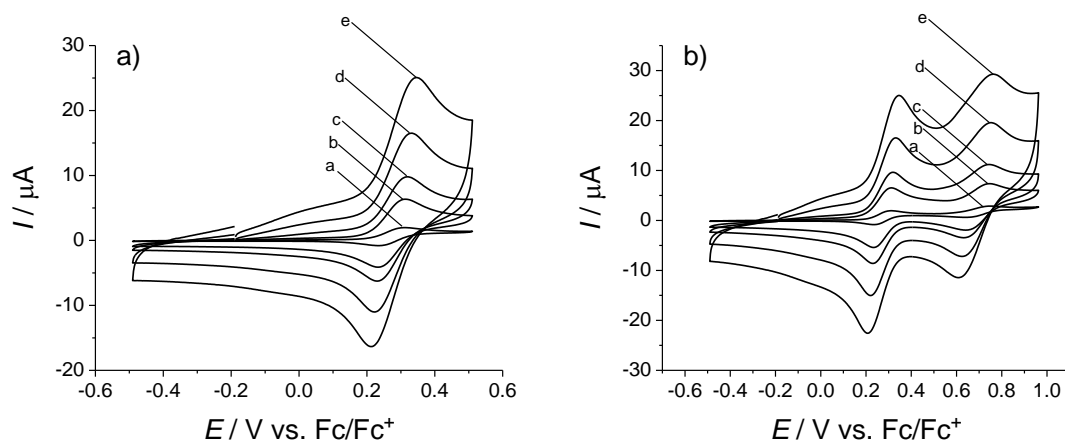


Fig. 46: Scan rate dependence for voltammetric signals for compound **7** (0.3 mM concentration) in DCM and 0.1 M Bu₄NClO₄ as supporting electrolyte, (a) $\nu = 0.01 \text{ Vs}^{-1}$, (b) $\nu = 0.1 \text{ Vs}^{-1}$, (c) $\nu = 0.2 \text{ Vs}^{-1}$, (d) $\nu = 0.5 \text{ Vs}^{-1}$, (e) $\nu = 1 \text{ Vs}^{-1}$.

Tab. 5: Formal potentials, wavelength of emission and absorption maximums and Stokes shifts for the different structures of the DAT molecules.

Compound	E° , 1st_peak /V	E° , 2nd peak /V	$\lambda_{\text{em, max}}$ /nm	$\lambda_{\text{abs, max}}$ /nm	$\lambda_{\text{em, max}} - \lambda_{\text{abs, max}}$ /nm
1	0.15	0.82	581	434	147
2	0.07	0.69	598	478	120
3	0.14	/	583	465	118
4	0.13	0.77	587	467	118
5	0.64	0.90	503	409	94
6	/	/	445	367	78
7	0.27	0.69	589	475	114

Tab. 6: Electrochemical properties of the DAT derivatives.

	$\nu/(\text{Vs}^{-1})$	E_{pa}/V	E_{pc}/V	$E^{\circ'}/\text{V}$	$\Delta E_{\text{p}}/\text{V}$	$I_{\text{pa}}/I_{\text{pc}}$
1 (1 st peak)	0.01	0.19	0.08	0.14	0.11	1.74
	0.1	0.19	0.11	0.15	0.08	1.22
	0.2	0.20	0.11	0.15	0.09	1.02
	0.5	0.21	0.10	0.15	0.11	0.86
	1	0.22	0.09	0.15	0.13	0.77
2 (1 st peak)	0.01	0.10	0.03	0.06	0.07	1.20
	0.1	0.11	0.03	0.07	0.08	1.02
	0.2	0.10	0.03	0.06	0.08	0.99
	0.5	0.12	0.02	0.07	0.10	0.94
	1	0.13	0.01	0.07	0.12	0.88
2 (2 nd peak)	0.01	0.76	0.63	0.70	0.13	1.47
	0.1	0.74	0.66	0.70	0.08	1.00
	0.2	0.74	0.64	0.69	0.09	0.89
	0.5	0.74	0.63	0.69	0.11	0.73
	1	0.75	0.62	0.69	0.13	0.64
3 (1 st peak)	0.01	0.17	0.10	0.13	0.08	/
	0.1	0.18	0.11	0.14	0.06	/
	0.2	0.17	0.11	0.14	0.06	/
	0.5	0.19	0.10	0.15	0.09	/
	1	0.21	0.10	0.15	0.11	/
4 (1 st peak)	0.01	0.16	0.09	0.12	0.08	1.28
	0.1	0.17	0.08	0.12	0.08	1.01
	0.2	0.17	0.08	0.13	0.09	0.94
	0.5	0.18	0.07	0.13	0.11	0.95
	1	0.20	0.07	0.13	0.12	0.84
7 (1 st peak)	0.01	0.31	0.24	0.27	0.08	1.19
	0.1	0.31	0.24	0.27	0.08	0.94
	0.2	0.32	0.23	0.28	0.09	0.89
	0.5	0.33	0.22	0.28	0.11	0.81
	1	0.34	0.21	0.28	0.13	0.76
7 (2 nd peak)	0.01	0.75	0.64	0.70	0.11	1.09
	0.1	0.74	0.64	0.69	0.10	1.05
	0.2	0.74	0.657	0.69	0.11	0.92
	0.5	0.75	0.62	0.69	0.13	0.84
	1	0.76	0.61	0.69	0.15	0.68

6.2 Fluorescence and UV-vis spectroscopy of DATs

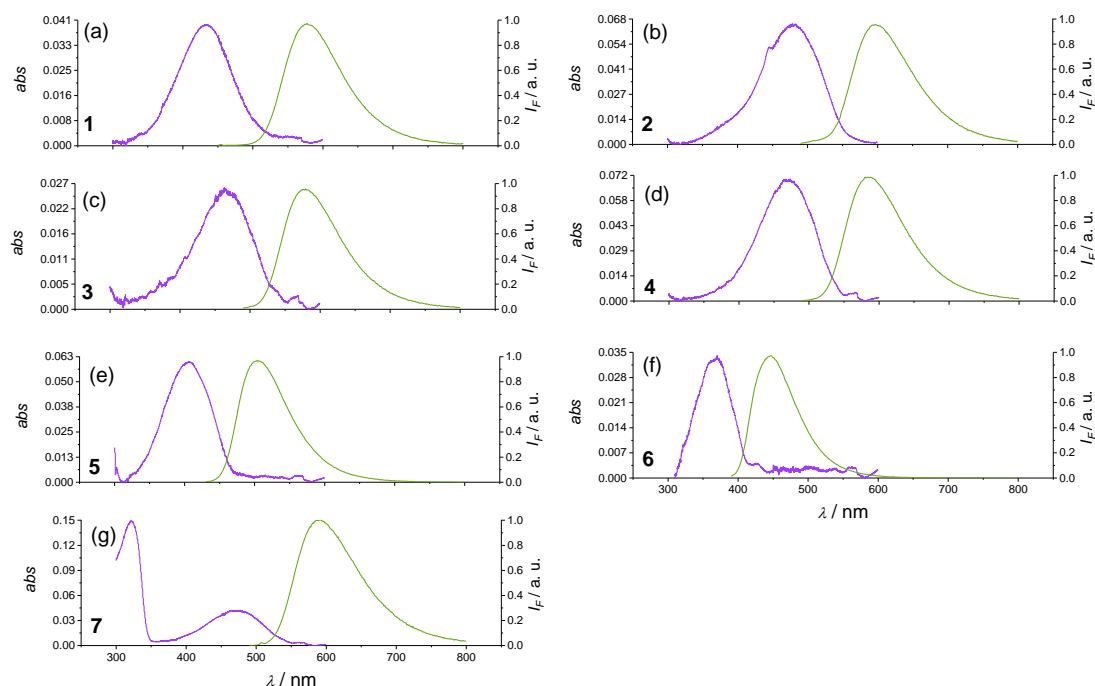


Fig. 47: Absorption (in purple) and emission spectra (in green) of 9 μM DAT derivatives in ethanol; a) compound **1**, b) compound **2**, c) compound **3**, d) compound **4**, e) compound **5**, f) compound **6** and g) compound **7**.

Absorption and emission spectra are shown in Fig. 47. As these compounds have typical push-pull aromatic system, the absorption and emission wavelengths are sensitive to the nature of substituent group. The shifts in absorption and emission wavelengths and change in Stokes shifts are shown in Tab. 5. Compound **1** carries two NH_2 groups and shows absorption and emission at 434 nm and 581 nm (Stokes shift of 147 nm). This compound has the largest Stokes shift from all seven investigated compounds. Compound **2** has two electron-donating groups and the Stokes shift is lower (120 nm). Because of electron-donating groups absorption and emission wavelengths are red-shifted to 478 nm and 598 nm. Compounds **3** and **4** have similar electron-donating substituents so their Stokes shift is the same (118 nm) although their absorption and emission wavelengths differ a bit (for compound **3** 465 nm and 583 nm, compound **4** 467 nm and 587 nm). Compound **5** has one electron donating and one electron-accepting group, the Stokes shift is significantly lower (94 nm). Absorption and emission wavelengths are blue-shifted to 409 nm and 503 nm. Compound **6** has two electron-accepting groups, absorption and emission are even more blue-shifted than in compound **5** to 367 nm and 445 nm (Stokes shift 87 nm). Compound **7** has again two electron-donating groups and absorption and

emission are in the same range as for compounds **3** and **4** at 475 nm and 589 nm. Stokes shift is 114 nm, which is probably due to the influence of the side groups attached to ring.

Fig. 48 shows a plot of the wavelength of emission maximum for compounds **1**, **2**, **3**, **4**, **5** and **7** versus the formal potential of the first oxidation. Except for compound **7**, the DAT derivatives exhibit a quite strict correlation between those quantities despite the fact that the electrochemical data had to be obtained in DCM for solubility reasons and the emission spectra were recorded in ethanol. Compound **7** is an exception because its phenyl substituent is directly attached to aromatic amine while all other aromatic substituents are separated by an aliphatic methylene group from the aromatic amine. The phenyl group in compound **7** stabilizes the nonbonding orbital of nitrogen. Because of this, the formal potential of compound **7** is significantly higher than those of others. Emission wavelength are not so strongly different. From this data one can conclude that by measuring fluorescence one can predict potentials of the first oxidation. However, all compounds that are plotted in Fig. 48 have at least one amine group. As one can see from the structure, compound **6** has two amide groups, which are weaker donors (compared to amines). Therefore, the electronic delocalization is weakened causing a hypsochromic effect (Fig. 47). Because of this, the formal potential of the first oxidation for compound **6** cannot be determined in Fig. 48.

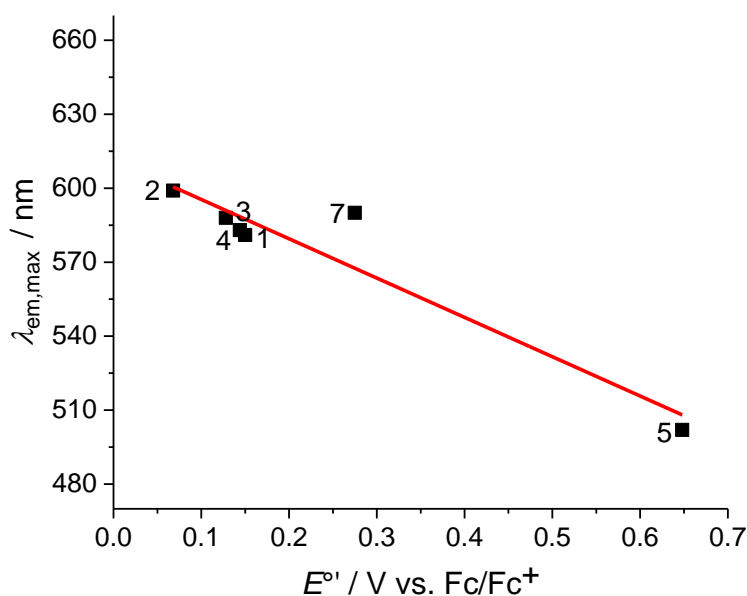


Fig. 48 Correlation between the formal potential and the wavelength of the emission maximum for compound **1**, **2**, **3**, **4**, **5** and **7**.

The correlation between the wavelength of absorption maximum and the redox potentials of first oxidation for compound **1**, **2**, **3**, **4**, **5** and **7** is shown in Fig. 49. Compared to the correlation in Fig. 48, there are two exceptions, compound **1** and **7**. Compound **7** has been discussed as exception already in connection to Fig. 48. As compound **1** is carrying two NH₂ groups, the Stokes shift has a significantly larger value compared to the other compounds (with substituent groups). As a consequence, the wavelength of the absorption maximum of compound **1** is significantly blue-shifted compared to all other investigated compounds.

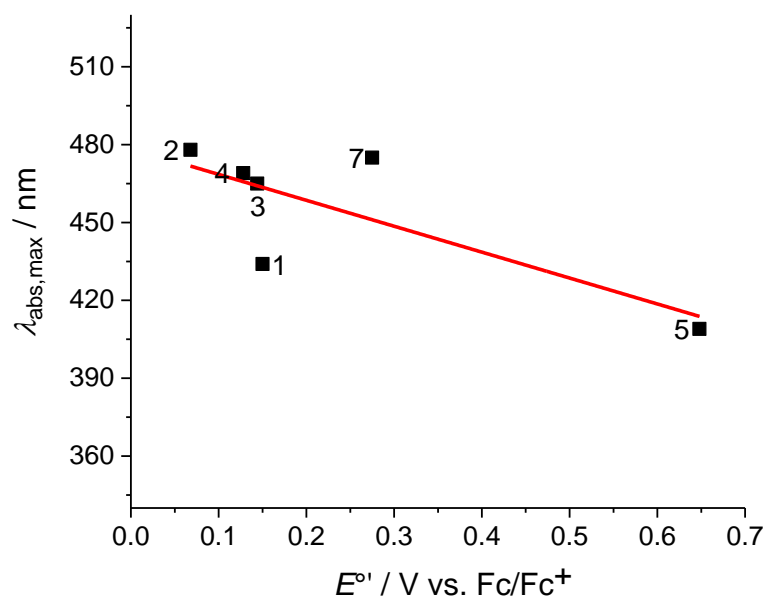


Fig. 49 Correlation between the formal potential and the wavelength of the absorption maximum for compound **1**, **2**, **3**, **4**, **5** and **7**.

first cycle (green line in Fig. 51) one can see that these layers have no redox activity until 1.04 V vs. SHE, where a large irreversible oxidation peak appears (marked III_a in Fig. 51). In the second potential cycle the current has significantly decreased and is absent in the third cycle totally. This peak is typical for electrochemical reaction of immobilized redox systems (described in Chapter 3.2). Here molecules of compound **8** are electrochemically oxidized which is followed by nucleophilic attack by H₂O. The proposed reaction mechanism is shown on Scheme 1. After electrochemical activation a reversible peak appears with a formal potential of 0.66 V in second cycle (blue line). I_a marks the anodic peak and I_c marks the cathodic one in Fig. 51. An irreversible peak also appears at 0.87 V (II_a in Fig. 51), which is quite surprising. In the third cycle (red line) the behaviour of those two peaks changes differently, the current for reversible system increases (I_a and I_c), while the current for the irreversible system decreases (II_a), which disappears in further cycles. After the third cycle, the behaviour of the reversible peak (I_a and I_c) at 0.66 V is stable, which can be seen from cyclic voltammogram in Fig. 52 in the potential range from 0.45 V to 0.85 V

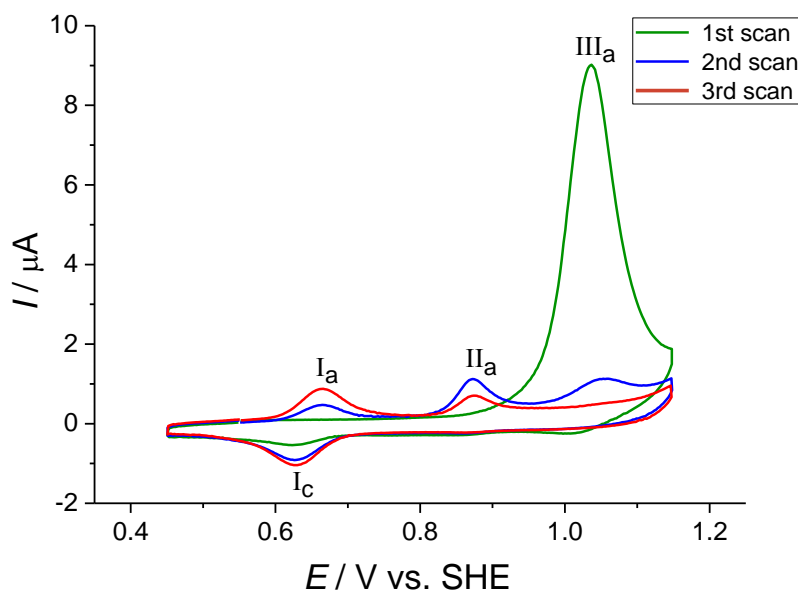


Fig. 51: Cyclic voltammogram of SAMs composed of compound **8** and 1-decanethiol on gold substrate in 0.1 M HClO₄ in range from 0.45 V to 1.15 V, $\nu=0.05$ V s⁻¹.

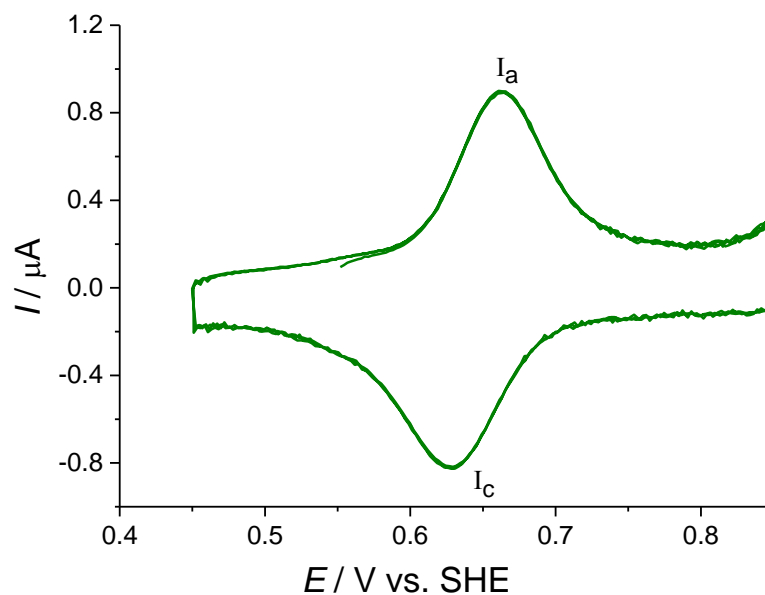
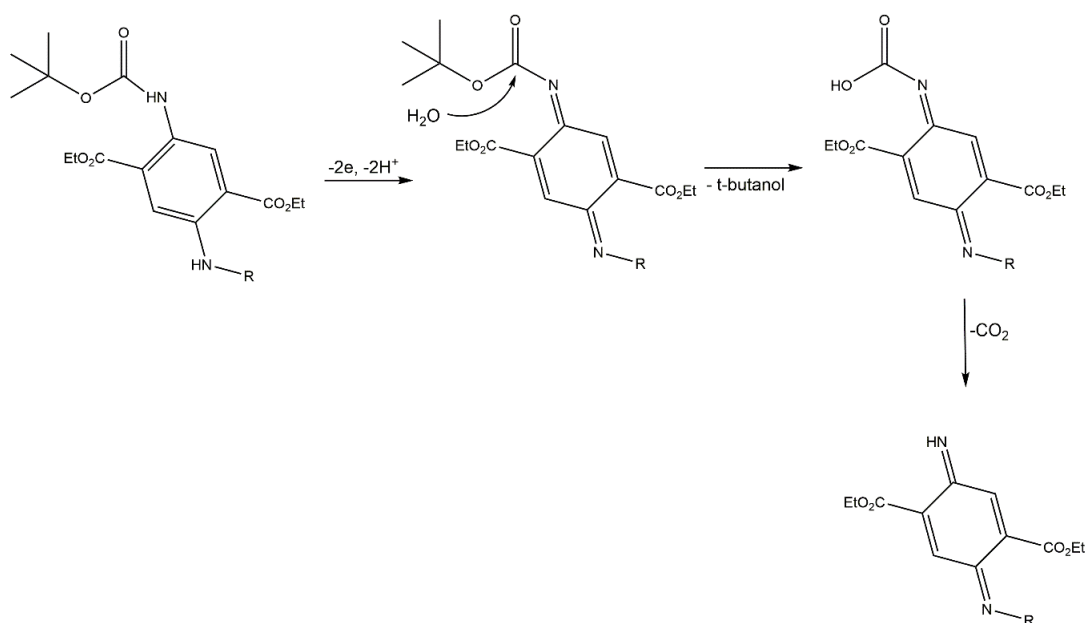


Fig. 52: Cyclic voltammogram of SAMs composed of compound **8** and 1-decanethiol on gold substrate in 0.1 M HClO₄ after electrochemical activation of SAMs in range from 0.45 V to 0.85 V, $\nu = 0.05 \text{ Vs}^{-1}$.



Scheme 1: The reaction mechanism of the electrochemical activation of the compound **8**.

The area under activation peak at 1.04 V (III_a in Fig. 51) and the area under the reversible peak (I_a in Fig. 52) were integrated in order to determine the charge, Q . The number of electrons transferred in the electrochemical reaction, n , was estimated to be 2 using equation (17). The interfacial concentration of species that is activated and redox-active was calculated with equation (16):

$$\Gamma = \frac{Q}{nFA} = \frac{9.65 \times 10^{-6} \text{C}}{2 \cdot 28.26 \text{mm}^2 \cdot 96485.32 \text{Cmol}^{-1}} = 1.77 \times 10^{-12} \frac{\text{mol}}{\text{mm}^2} \quad (29)$$

$$\Gamma = 1.77 \times 10^{-10} \frac{\text{mol}}{\text{cm}^2}$$

$$\Gamma = \frac{Q}{nFA} = \frac{9.20 \times 10^{-8} \text{C}}{2 \cdot 28.26 \text{mm}^2 \cdot 96485.32 \text{Cmol}^{-1}} = 1.69 \times 10^{-13} \frac{\text{mol}}{\text{mm}^2} \quad (30)$$

$$\Gamma = 1.69 \times 10^{-11} \frac{\text{mol}}{\text{cm}^2}$$

The interfacial concentration Γ of species that are activated (III_a, Fig. 51) is calculated in equation (29) and the ones that are redox-active (I_a, Fig. 52) in equation (30). Literature value of interfacial concentration of SAMs with lipoic acid is $7.1 \cdot 10^{-10} \text{ mol cm}^{-2}$ [145] which is in good agreement with interfacial concentration calculated from electrochemical activation in equation (29). By comparing the interfacial concentrations in eq. (29) and (30), it was determined that only 10% of molecules that are activated form the reversible redox couple in Fig. 52.

Laviron's theory (plot of E_p versus $\log v$ in Fig. 53) was used for determining k_{ET} as described in Chapter 3.2.1. The average value of electron transfer coefficient, α is estimated to be 0.36. Under these conditions the average kinetic parameter k_{ET} was obtained as 16.17 s^{-1} when calculated from the cathodic potentials and 35.14 s^{-1} when calculated from the anodic potentials.

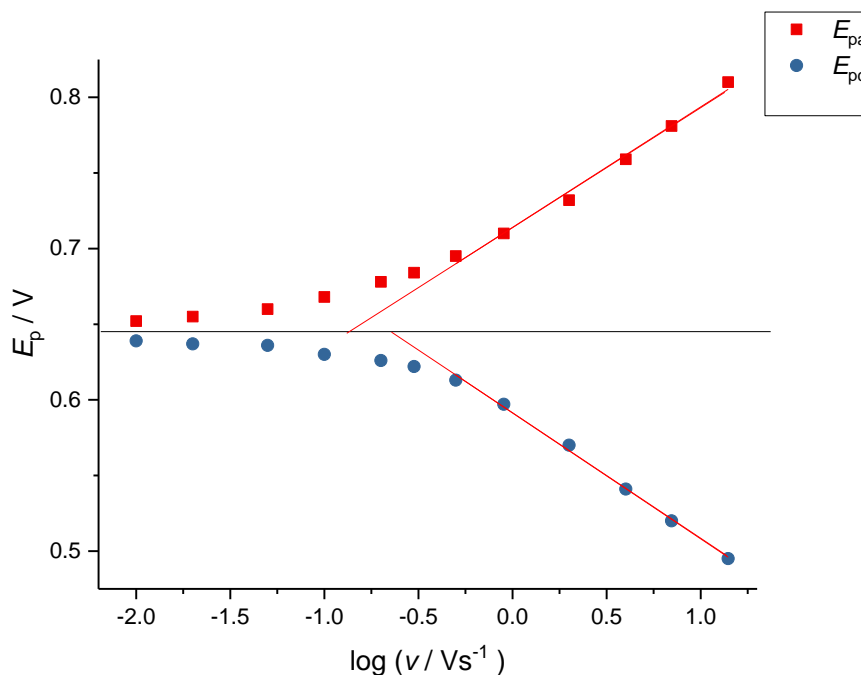


Fig. 53: Plot of peak potential (E_p) of peak I_a and I_c vs $\ln(v)$ for electron transfer in cyclic voltammogram in Fig. 52.

Because the results of electrochemical activation in perchloric acid are quite interesting and unexpected, we wanted to see whether the monolayers show a similar behaviour in other solvents. Electrochemical activation was also tried in sulphuric acid. Cyclic voltammogram in Fig. 54 shows the behaviour of the backfilled surfaces of compound **8** in 0.1 M sulphuric acid. An irreversible oxidation peak at 1.1 V can be observed in the potential range from -0.35 V to 1.15 V vs. SHE (marked II_a in Fig. 54) in the first cycle of backfilled SAMs of compound **8** in 0.1 M sulphuric acid. The position of this peak is shifted by 0.06 V compared to electrochemical activation in perchloric acid. However, no significant peaks can be seen in cyclic voltammogram after activation. This means that activation of this self-assembled system with the appearance of a reversible redox couple is exclusive for perchloric acid.

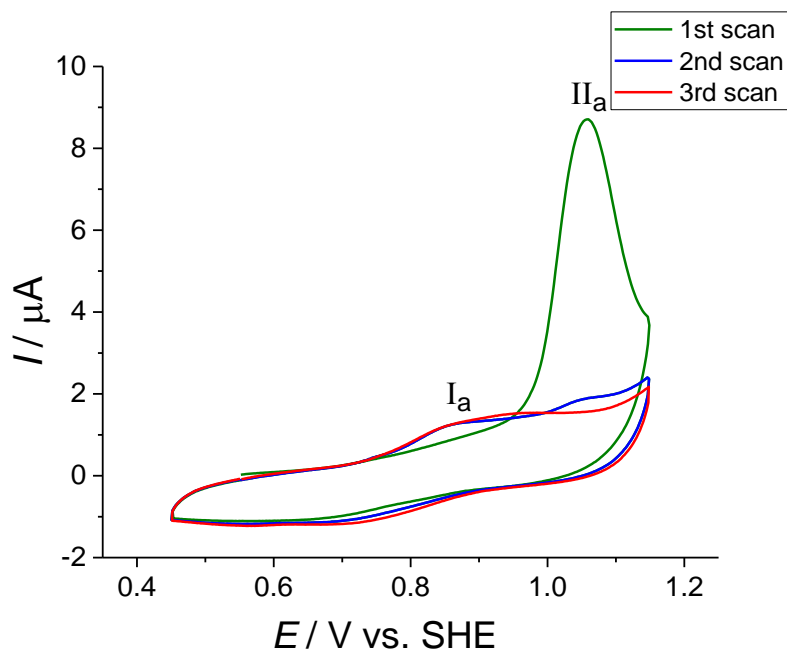


Fig. 54: Cyclic voltammogram of SAMs composed of compound **8** and 1-decanethiol on gold substrate in 0.1 M H_2SO_4 in range from 0.45 V to 1.15 V, $\nu=0.05 \text{ V s}^{-1}$.

Electrochemical activation was also tried for compound **9** which has a shorter chain. In Fig. 55 is shown a cyclic voltammogram of this system in perchloric acid. As compound **9** has two electron-withdrawing groups connected to the ring (urethane and amide) it was not possible to activate this SAM in the potential window in which SAMs are stable on gold in perchloric acid. The current increase at 1.4 V in Fig. 55 is probably due to oxidation of the gold [146].

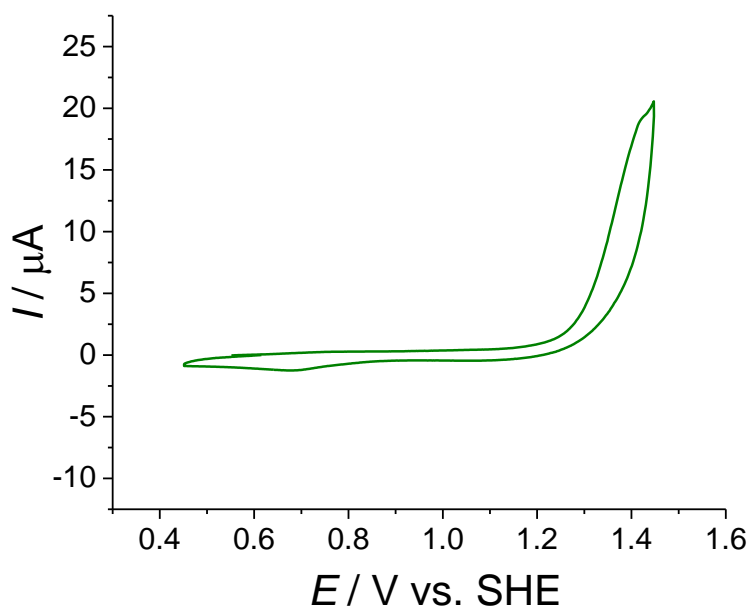


Fig. 55: Cyclic voltammogram of SAMs composed of compound **9** and 1-hexanethiol on gold substrate in 0.1 M HClO_4 in range from 0.45 V to 1.50 V, $\nu = 0.05 \text{ V s}^{-1}$.

As the behaviour of SAMs that contain compound **8** and 1-decanethiol in perchloric acid is quite unusual, further spectroscopic characterization of these surfaces were initiated.

7.2 Surface spectroscopic characterization

After preparation, surfaces were characterized with XPS and PM IRRAS. The basics of both techniques are summarised in Chapter 3.3 and Chapter 3.4, respectively.

XPS was used for determination of the chemical information from the molecular monolayers. The peak-fit analysis was performed by using the sum of Gaussian and Lorentzian contributions and smart background from Avantage software. The convolution combination of Gaussian and Lorentzian contributions may give an improved peak fit in some cases, but it involves more calculations and is slightly slower. In this case it was not necessary. In Fig. 56 are shown the results of the peak fit analysis obtained for the C 1s, O 1s, N 1s and S 2p spectrum of a molecular monolayer composed of compound **8** and 1-decanthiol. The assignment of the peaks and binding energies is summarized in Tab. 7. The C 1s spectrum is composed of two main peaks, one at 284.6 eV (marked 1) and one at 285.4 eV (marked 2). The first peak at 284.6 eV (marked 1) corresponds to the carbon atoms of the alkyl chains, the aromatic ring and the carbon bound to the sulphur atoms. In contrast the peak at 285.4 eV (marked 2) corresponds to the carbon atoms with a higher binding energy due to the bond to one more electronegative atom (C–O and C–N) [147]. This higher binding energy comes from the higher electronegativity of the oxygen and nitrogen atom compared to sulphur, carbon and hydrogen atoms. Fig. 56, also shows the presence of four small peaks lying at binding energies of 286.8 eV (marked 3), 287.9 eV (marked 4), 289.1 eV (marked 5) and 290.7 eV (marked 6). The first of those peaks (marked 3) corresponds to carbon in amide and ester group which have two electronegative atoms bound to carbon (O=C–O and O=C–N) which shifts binding energies to even higher values. The peak at 287.9 eV (marked 4) corresponds to carbon bound to three electronegative atoms in the urethane group. The peaks at 289.1 eV (marked 5) is attributed to contamination of the sample during preparation of compound or contamination of the surfaces during handling in the laboratory. Multi-electron

excitation, i.e. to shake-up is assigned to peak at 290.7 eV [148] (marked 6). Because of the contamination, the C 1s peak will not be discussed further in the thesis. The O 1s spectrum of surfaces with compound **8** is composed of two main peaks at 531.7 eV (marked 1) and 533.3 eV (marked 2). These peaks are attributed to the oxygen atoms involved in the O=C and O-C bonds, respectively [149]. Moreover, binding energy of 533.00 - 533.50 eV corresponds to binding energy of oxygen in adsorbed water molecules at surface [150]. This means peak at 533.3 eV (marked 2) which corresponds to oxygen in O-C group, can also be attributed to adsorbed water. As there is high probability of adsorbed water molecules on these surfaces, the oxygen peak cannot be taken for further evaluation of the surfaces. Although, S 2p spectra was recorded first there is still radiation damage doublet at 163.3 eV [151]. The main doublet is at 161.8 eV corresponds to sulphur gold bond [127]. There is only one N 1s component at 399.6 eV which corresponds to all nitrogen atoms in SAMs [152]. Atomic ratios of the SAM surface normalized to sulphur are C: O: N: S = 16.5: 4.2: 1.7: 1. The ratios of the same elements in the molecule are C: O: N: S = 14: 3.5: 1.5: 1, which is in good agreement with the ratio on the surface. The higher amount of carbon on the surface can be explained by the presence of diluent and contamination on the surface. Also, the higher content of oxygen can be explained by adsorbed water molecules on the surface. The amount of the diluent on the surface is insignificant. This is proved by the fact that the ratio of nitrogen compared to sulphur is almost identical in the compound and on the surface.

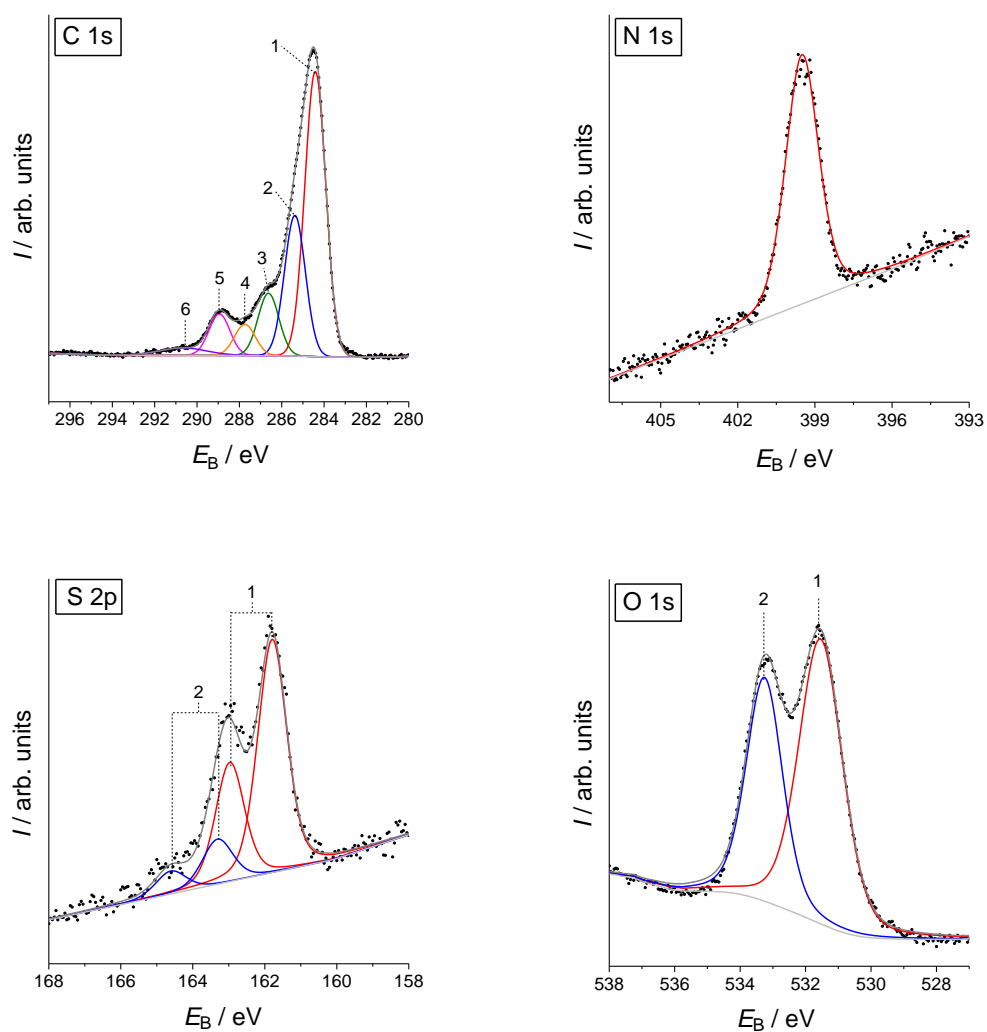


Fig. 56: XP spectra of SAMs with 1-decanethiol and compound **8** on gold substrate in the C 1s, N 1s, O 1s and S 2p region. The experimental data points are plotted as dots, the envelope as a dark grey line, single components as red, blue, orange, green, purple and pink lines and the background a light grey line.

Tab. 7 Assignment of fitted XPS spectra from Fig. 56

Signal	Interpretation	E_B / eV	FWHM / eV	Reference
S 2p _{3/2}	R-S-Au	161.8	1.00	[127]
S 2p _{1/2}	R-S-Au	162.9	1.00	[127]
S 2p _{3/2}	radiation damage	163.3	1.00	[151]
S 2p _{1/2}	radiation damage	164.4	1.00	[151]
C 1s	C-C, C-S	284.6	1.21	[147]
C 1s	C-N, C-O	285.4	1.27	[147]
C 1s	ester and amide	286.8	1.53	[147]
C 1s	urethane	287.9	1.21	[147]
C 1s	contamination	289.1	1.53	/
C 1s	shake-up	290.7	2.62	[148]
O 1s	O=C	531.7	1.53	[149]
O 1s	O-C, H ₂ O	533.3	1.53	[149]
N 1s	R-N-H	399.6	1.63	[152]

The infrared-reflectance spectra in the region (1800 cm⁻¹ to 900 cm⁻¹) of the SAMs which contain compound **8** is shown in Fig. 57. The peak assignment is shown in Tab. 8, which was done according to literature [153, 154]. The first two bands at 1727 cm⁻¹ and 1688 cm⁻¹ are the most interesting for these SAMs. They originate from C=O stretching modes. The mode at 1727 cm⁻¹ (marked 1 in Fig. 57) comes from C=O stretching modes in ester groups and the one at 1688 cm⁻¹ (marked 2) corresponds to stretching modes of the urethane and the amide group in compound **8**. In plane CC stretching vibrations from the ring are located at 1544 cm⁻¹ (marked 3), 1421 cm⁻¹ (marked 4) and 1393 cm⁻¹ (marked 5). The band at 1368 cm⁻¹ (marked 6) correspond to CH₃ bending modes and C-O stretching modes in urethane group. The signal at 1266 cm⁻¹ (marked 7) is assigned to overlapping C-N stretching modes, C-O asymmetric stretching modes CC ring stretching modes and CH₂ twisting modes. Also, C-N stretching modes are located at 1243 cm⁻¹ (marked 9) which overlap with C-C stretching modes. C-O asymmetric stretching modes are located at 1224 cm⁻¹ and overlap with CC ring stretching mode. Vibration at 1175 cm⁻¹ (marked 10) with shoulder at 1158 cm⁻¹ corresponds to out of plane CC ring stretching modes. Two bands at 1130 cm⁻¹ (marked

11) and 1109 cm^{-1} (marked 12) are C-O symmetric stretching modes in the Boc group and ester groups. Due to the overlap of bands in this region and the complicated structure of compound **8**, this assignment is tentative.

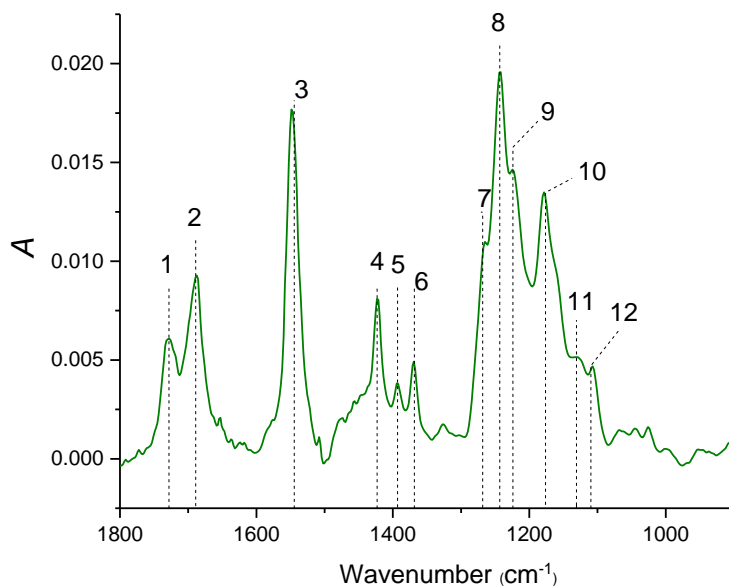


Fig. 57: PM IRRAS spectra of SAMs with compound **8** and 1-decanethiol on gold substrate in region from 1800 cm^{-1} to 900 cm^{-1} .

Tab. 8: Assignment of bands from Fig. 57

Number	Wavenumber / cm^{-1}	Assignment	Reference
1	1727	(C=O) stretch ester	[153, 154]
2	1688	(C=O) stretch amide and urethane	[153, 154]
3	1544	in plane (CC) ring stretch	[153, 154]
4	1421	in plane (CC) ring stretch	[153, 154]
5	1393	in plane (CC) ring stretch	[153, 154]
6	1368	(CH ₃) bending + (C-O) stretch urethane	[153, 154]
7	1266	(C-N) stretch+ (C-O) asym stretch+ (CC) ring stretch + (CH ₂) twisting	[153, 154]
8	1243	(C-N) stretch + (C-C) stretch	[153, 154]
9	1224	(C-O) asym stretch + (CC) ring stretch	[153, 154]
10	1175 + 1158 (sh.)	out of plane (CC) ring stretch	[153, 154]
11	1130	(C-O) sym stretch	[153, 154]
12	1109	(C-O) sym stretch	[153, 154]

The C–H stretching region of the same surface is shown in Fig. 58 with the peak assignments shown in Tab. 9. The degree of crystallinity and packing density of molecules in the SAM can be interpreted through PM IRRAS spectra in this region [155, 156]. The CH₃ stretching modes from 1-decane thiol (marked 3) can be distinguished from the CH₃ stretching modes in Boc group (marked 2). The asymmetric stretching modes at 2983 cm^{-1} originate from the Boc group in compound **8** and the mode at 2972 cm^{-1} are from 1-decanthiol. Asymmetric CH₂ vibrations are at 2927 cm^{-1} (marked 4) and symmetric ones at 2854 cm^{-1} (marked 6). This value is the indication of a less crystalline, more liquid-like packing of the SAM [157, 158]. Well-packed crystalline SAMs have an asymmetric CH₂ stretching band located at around 2919 cm^{-1} [159]. Symmetric CH₃ stretching mode in Boc group is usually very weak and cannot be

assigned due to overlap with CH₂ asymmetric stretching modes and CH₃ symmetric stretching modes [160, 161].

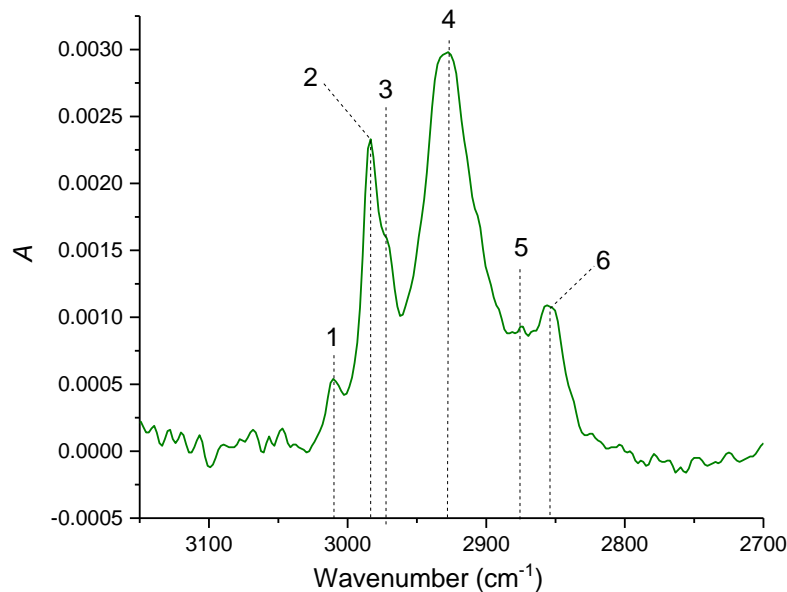


Fig. 58 PM IRRAS spectra of SAMs with compound **8** and 1-decanethiol on gold substrate in region from 3150 cm⁻¹ to 2700 cm⁻¹.

Tab. 9 Assignment of bands from Fig. 58

Number	Wavenumber / cm ⁻¹	Assignment	Reference
1	3010	(CH) _{ar.} stretch	[162]
2	2983	(CH ₃) _{Boc} asym stretch	[163]
3	2972	(CH ₃) asym stretch	[155]
4	2927	(CH ₂) asym stretch	[155]
5	2876	(CH ₃) sym stretch	[155]
6	2854	(CH ₂) sym stretch	[155]

After characterization of freshly prepared SAMs, spectroscopic measurements were performed for SAMs that were only immersed in perchloric acid for 15 min without any kind of electrochemical treatment. Spectroscopic characterization of this surface was done in order to determine whether exposure to perchloric acid without applied potential modified the structure of molecules on the surface. XP spectra of N 1s and S 2p are shown in Fig. 59 with assignment of fitted peaks in Tab. 10. In these spectra one can see no

change compared to spectra of unmodified surfaces (Fig. 56). Ratio of nitrogen compared to sulphur, also did not change and is: N: S = 1.7: 1.

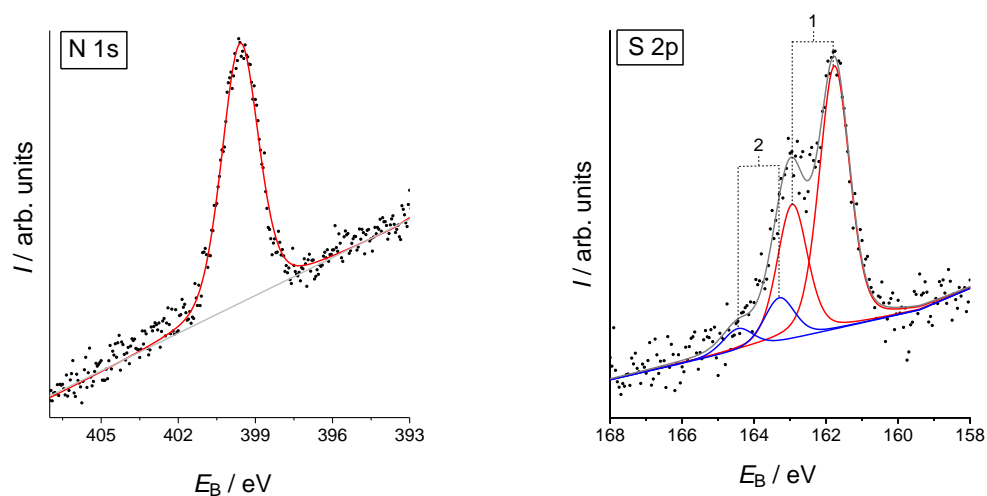


Fig. 59: XP spectra of SAMs with 1-decanethiol and compound **8** on gold substrate in the N 1s and S 2p region after immersion in 0.1 M HClO₄ for 15 min. The experimental data points are plotted as dots, the envelope as a dark grey line, single components as red and blue lines and the background a light grey line.

Tab. 10 Assignment of fitted XPS spectra from Fig. 59

Signal	Interpretation	E_B / eV	FWHM / eV	Reference
S 2p _{3/2}	R-S-Au	161.70	1.00	[127]
S 2p _{1/2}	R-S-Au	162.84	1.00	[127]
S 2p _{3/2}	radiation damage	163.30	1.00	[151]
S 2p _{1/2}	radiation damage	164.45	1.00	[151]
N 1s	R-N-H	399.60	1.62	[152]

PM IRRAS spectra of samples that were only immersion in perchloric acid for 15 min are shown in Fig. 60 (1800 – 900 cm⁻¹ region) and in Fig. 61 (CH stretching region) with assignment in Tab. 11 and Tab. 12, respectively. Compared to the spectra in Fig. 57 and Fig. 58 one cannot see any significant change.

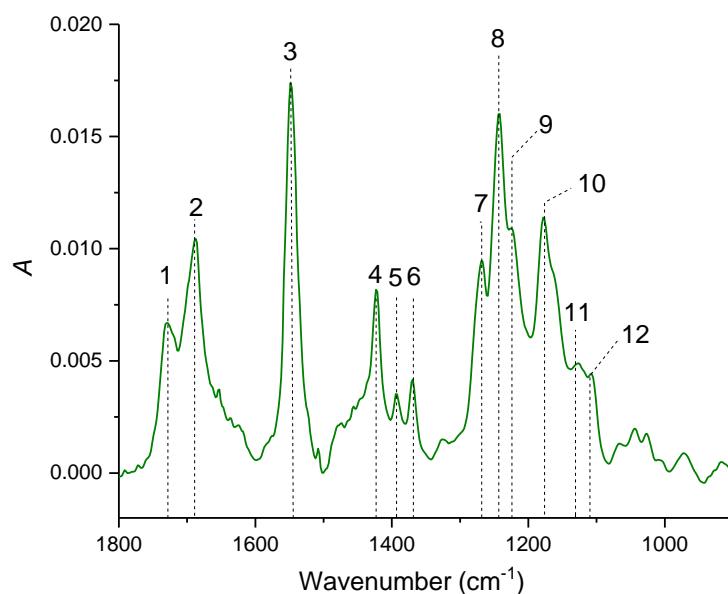


Fig. 60: PM IRRAS spectra of SAMs with compound **8** and 1-decanethiol on gold substrate after immersion in perchloric acid in region from 1800 cm^{-1} to 900 cm^{-1} .

Tab. 11: Assignment of spectra from Fig. 60

Number	Wavenumber / cm^{-1}	Assignment	Reference
1	1727	(C=O) stretch ester	[153, 154]
2	1689	(C=O) stretch amide and urethane	[153, 154]
3	1546	in plane (CC) ring stretch	[153, 154]
4	1423	in plane (CC) ring stretch	[153, 154]
5	1393	in plane (CC) ring stretch	[153, 154]
6	1369	(CH ₃) bending + (C-O) stretch urethane	[153, 154]
7	1268	(C-N) stretch+ (C-O) asym stretch+ (CC) ring stretch + (CH ₂) twisting	[153, 154]
8	1244	(C-N) stretch + (C-C) stretch	[153, 154]
9	1225	(C-O) asym stretch + (CC) ring stretch	[153, 154]
10	1176 + 1161 (sh.)	out of plane (CC) ring stretch	[153, 154]
11	1132	(C-O) sym stretch	[153, 154]
12	1110	(C-O) sym stretch	[153, 154]

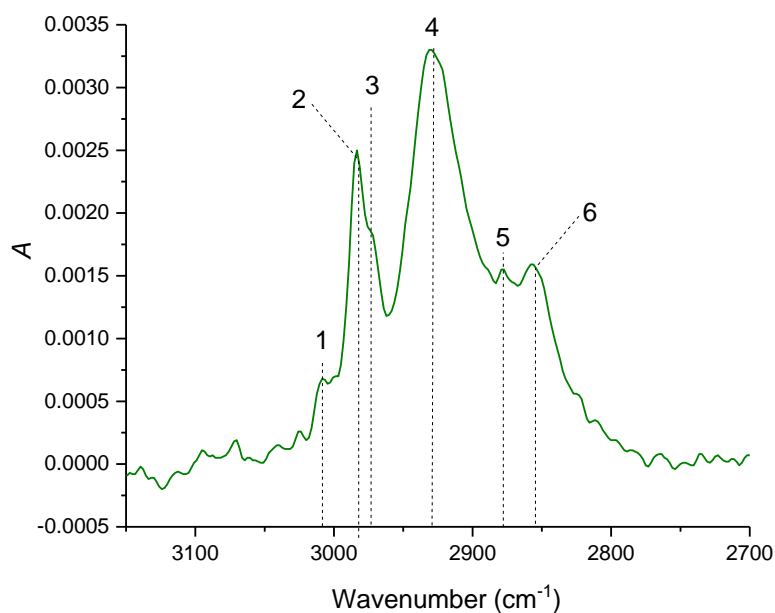


Fig. 61: PM IRRAS spectra of SAMs with compound **8** and 1-decanethiol on gold substrate after immersion in region from 3150 cm^{-1} to 2700 cm^{-1} .

Tab. 12: Assignment of bands from Fig. 61

Number	Wavenumber / cm^{-1}	Assignment	Reference
1	3090	$(\text{CH})_{\text{ar}}$ stretch	[162]
2	2982	$(\text{CH}_3)_{\text{Boc}}$ asym stretch	[163]
3	2973	(CH_3) asym stretch	[155]
4	2928	(CH_2) asym stretch	[155]
5	2878	(CH_3) sym stretch	[155]
6	2854	(CH_2) sym stretch	[155]

Until this point one can conclude that freshly prepared SAMs that were characterized with XPS and PM IRRAS are composed mostly of compound **8**. The amount of diluent on the surface is insignificant. These layers are not densely packed. They have a more liquid like structure. Further evaluation, that was done on the surfaces only immersed in perchloric acid without any potential applied shows that neither the structure of the molecules on the surface nor the packing of the SAMs did change.

XPS measurements were also performed to investigate electrochemical and chemical conversion on surfaces during electrochemical activation. N 1s and S 2p spectra

of surfaces after activation are shown in Fig. 62 and the assignment of the signal components can be found in Tab 13. S 2p spectra did not change, one can still see the S 2p_{3/2} signal at 161.7 eV and S 2p_{1/2} at 162.8 eV which correspond to sulphur bound to gold. This data show that the molecules were still bound to the gold surface after electrochemical activation. The doublet at S 2p_{3/2} at 163.3 eV and S 2p_{1/2} at 164.4 eV is caused by XP radiation damage as discussed in Chapter 3.3.5. Neither the binding energy of the N 1s peak (399.6 eV), nor the intensity changed. From this, one can conclude that all nitrogen atoms remained in the adsorbed layer on the surface. The ratio between nitrogen and sulphur did not change. (N: S = 1.5: 1)

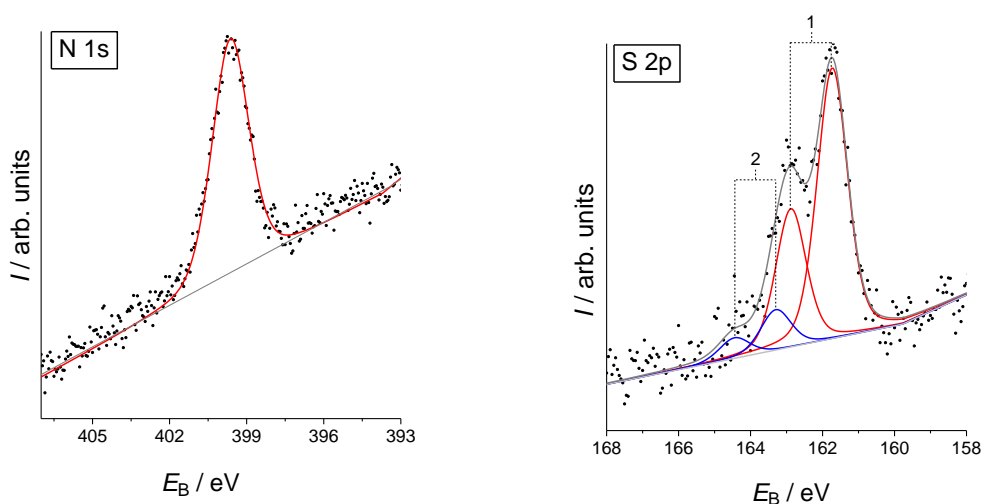


Fig. 62: XPS spectra of SAMs with 1-decanethiol and compound **8** on gold substrate in the N 1s and S 2p region after electrochemical activation in 0.1 M HClO₄. The experimental data points are plotted as dots, the envelope as a dark grey line, single components as red and blue lines and the background a light grey line.

Tab 13: Assignment of XPS peaks form Fig. 62

Signal	Interpretation	E_B / eV	FWHM / eV	Reference
S 2p _{3/2}	R-S-Au	161.7	1.00	[127]
S 2p _{1/2}	R-S-Au	162.8	1.00	[127]
S 2p _{3/2}	radiation damage	163.3	1.00	[151]
S 2p _{1/2}	radiation damage	164.4	1.00	[151]
N 1s	R-N-H	399.6	1.70	[152]

The PM IRRAS spectra that are recorded after the electrochemical activation are shown in Fig. 63 and Fig. 64 and bands are assigned in Tab. 14 and Tab 15, respectively.

In the region $1800 - 900 \text{ cm}^{-1}$ (Fig. 63), the intensities of all bands are significantly decreased compared to the spectra in Fig. 57. One can still see the C=O stretching modes at 1729 cm^{-1} (in ester group) which has an almost constant intensity and one at 1689 cm^{-1} (in amide and urethane group) that significantly decreased. In the CH region (Fig. 64), the CH_3 asymmetric stretching modes of the Boc group decreased in intensity, while the other bands did not change their intensities. Spectroscopic data after electrochemical activation support the reaction mechanism described in Scheme 1. The decrease in intensity of most of the bands in the $1800 - 900 \text{ cm}^{-1}$ region can indicate that molecules after electrochemical activation could react with their neighbouring molecules and polymerize on the surface. This claim also supports the fact that the end product in Scheme 1 is in the oxidized form and as there is no reduction peak corresponding to the electrochemical activation peak (III_a in Fig. 51), this reactive oxidized product of the electrochemical activation is likely to cause polymerization on the surface. From the spectroscopic data it was not possible to explain the formation of the reversible redox couple (I_a and I_c in Fig. 52). Tentatively, it can be concluded that a small fraction of the molecules on the surface remains unpolymerized after the electrochemical activation and can perform the reversible electrochemical reaction.

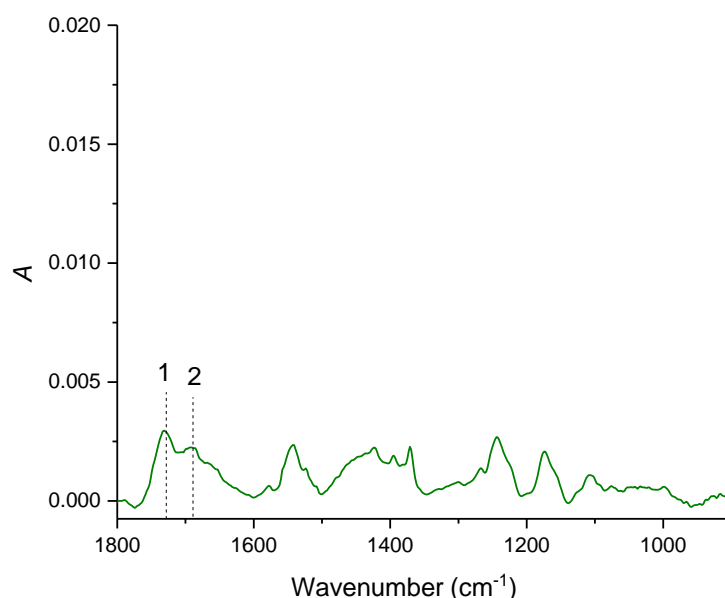


Fig. 63: PM IRRAS spectra of SAMs with compound **8** and 1-decanethiol on gold substrate after electrochemical activation in HClO_4 in region from 1800 cm^{-1} to 900 cm^{-1} .

Tab. 14: Assignment of bands from Fig. 63

Number	Wavenumber / cm^{-1}	Assignment	Reference
1	1729	(C=O) stretch ester	[153, 154]
2	1689	(C=O) stretch amide and urethane	[153, 154]

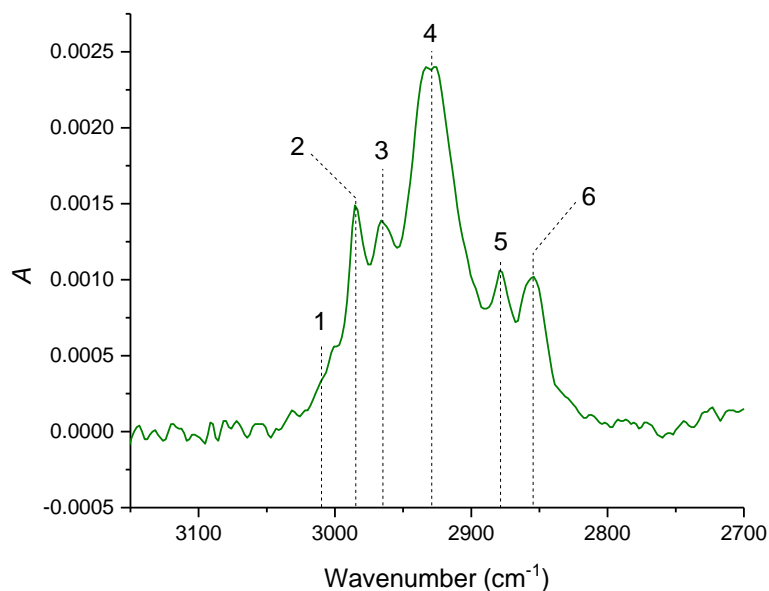


Fig. 64: PM IRRAS spectra of SAMs with compound **8** and 1-decanethiol on gold substrate after electrochemical activation in HClO_4 in region from 3150 cm^{-1} to 2700 cm^{-1} .

Tab 15: Assignment of bands from Fig. 64

Number	Wavenumber / cm^{-1}	Assignment	Reference
1	3009	$(\text{CH})_{\text{ar}}$ stretch	[162]
2	2985	$(\text{CH}_3)_{\text{Boc}}$ asym stretch	[163]
3	2963	(CH_3) asym stretch	[155]
4	2929	(CH_2) asym stretch	[155]
5	2878	(CH_3) sym stretch	[155]
6	2855	(CH_2) sym stretch	[155]

7.3 Electrochemical characterization of DAT derivatives with a fluorinated protecting group

The structure of compound **8** and **9** (described in Chapter 7.1) was modified and instead of the Boc group compounds **10** and **11** have trifluoromethylated benzamine as a potential leaving group. Such a surface reaction can be detected more elegantly with XPS (structure in Fig. 65). SAMs were prepared in the same way as in the previous Chapter.

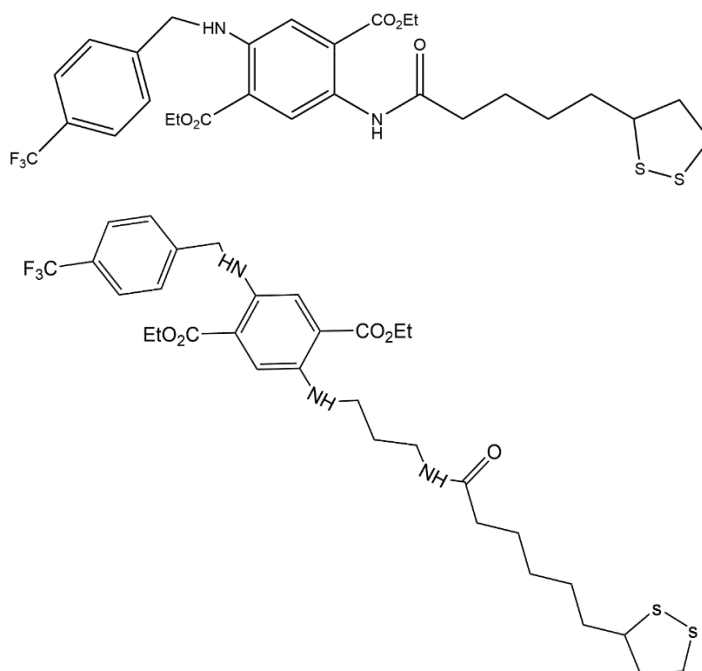


Fig. 65: Structure of compound **10** (up) and **11** (down).

Cyclic voltammograms of compound **10** and **11** are shown in Fig. 66. Compound **10** shows an activation peak at 1.1 V (marked II_a in Fig. 66) but no redox-active reversible couple is formed after electrochemical activation. While compound **11** shows in the first cycle (green line) two irreversible oxidation peaks at 0.78 V (marked IV_a in Fig. 66) and 0.98 V (marked V_a), both peaks are not present in the second cycle. In the second cycle (blue line) a reversible peak appears (anodic and cathodic peak marked as III_a and III_c) at 0.64 V, which did not change in the third cycle (red line) and remained stable since (Fig. 67). As this compound does not have typical urethane group where nucleophilic substitution of H₂O is likely to happen, the mechanism of activation of the surfaces with compound **11** is not the same as for surfaces with compound **8** and is proposed in Scheme 2. The reaction product is the oxidized form of compound **10** and there is no reduction peak that corresponds to the activation peak in cyclic voltammogram. As the final product

in Scheme 2 is in the oxidized form and taking into account the conclusions in the previous Chapter, it can be concluded that the molecules react with the neighbouring molecules and polymerize on the surface after electrochemical activation. A small fraction of the molecules remains unpolimerized and can perform reversible electrochemical reaction similar to mechanism described in the previous Chapter. It remains unclear why there are two oxidation peaks in the electrochemical activation reaction of surfaces with compound **11** and further spectroscopic analysis of the system were performed to clarify this.

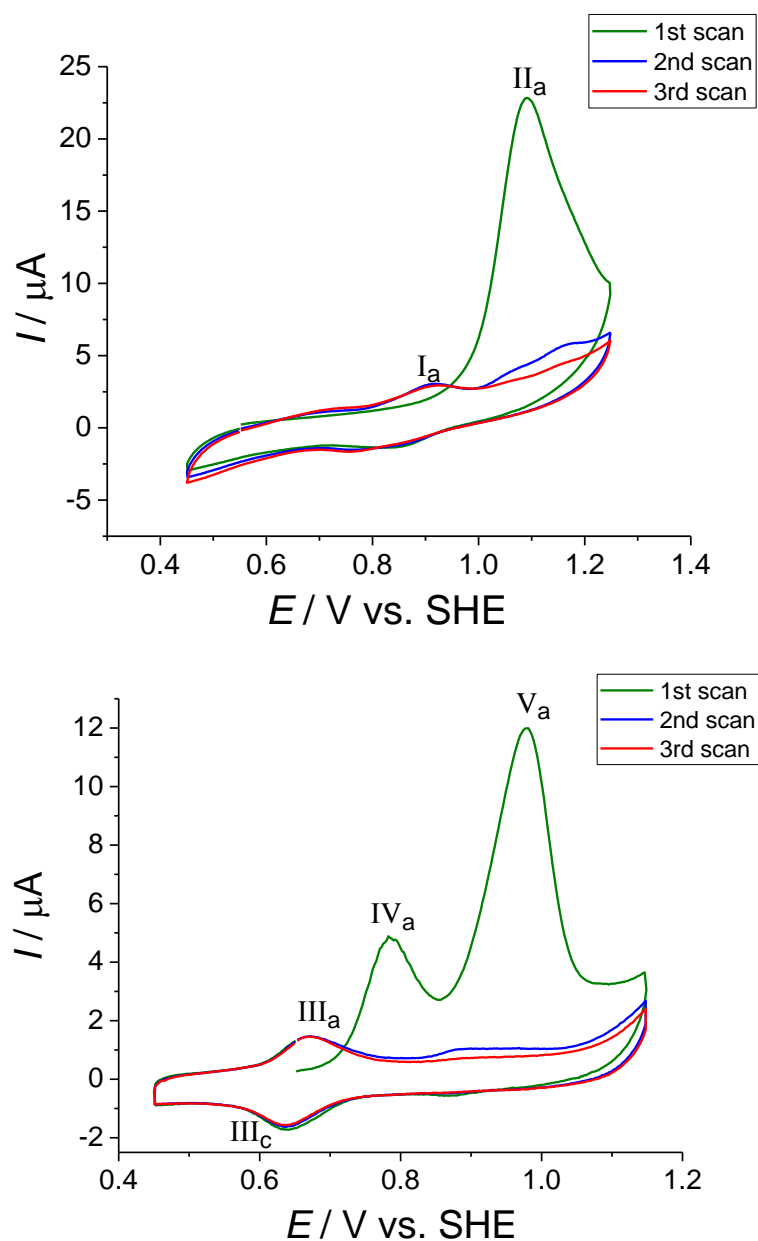


Fig. 66: Cyclic voltammogram of SAMs composed of compound **10** and 1-hexanethiol (up) and of compound **11** and 1-decanethiol (down) on gold substrate in 0.1 M HClO_4 in range from 0.45 V to 1.15 V $v=0.1 \text{ V s}^{-1}$.

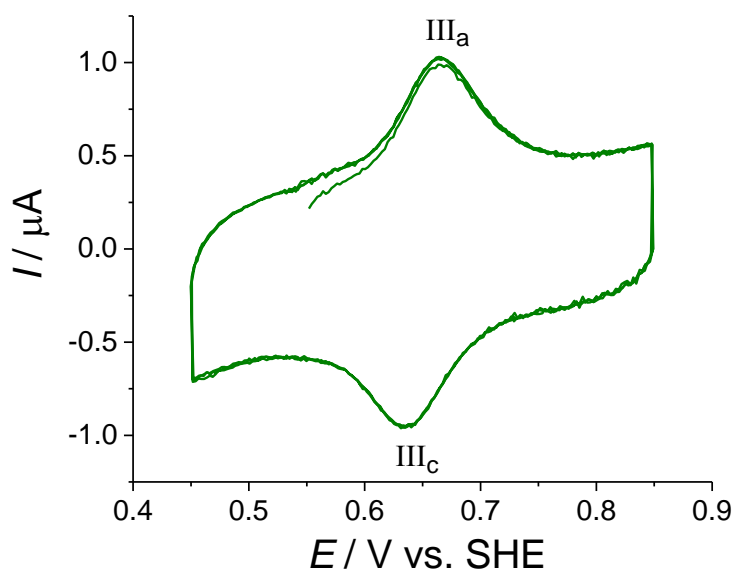


Fig. 67: Cyclic voltammogram of SAMs composed of compound **11** and 1-decanethiol on gold substrate in 0.1 M HClO₄ after electrochemical activation of SAMs in range from 0.45 V to 0.85 V, $\nu=0.1$ Vs⁻¹.

The area under the activation peaks (marked IV_a and V_a in Fig. 66, down) and the peak marked III_a in Fig. 67 was integrated and the charge, Q , was calculated. Afterwards the interfacial concentration Γ of species that are activated and redox-active were calculated with equation (16). The number of electrons transferred in the electrochemical reaction, n , was estimated to be 2 using the equation (17).

$$\Gamma = \frac{Q}{nFA} = \frac{(8.04 + 2.09) \times 10^{-7} \text{C}}{2 \cdot 37.05 \text{mm}^2 \cdot 96485.32 \text{Cmol}^{-1}} = 1.42 \times 10^{-12} \frac{\text{mol}}{\text{mm}^2} \quad (31)$$

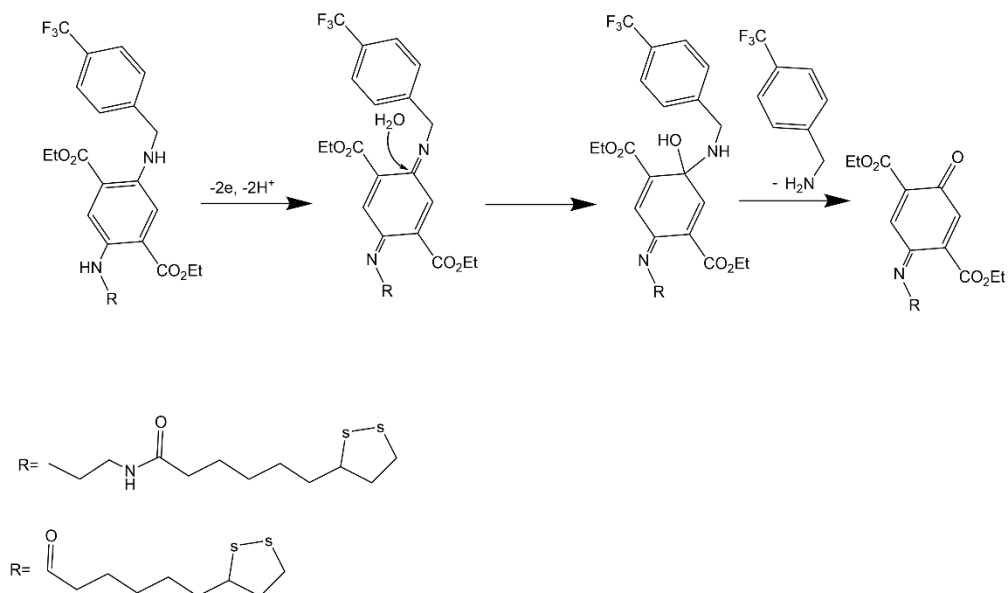
$$\Gamma = 1.42 \times 10^{-10} \frac{\text{mol}}{\text{cm}^2}$$

$$\Gamma = \frac{Q}{nFA} = \frac{4.91 \cdot 10^{-9} \text{C}}{2 \cdot 37.05 \text{mm}^2 \cdot 96485.32 \text{Cmol}^{-1}} = 0.69 \times 10^{-14} \frac{\text{mol}}{\text{mm}^2} \quad (32)$$

$$\Gamma = 0.69 \times 10^{-12} \frac{\text{mol}}{\text{cm}^2}$$

The calculation for the interfacial concentration of the activated species is specified in the equation (31) and for the formed reversible redox couple in the equation (32). The interfacial concentration of molecules that were activated electrochemically at surfaces prepared with compound **11** has similar values as the one prepared from compound **8**. By comparing values of calculated interfacial concentration, it was

determined that only 5 % of molecules that are activated contribute to the reversible peak (marked III_a and III_c in Fig. 67). This number is lower for the half compared to ratio calculated from equations (29) and (30) in Chapter 7.1.



Scheme 2: Mechanism of the electrochemical activation reaction for the compound **10** and **11**.

The heterogenous standard rate constant k°_{ET} as determined from Laviron's theory has a value of 14.60 s^{-1} when calculated from the cathodic peak potentials and 39.21 s^{-1} when calculated from the anodic peak potentials. The average value of electron transfer coefficient, α is 0.32. These values are in good agreement with values for k°_{ET} for structurally similar compounds determined in Chapter 7.1.

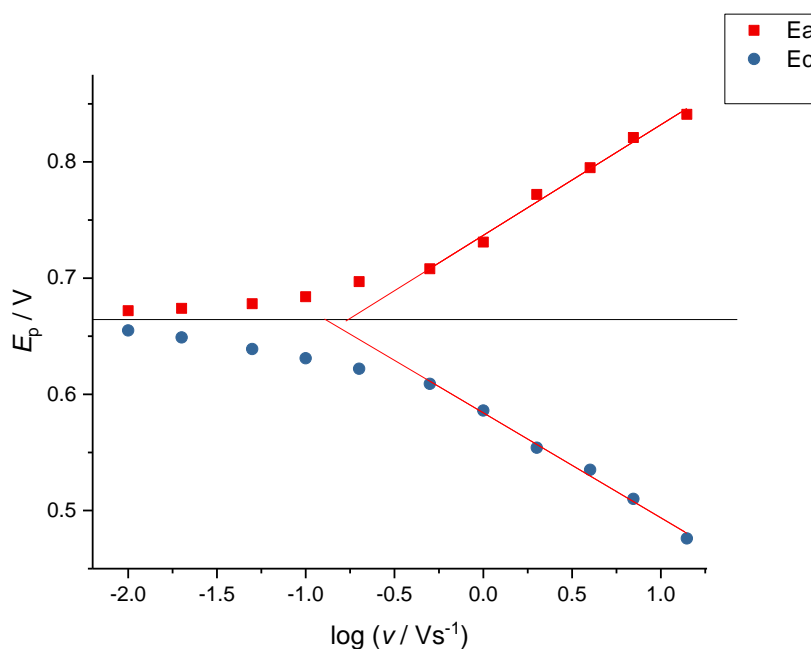


Fig. 68: Plot of peak potential (E_p) of peak III_a and III_c vs $\log(v)$ for electron transfer in cyclic voltammogram in Fig. 67.

7.4 Spectroscopic characterization of surfaces

The XP spectra of a molecular monolayer of compound **11** and 1-decanthiol were recorded before any kind of modification of the surfaces. Fig. 69 shows the results of the peak fit analysis obtained for the C 1s, O 1s, N 1s, F 1s and S 2p spectra. The assignment of the peaks and binding energies are summarized in Tab. 16. The two main peaks in the C 1s spectrum at 284.7 eV (marked 1) and at 285.7 eV (marked 2) have the same assignment as for the surfaces described in previous Chapter. The C 1s spectra contain four smaller peaks lying at binding energies of 287.1 eV (marked 3), 288.8 eV (marked 4), 290.1 (marked 5) and 292.9 eV (marked 6). The first three peaks have the same assignment as ones in Chapter 7.2. The one at 292.9 eV (marked 6) corresponds to carbon bound to fluorine. Because of the high electronegativity of fluorine, the binding energies are shifted to high values. The O 1s spectrum has two main peaks at 531.8 eV (marked 1) and 533.7 eV (marked 2). These peaks have the same assignment as the one in previous monolayer. Because of the similarity of binding energies of the oxygen in adsorbed water molecules at surface, this will not be included in further discussion [150]. The S 2p spectra has the main doublet at 161.8 eV and 163.0 eV (marked 1) corresponding to sulphur bound to gold and a doublet at 163.5 eV and 164.8 eV (marked 2) which is caused by

radiation damage of the monolayers. There is only one type of nitrogen at binding energy of 399.7 eV. It corresponds to all nitrogen atoms in compound **11**. Fluorine in the compound **11** is detected at binding energies of 688.5 eV which is typical for the F₃-C group [164–166]. Atomic ratios of the surface normalized to sulphur are: C: O: N: F: S = 16.7: 3.1: 1.3: 1.8: 1. The elemental ratios in the molecule are: C: O: N: F: S = 16: 2.5: 1.5: 1.5: 1 which is in good agreement with the ratio on the surface. The higher amount of carbon can be explained by the presence of diluent and contamination on the surface. The higher amount of oxygen can be explained by adsorbed water molecules on the surface. The amount of diluent is not significant on the surface and that can be proven by the fact that ratio of nitrogen compared to sulphur is almost the same in the compound and on the surface.

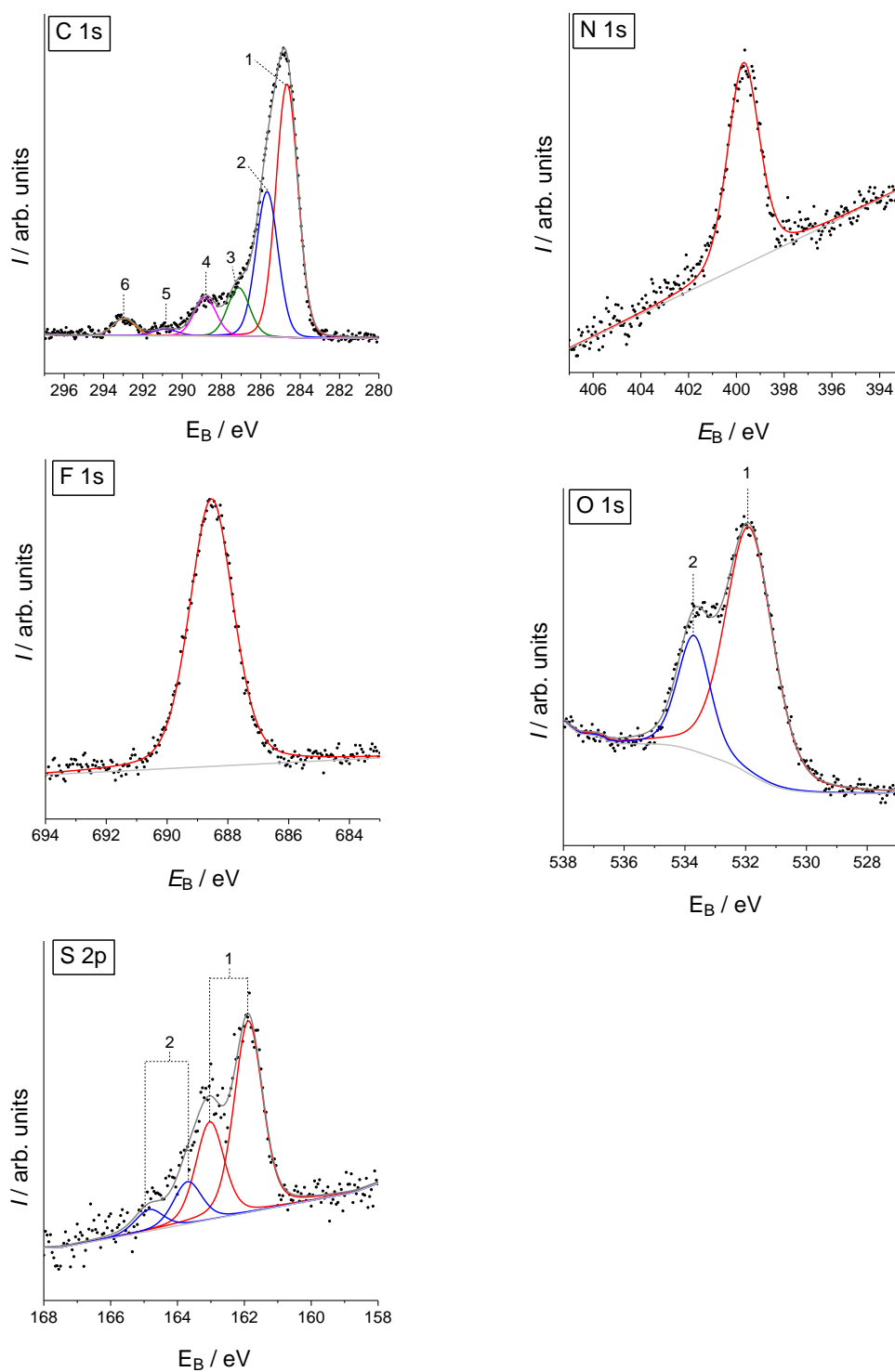


Fig. 69: XP spectra of SAMs with 1-decanethiol and compound **11** on gold substrate in the C 1s, N 1s, F 1s, O 1s and S 2p region. The experimental data points are plotted as dots, the envelope as a dark grey line, single components as red, blue, orange, green, purple and pink lines and the background a light grey line.

Tab. 16: Assignment of fitted spectra from Fig. 69

Signal	Interpretation	E_B / eV	FWHM / eV	Reference
S 2p _{3/2}	R-S-Au	161.8	1.00	[127]
S 2p _{1/2}	R-S-Au	163.0	1.00	[127]
S 2p _{3/2}	radiation damage	163.5	1.00	[151]
S 2p _{1/2}	radiation damage	164.8	1.00	[151]
C 1s	C-C, C-S	284.7	1.32	[147]
C 1s	C-N, C-O	285.7	1.32	[147]
C 1s	ester and amide	287.1	1.32	[147]
C 1s	contamination	288.8	1.32	/
C 1s	shake-up	290.1	1.70	[148]
C 1s	C-F3	292.9	1.32	[164–166]
O 1s	C=O	531.8	1.86	[149]
O 1s	C-O, H ₂ O	533.7	1.27	[149]
N 1s	R-N-H	399.7	1.58	[152]
F 1s	F ₃ -C	688.5	1.70	[164–166]

After immersion in perchloric acid for 15 min, XP spectra were recorded (Fig. 70). The peak assignment is summarized in Tab. 17. One cannot see significant changes in the spectra. The normalized atomic ratio to S 2p peak is: N:F:S = 1.4: 1.4: 1. Here one can see that the amount of fluorine is lower by the factor of 0.4 compared to Fig. 69. This value is in the error range of a quantitative analysis of XPS.

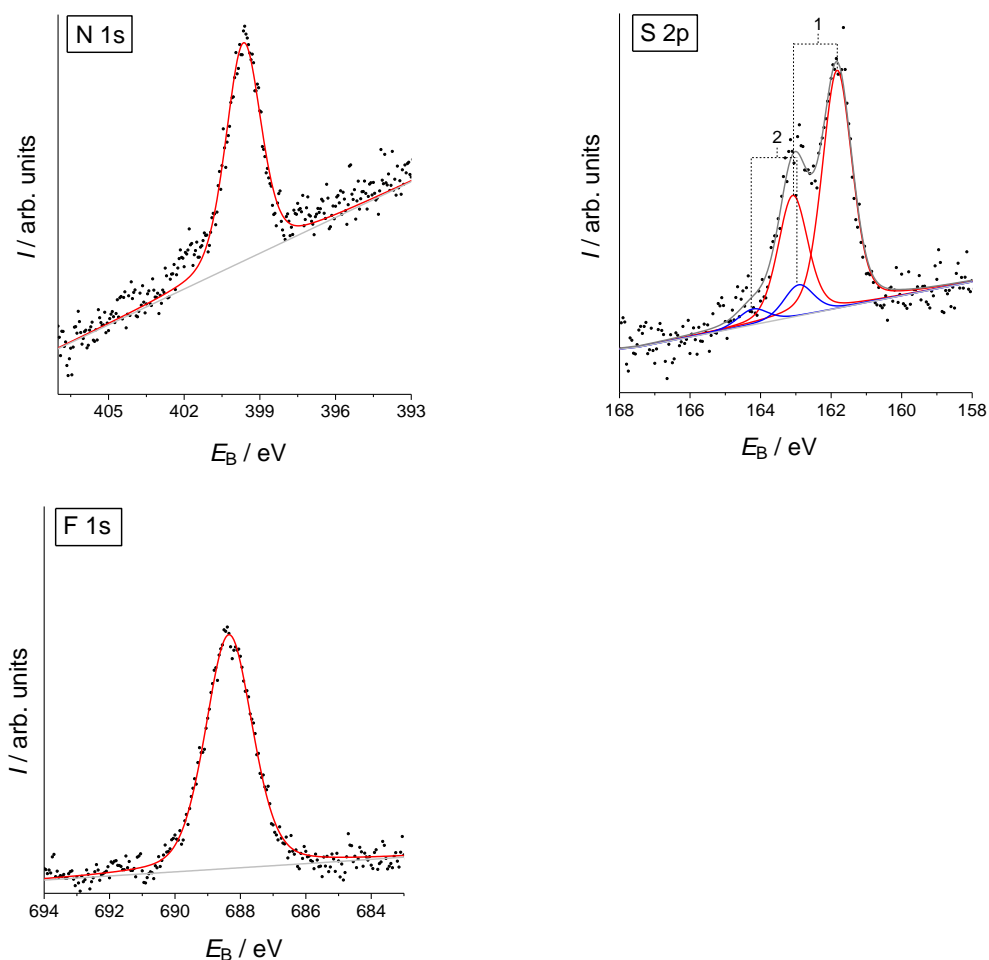


Fig. 70: XPS spectra of SAMs with 1-decanethiol and compound **11** on gold substrate in the N 1s, F 1s and S 2p region after immersion in HClO₄. The experimental data points are plotted as dots, the envelope as a dark grey line, single components as red and blue lines and the background a light grey line.

Tab. 17: Assignment of fitted spectra from Fig. 70

Signal	Interpretation	E_B / eV	FWHM / eV	Reference
S 2p _{3/2}	R-S-Au	161.8	1.00	[127]
S 2p _{1/2}	R-S-Au	163.1	1.00	[127]
S 2p _{3/2}	radiation damage	163.0	1.00	[151]
S 2p _{1/2}	radiation damage	164.20	1.00	[151]
N 1s	R-N-H	399.7	1.64	[152]
F 1s	F ₃ -C	688.4	1.70	[164–166]

After the first oxidation peak at 0.78 V, XPS analysis of the surfaces was performed. Fitted spectra of N 1s, S 2p and F 1s are shown in Fig. 71. The peak assignment and

binding energies are shown in Tab. 18. The atomic ratios normalized to sulphur are N:F:S = 1.3:0.9:1. When comparing these values to the ones from unmodified surfaces, one can see that the amount of fluorine is reduced by one half. This means that in the first activation peak, part of the surface was electrochemically activated. On the other hand, the amount of nitrogen did not change. By the reaction mechanism part of nitrogen should also be removed from the surface, but this could not be detected by quantitative analysis of XPS data because the technique is not sensitive enough for this change of surface concentration.

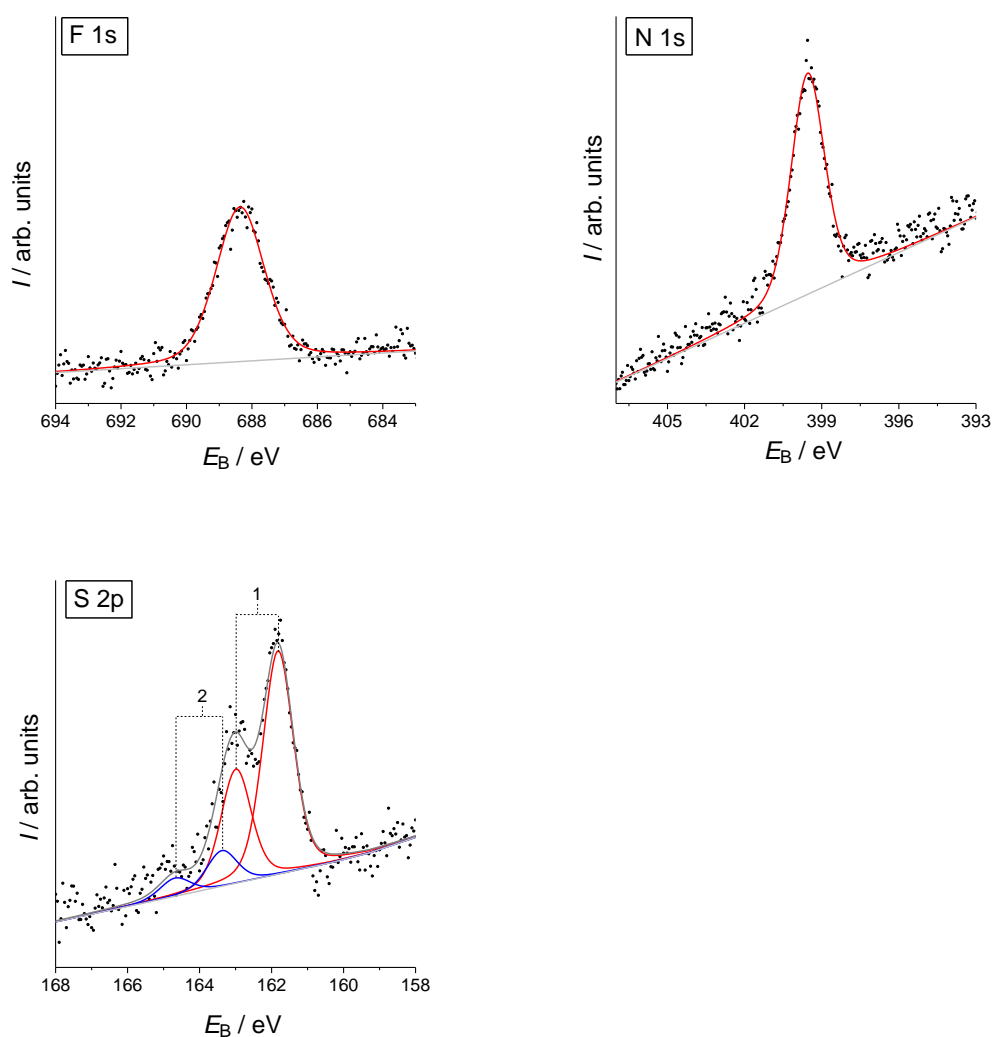


Fig. 71: XP spectra of SAMs with 1-decanethiol and compound **11** on gold substrate in the N 1s, F 1s and S 2p region after oxidation peak at 0.78 V. The experimental data points are plotted as dots, the envelope as a dark grey line, single components as red and blue lines and the background a light grey line.

Tab. 18 Assignment of fitted spectra from Fig. 71

Signal	Interpretation	E_B / eV	FWHM / eV	Reference
S 2p _{3/2}	R-S-Au	161.8	1.00	[127]
S 2p _{1/2}	R-S-Au	163.0	1.00	[127]
S 2p _{3/2}	radiation damage	163.4	1.00	[151]
S 2p _{1/2}	radiation damage	164.7	1.00	[151]
N 1s	R-N-H	399.6	1.54	[152]
F 1s	F ₃ -C	688.4	1.74	[164–166]

Fitted spectra of fully activated surfaces are shown in Fig. 72 with summarized peak assignment in Tab. 19. One can see a significant loss of fluorine from the surface (N: F: S = 1.3: 0.5: 1). From quantitative analysis, it is estimated that around one third of fluorine is left on surface when compared with the unmodified surfaces. Here loss of nitrogen from the surface could not be detected. With rough calculation it is estimated that a fraction of 0.28 of the original nitrogen content was removed from surface. Such small change cannot always be detected with XPS.

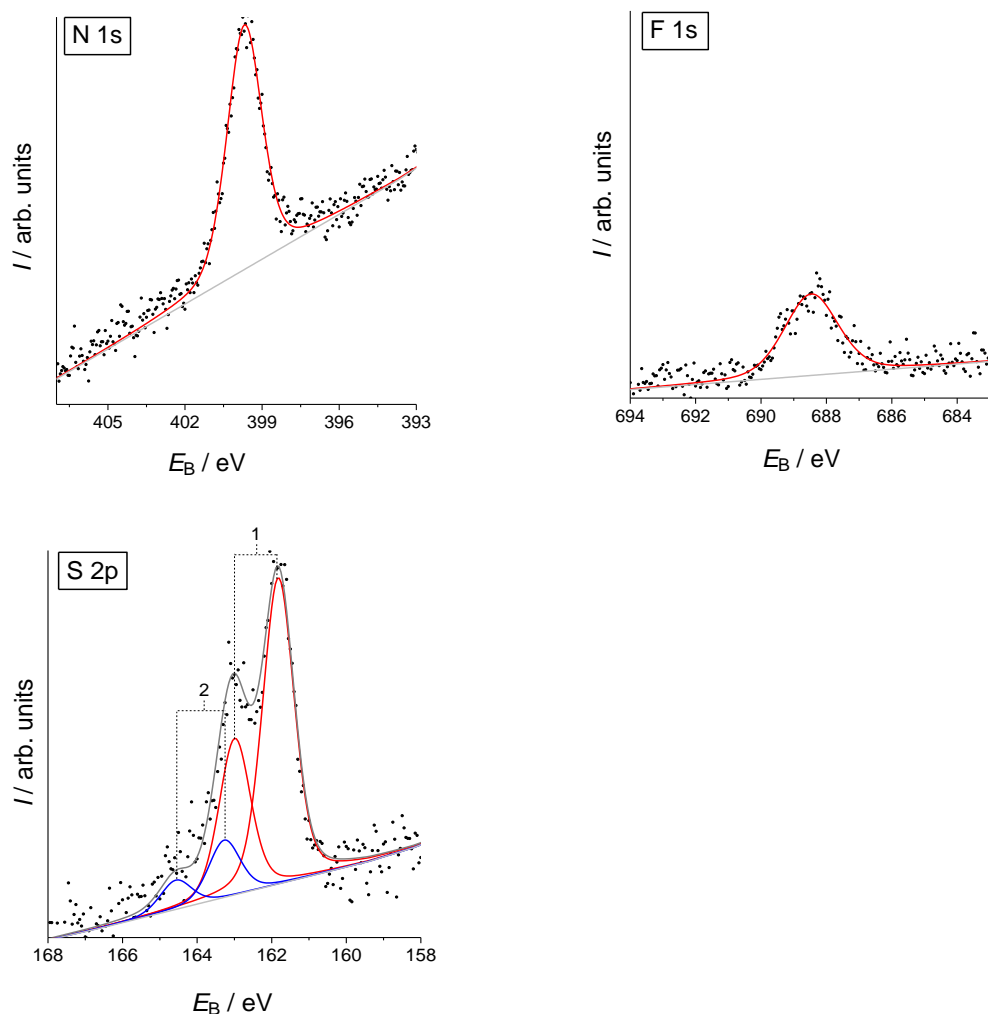


Fig. 72: XP spectra of SAMs with 1-decanethiol and compound **11** on gold substrate in the N 1s, F 1s and S 2p region after the oxidation peak at 0.98 V. The experimental data points are plotted as dots, the envelope as a dark grey line, single components as red and blue lines and the background a light grey line.

Tab. 19: Assignment of fitted spectra from Fig. 72.

Signal	Interpretation	E_B / eV	FWHM / eV	Reference
S 2p _{3/2}	R-S-Au	161.8	1.00	[127]
S 2p _{1/2}	R-S-Au	163.0	1.00	[127]
S 2p _{3/2}	radiation damage	163.3	1.00	[151]
S 2p _{1/2}	radiation damage	164.6	1.00	[151]
N 1s	R-N-H	399.5	1.64	[152]
F 1s	F ₃ -C	688.5	1.90	[164–166]

After electrochemical and spectroscopic analysis of the SAMs that contain compound **11**, one can ask the questions why 1/3 of the original fluorine content is left on the surface.

This can be explained by the fact that the tailgroup in compound **11** is hydrophobic and as electrochemical activation is carried out in aqueous solution, a certain portion of the tailgroups is buried in layer and others are sticking out from the surface. These two conformations can have different oxidation potentials as their electrochemical environment is different. Therefore, two well separated oxidation peaks are present in cyclic voltammogram of the electrochemical activation of surfaces. The part of the tailgroups that is buried in the layer cannot leave surface after electrochemical activation, which is the reason why after activation one can still see one third of the fluorine left on the surface.

7.5 Addition reaction on surface

The redox-active species (I_a and I_c Fig. 52) that were generated at surfaces containing compound **8**, described and characterized in Chapter 7.1, can be used for binding effectors to the surface. The surfaces undergo an addition reaction with an effector from the solution when the surface is in its oxidized state. As a proof of concept, we used 3-(trifluoromethyl)aniline to simulate an effector because the fluorine group function in this compound can easily be detected by XPS in the modified monolayers.

A cyclic voltammogram of the electrochemically controlled addition reaction is shown in Fig. 73. It displays the typical behaviour of the EC reaction mechanism of surface-immobilized species. Firstly, the molecules at the surface are oxidized. This form of the molecule is active and it binds 3-(trifluoromethyl)aniline in an 1,4-addition reaction. (Schematic representation of the 1,4-addition reaction is presented in Fig. 74.) With each cycle more molecules are attached to the surface and the oxidation and reduction peak of couple I_a/I_c decrease. Experiments without 3-(trifluoromethyl)aniline show almost constant oxidation and reduction peak current (Fig. 52).

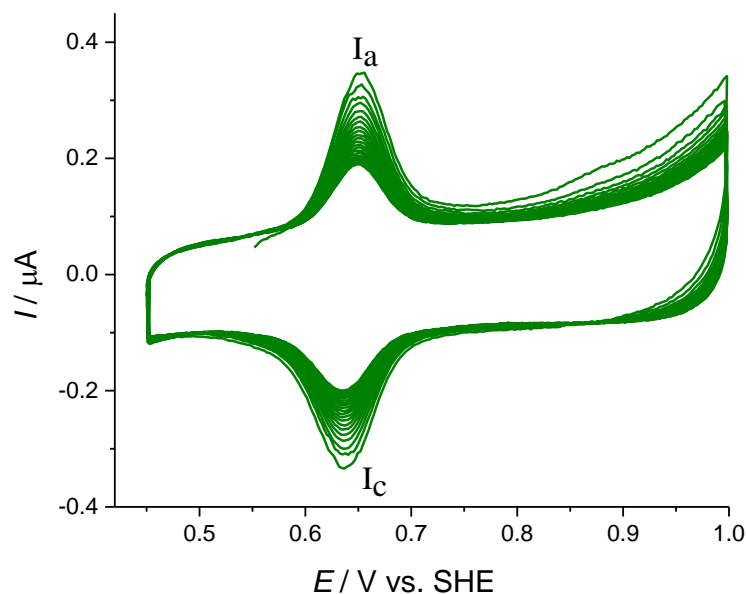


Fig. 73: Cyclic voltammogram of surface addition reaction of SAMs containing compound **8** on gold substrate in solution of 0.1 M 3-(trifluoromethyl)aniline in 0.1 M HClO₄, $\nu=0.02\text{Vs}^{-1}$.

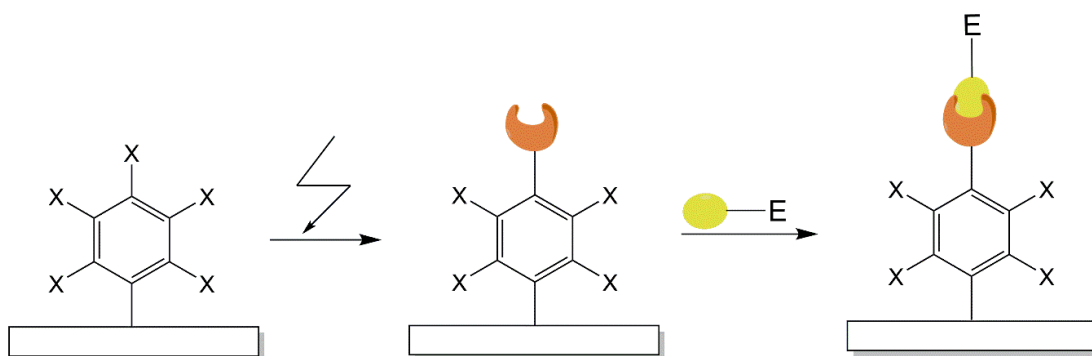


Fig. 74: Schematic representation of 1, 4-addition reaction: in the first step molecule is activated by applying potential, in the second step effector is attached to the molecule bound to the surface by 1, 4-addition reaction. Brown/orange part of surface immobilized species represents the part of the molecule where effector is bound, the yellow part of effector is group with which effector is bound to the surface immobilized species.

XP spectra of F 1s peaks are shown in Fig. 75. The spectra in Fig. 75a is from the surface where the addition reaction was performed. The spectra in Fig. 75b was obtained from a surface where the monolayers were exposed to electrolyte for 15 min without potential cycling. One can see that in Fig. 75a fluorine is present on the surface while this is not the case for spectra in Fig. 75b. This excludes the possibility of physisorption of the nucleophile on the surface. XP spectra in Fig. 75 are proof that 3-(trifluoromethyl)aniline was bound to the surface by an addition reaction with the oxidized form of the redox couple I_a/I_c formed during electrochemical surface activation. When the atomic ratios of sulphur and fluorine from XPS signals are compared, it was determined that 10% of

surface molecule underwent the addition reaction with the nucleophilic molecule. In Chapter 7 the interfacial concentration of activated species (IIIa in Fig. 51) and formed redox-active couple (I_a/I_c in Fig. 52) was calculated with equation (29) and (30). From the interfacial concentrations from these two equations it was determined that 10% of molecules that are activated are redox-active, which can be estimated to be 10% of the surface since the amount of diluent molecules is insignificant. As stated earlier in this paragraph, it was determined that in fact 10 % of surface was modified with 1, 4-addition reaction, one can conclude that the majority of molecules that were redox-active have performed addition reaction with the nucleophilic molecule.

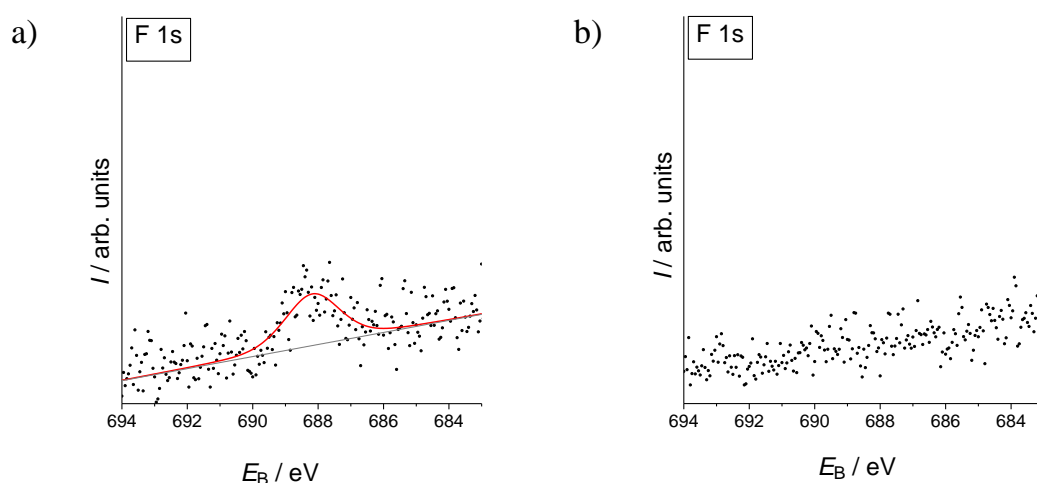


Fig. 75: XP spectra of SAMs with 1-decanethiol and compound **8** on gold substrate in the F 1s region of surfaces a) after addition reaction, b) of surfaces that were in solution of 0.1 M 3-(trifluoromethyl)aniline in 0.1 M HClO_4 . The experimental data points are plotted as dots, single component as red line and the background a black line.

8 Summary and Outlook

The aim of this project was to investigate molecules which can be potentially used in light-harvesting device. The molecules were investigated with electrochemical and spectroscopic methods. The molecules were also assembled on the surfaces and it was demonstrated that those surfaces can perform addition reaction when a potential was applied. This Chapter summarizes all results and gives a conclusion with suggested direction for future investigations.

8.1 Summary of investigated systems

The initial part of the research was focused on the electrochemical and spectroelectrochemical characterization of $[(\text{Cp}_2\text{Ti})_3\text{HATN}(\text{Ph})_6]$ (Chapter 5). In voltammograms of $[(\text{Cp}_2\text{Ti})_3\text{HATN}(\text{Ph})_6]$ three reduction waves and six oxidation waves are observed. All electron transfers are one electron processes clearly separated on the potential scale. The six oxidations correspond to the sequential removal of six valence electrons of the three Ti(II) centres. The two reductions for the overall charging states $0 \rightarrow -1$ and $-1 \rightarrow -2$ result from the reduction of the ligand, which was in agreement with voltammogram from the ligand only. The third reduction ($-2 \rightarrow -3$) cannot be assigned from voltammetric data only. Until today in literature the nine reversible redox steps of $[(\text{Cp}_2\text{Ti})_3\text{HATN}(\text{Ph})_6]$ are unprecedented.

The solution spectra of $[(\text{Cp}_2\text{Ti})_3\text{HATN}(\text{Ph})_6]$ and their oxidation and reduction products $[(\text{Cp}_2\text{Ti})_3\text{HATN}(\text{Ph})_6]^{3-}$, $[(\text{Cp}_2\text{Ti})_3\text{HATN}(\text{Ph})_6]^{2-}$, $[(\text{Cp}_2\text{Ti})_3\text{HATN}(\text{Ph})_6]^{1-}$, $[(\text{Cp}_2\text{Ti})_3\text{HATN}(\text{Ph})_6]^{1+}$ and $[(\text{Cp}_2\text{Ti})_3\text{HATN}(\text{Ph})_6]^{2+}$ show electronic transitions in the UV, vis and NIR spectral ranges. The existence of the SOMO in the ground state of complex gives several characteristic electronic transitions. The most characteristic transition in the UV-vis part of the spectra is the $\pi-\pi^*$ from the HOMO to the LUMO orbital of the ligand at 3.0 eV. In this region, there are also the $\pi-\pi^f$ transition at 1.7 eV and the degenerated intervalence charge transfer (IVCT) from the Ti(II)(e) to the LUMO orbital of the ligand. In the NIR region of the spectra the $\pi^f-\pi^*$ transition can be seen at 1.1 eV, LMCT at 0.6 eV and 0.75 eV and the IVCT from the Ti(II)(e) to the SOMO orbital of the ligand at around 0.9 eV. In the -1 and the -2 oxidation state one loses IVCT

because all Ti atoms are in the same oxidation state. Now a MLCT is observed. In the -1 oxidation state all transitions are shifted to lower energies, in the -2 some transitions are lost because the SOMO orbital is filled with an electron. In the -3 oxidation state, one orbital of the Ti atom is filled with an electron so the complex is in the mixed valence state again. In the +1 oxidation state an electron is removed from the SOMO orbital, some transitions are lost compared to ground state of complex. In the +2 oxidation state one can see all transitions as in the +1 oxidation state. In NIR part of spectra the MLCT transitions cannot be resolved so exact energies of the transitions cannot be determined.

As a second focus of the thesis, the derivatives of 2,5-diaminoterephthalate were characterized electrochemically and spectroscopically as a molecular scaffold, which can be functionalized with up to four different effector groups. The alternation of functional groups on the DAT moiety influences not only the formal potentials, but also the mechanism of the electrochemical reaction. Functional groups can act as protection, so the radical cation that is created in first oxidation does not react immediately with the environment and it is reduced in further cycle. Functionalization with electron withdrawing groups (such as Boc group) leads to oxidation at really high potentials, which cannot be followed in the potential range of the voltammograms. Surprisingly, DATs with completely different substituents at the DAT core (compound **1** and compound **4**) show completely identical redox behaviour with a difference in formal potential E° of 0.02 V. Variation of functional groups at the DATs moiety can also be seen in shifts of the wavelength of maximum of absorption and emission. Electrochemical and spectroscopic data, the formal potential of the first oxidation and the wavelength of emission and absorption maximum were correlated. This correlation for wavelength of maximum absorption and emission holds with high precision for DATs with methyl or acetyl functionalities attached to the DAT scaffold. The formal potential of the first oxidation can be established by measuring the wavelength of emission and absorption maximum.

In the next step, DATs were functionalized with lipoic acid in order to be assembled on the surfaces as self-assembled monolayers. Four different DAT molecules were assembled onto surface with backfilling method and their electrochemical behaviour was investigated in perchloric acid. Depending on the structure of the tail group of the molecules, cyclic voltammograms exhibit different features. In the first cycle compound

8, **10** and **11** were electrochemically activated, firstly oxidizing the chromophore followed by a nucleophilic attack by H₂O where the protecting group is removed. Interestingly on the surfaces with assembled compound **8** and **11** that have longer spacer, a stable and reversible redox couple is formed after electrochemical activation. Although the molecules have similar structure and cyclic voltammograms, the mechanism of electrochemical activation is not the same.

In electrochemical activation of compound **8**, the Boc group was cleaved as proven by XPS and PM IRRAS spectra of the surfaces. In XP spectra of surfaces without modification, surfaces that were in perchloric acid without applied potential and after electrochemical activation, one could not see changes in intensities or binding energies of N 1s and S 2p spectra. On the other hand, PM IRRAS spectra in region 1800 – 900 cm⁻¹ of activated surface exhibit significant changes compared to surfaces that were in perchloric acid without applied potential and surfaces without modification. Most of the intensities of the bands in 1800 – 900 cm⁻¹ region significantly decreased, only the intensity of C=O stretching modes at 1729 cm⁻¹ and 1689 cm⁻¹ could be seen clearly. The ratio of the intensities of C=O stretching modes is changed after activation reaction. In the CH region, only the intensity of asymmetric CH₃ stretching modes in the Boc group decreased upon electrochemical activation. This proved that chains of monolayer stayed intact during activation.

SAMs which contain compound **11** have fluorine in the potential leaving group and electrochemical activation could be followed elegantly with XPS. Firstly, in cyclic voltammogram of the electrochemical activation one can see two activation peaks instead of one which was present for compound **8** and **10**. When comparing spectra of surfaces without any kind of modification and spectra of surfaces which were in perchloric acid without any electrochemical treatment the amount of fluorine is almost doubled comparing to those after the first oxidation peak. The surfaces after complete electrochemical activation have lost two thirds of fluorine originally present.

The activation of the surfaces that contain compound **8** enables binding of effector groups. The modified surfaces undergo an 1, 4-addition reaction with an effector from the solution when the surface is in its oxidized state. As a proof of concept, 3-(trifluoromethyl)aniline was used as an effector. In cyclic voltammogram in solution of

perchloric acid with 3-(trifluoromethyl)aniline, one can see the typical behaviour the EC reaction mechanism for the surface immobilized species. From the XPS data, one can conclude that around 10% of the DAT molecules were modified with addition reaction.

8.2 Conclusion and outlook

In conclusion, this thesis carries on investigation of two different part of light harvesting systems, $[(\text{Cp}_2\text{Ti})_3\text{HATN}(\text{Ph})_6]$ and eleven derivatives of DATs. DAT chromophore proved to be a versatile tool which can be functionalized by up to four effector groups. Even though their structure is only slightly modified, the behaviour of the DAT changes significantly. Based on the results of this thesis, the two investigated systems compound **8** and $[(\text{Cp}_2\text{Ti})_3\text{HATN}(\text{Ph})_6]$ can act as parts of light harvesting devices. However, a breakthrough in building such light harvesting device requires improvements in several interdependent aspects of the system.

Firstly, HATN complexes or similar multicentre complexes should be further modified so that they can be stable in air and soluble in aqueous solutions. Then, this type of complexes could be bound to the surface investigated in Chapter 7.5. Afterwards, interaction between these two entities and electron transfer reactions could be investigated with electrochemical and spectroscopic techniques.

Self-assembled monolayers that were created with derivatives of DATs could be activated in local patterns by scanning electrochemical microscopy. This could be achieved with microelectrodes which would be positioned above the sample. At the microelectrode, a potential would be applied to cause the oxidation, in the electrolyte, of a mediator present in the solution. The oxidized mediator would diffuse to the self-assembled monolayer and oxidize the DAT moiety. In this way surface can be activated in a patterned way and different molecular entities could be assembled on different regions of the surfaces. The interaction of this molecular entities could be investigated electrochemically. Depending on the nature of the entities bound to the surface, the energetic interaction in this system could also be studies by spectroscopic methods. These systems would provide an excellent basis for electron transfer reactions in energy

harvesting processes used for electricity generation, selective chemical conversions or sensory purposes if biological or biomimetic receptors are bound to the surface.

Even though DATs are fluorescent molecules, fluorescence spectroscopy of the monolayers could not be recorded because fluorescence was quenched by the gold substrate[167, 168]. Further modification of the DAT backbone is necessary, to anchor the system on oxidic surfaces like conducting glass (rather than gold). In this way surfaces could be characterized by fluorescent spectroscopy. Because the emission spectra changes with the binding of effectors, the progress of surface modification could be monitored spectroscopically which is independent on the applied potential by which the activation itself is externally switched on or off.

Overall, a modification of the multicentre complexes and DATs investigated in this thesis in the above-mentioned way followed by their characterization and building of light harvesting devices composed of these two entities of would be of interest. Especially because the electron transfer processes between these two remarkable molecular units can be investigated which could maybe contribute to efficiency in electron transfers in artificial light harvesting devices.

9 Appendix

Abbreviation

Aux	auxiliary electrode
CE	counter electrode
CME	chemically modified electrode
Cp	cyclopentadiene
CV	cyclic voltammetry
DAT	2,5-diaminoterephthalate
D-A	Diels-Alder reaction
DCM	dichloromethane
DPV	differential pulse voltammetry
DPPD	N,N'-diphenyl-p-phenylenediamine
ESCA	electron spectroscopy for chemical analysis
FWHM	full width at half of the peak maximum height
GC	glassy carbon
HAT	hexaazatrinaphthylene
HATN	hexaazatriphenylene
IMFP	the inelastic mean free path
IR	infrard
IRRAS	infrared reflection absorption spectroscopy
ITO	indium doped tin oxide
IVCT	intervalence charge transfer
LMCT	charge transfer between the ligand and the metal centre
LSV	linear sweep voltammetry
MLCT	charge transfer between the metal centre and the ligand
NIR	near-infrared
OCP	open circuit potential
PEM	photoelastic modulator

PM IRRAS	polarization modulation infrared reflection-absorption spectroscopy
PPD	<i>p</i> -Phenylenediamine
RE	reference electrode
SAM	self-assembled monolayer
THF	tetrahydrofuran
UHV	ultra-high vacuum
UV-vis	ultraviolet–visible
WE	working electrode
X-AES	X-ray induced Auger electron spectroscopy
XPS	X-ray photoelectron spectroscopy

Symbols

A	electrode surface area
c	bulk concentration
d	thickness
d	diameter
D	diffusion coefficient
E°	formal potential
\vec{E}	the electric field
E_B	binding energy
E_{kin}	kinetic energy
E_p	peak potential
E_{pa}	anodic peak potentials
E_{pc}	cathodic peak potentials
\vec{E}_z	<i>z</i> -component of electric field
E_λ	vertex potential
ΔE_p	separation between two peak potentials
F	Faraday constant
$h\nu$	photon energy

$\Delta I = I_s - I_p$	signal difference of s- and p-polarized light
$\langle I \rangle = (I_s + I_p)/2$	averaged signal of s- and p-polarized light
$I(A)$	intensity of a photoelectron peak from an element A in a substrate covered with a film of thickness d
$I_0(A)$	intensity of the same peak from a clean substrate
I_p	peak current
I_{pa}	anodic peak current
I_{pc}	cathodic peak current
$I_{pc,0}$	uncorrected cathodic peak currents to the zero-current baseline
I_λ	current at the vertex potential
$J_1(\Psi_0)$	Bessel functions of first order
$J_2(\Psi_0)$	Bessel functions of second order
k_{ET}	rate of electron transfer
l	angular momentum quantum number
n	principal quantum number
n	number of electrons
n_1	refractive indices of the media 1
n_2	refractive indices of the media 2
Q	charge under the peak
R	gas constant
s	spin angular momentum number
T	temperature
v	scan rate
v_a	regression lines for the anodic and branch
v_c	regression lines for the cathodic branch
α	transfer coefficient
Γ	interfacial concentration of the redox-active species
γ_1	angle of the incident light
γ_2	broken angle of the transmitted light

θ	angle between transition dipole moment and the electric field of the light
θ	angle between the plane of the substrate and the detector
λ	attenuation length
$\vec{\mu}$	transition dipole moment
φ	work function and is specific to the spectrometer
Ψ_0	maximum shift of incident light produced by PEM
ω_m	excitation frequency of the PEM

10 Own publications and conference contributions

10.1 Publications

P. Sander, A. Markovic, M. Schmidtman, O. Janka, G. Wittstock, R. Beckhaus, "Synthesis, Crystal structures, Magnetic and Electrochemical Properties of Highly Phenyl substituted Trinuclear 5,6,11,12,17,18- Hexaazatrinaphthylene (HATNPh₆)-bridged Titanium Complexes", *Inorg. Chem.* **2018**, *57*, 11165-11174.

H. Kollmann, M. Esmann, J. Witt, A. Markovic, V. Smirnov, G. Wittstock, M. Silies, C. Lienau, "Fourier-Transform Spatial Modulation Spectroscopy of Single Gold Nanorods", *Nanophotonics* **2018**, *7*, 715-726

10.2 Oral presentations in national and international conferences

A. Marković, G. Wittstock;"Surface Modification by Self-Assembled Monolayers of Fluorescent Dyes", 2nd International Meeting *on* Materials Science for Energy Related Applications, Belgrade, Serbia, 29 Sep- 30 Sep 2016. (in English)

A. Marković, P. Fangmann, R. Beckhaus, G. Wittstock;" Electrochemical and spectroscopical investigations of trinuclear titanium complexes ", ECHEMS 2017, Milano Marittima, Italy, 6 June - 9 June 2017. (in English)

A. Marković, P. Fangmann, R. Beckhaus, G. Wittstock;" Electrochemical and spectroelectrochemical studies on electron transfer reactions on transition metal complexes with π -acceptor ligands ", 6th Regional Symposium on Electrochemistry of South-East Europe, Balatonkenese, Hungary, 11 June - 15 June 2017. (in English)

A. Marković, Leon Buschbeck, Jens Christoffers, G. Wittstock;" Fluorescent dyes for electrochemical sensing – Electrochemical activation of self-assembled monolayers ", 3rd International Meeting *on* Materials Science for Energy Related Applications, Belgrade, Serbia, 25 Sep- 26 Sep 2018. (in English)

10.3 Posters in national and international conferences

A. Marković, I. Pašti, N. Gavrilov, S. Mentus;" Adsorption of acetonitrile on platinum and its effects on oxygen reduction reaction – Combined theoretical and experimental study", 11th ECHEMS, Bad Zwischenahn, Germany 15 June - 18 June 2015. (in English)

A. Marković, G. Wittstock;"Surface Modification by Self-Assembled Monolayers of Fluorescent Dyes", 7th International Workshop on Surface Modification for Chemical and Biochemical Sensing, Pultusk Castle, Poland, 6 Nov – 10 Nov 2015. (in English)

A. Marković, G. Wittstock; "Surface Modification by Self-Assembled Monolayers of Fluorescent Dyes", 7th ElecNano, Lille, France ,23 May-25 May 2016. (in English)

A. Marković, G. Wittstock; A. Marković, L. Freimuth, J. Christoffers, G. Wittstock; "Surface Modification by Self-Assembled Monolayers of Fluorescent Dyes", GDCh-Electrochemistry 2016, Goslar, Germany, 26 Sep - 28 Sep 2016. (in English)

A. Marković, L. Buschbeck, J. Christoffers, G. Wittstock; "Fluorescent dyes for electrochemical sensing – Electrochemical activation of self-assembled monolayers", 69th Annual Meeting of the International Society of Electrochemistry, Bologna, Italy, 2 Sep - 7 Sep 2018. (in English)

A. Marković, P. Sander, C. Dosche, R. Beckhaus G. Wittstock; "Electrochemical and spectroelectrochemical studies on electron transfer reactions of transition metal complexes with π -acceptor ligands", 69th Annual Meeting of the International Society of Electrochemistry, Bologna, Italy, 2 Sep - 7 Sep 2018. (in English)

11 Curriculum Vitae

Personal data

First and last name	Aleksandra Markovic
Date of birth	17.05.1991
Place of birth	Užice, Serbia
Nationality	Serbian
Languages	Serbian (mother tongue), English, German, Russian

School/Study/Scientific Qualification

04/2015 -	Graduate School "Interface Science", Carl von Ossietzky University Oldenburg
09/2014 – 09/2015	University of Belgrade, Faculty of Physical Chemistry, Master of Science (1 years of study, 60 ECTS), Master thesis "Theoretical analysis of non-metals adsorption on MgO/Mo(001) surface" (Advisor: Dr. Igor Pašti, Assistant Professor)
10/2010 – 06/2014	University of Belgrade, Faculty of Physical Chemistry, (Bachelor of Science 4 years of study, 240 ECTS), Bachelor thesis "Modification of the electrocatalytic activity of platinum due to the adsorption of acetonitrile - combined theoretical and experimental study" (Advisor: Dr. Igor Pašti, Assistant Professor)
09/2006 – 09/2010	High school "Užicka gimnazija", Užice

Scientific Employment within the University

04/2015 - 06/2015	Scientific coworker (Prof. Dr. Wittstock)
----------------------	---

06/2015 - Member of the graduate course Nanoenergy
Scientific coworker

Awards

03/2016 "Pavle Savic" for outstanding achievement in the BSc studies of physical chemistry awarded by Society of Physical Chemists of Serbia for generation 2010/2011

Own Participation in Teaching

12/2015-2/2017 Instructor for "Enzymatische Hydrolyse von Harnstoff" (basic electrochemical lab course for B.Sc. students)

12/2018-12/2018 Instructor for "Origin introduction course" (course for B.Sc. students)

Offices in Academic Self-Administration within the University

2012-2014 President of Student Parliament, Faculty of Physical Chemistry, Belgrade

2010-2014 Member of Student Parliament, Faculty of Physical Chemistry, Belgrade

12 References

- 1 Marcus, R. and Sutin, N. (1985) Electron transfers in chemistry and biology. *Biochim. Biophys. Acta*, **811**, 265–322.
- 2 Liu, J., Chakraborty, S., Hosseinzadeh, P., Yu, Y., Tian, S., Petrik, I., Bhagi, A., Lu, Y. (2014) Metalloproteins containing cytochrome, iron-sulfur, or copper redox centers. *Chem. Rev.*, **114** (8), 4366–4469.
- 3 D'Alessandro, D.M. and Keene, F.R. (2006) Intervalence charge transfer (IVCT) in trinuclear and tetranuclear complexes of iron, ruthenium, and osmium. *Chem. Rev.*, **106** (6), 2270–2298.
- 4 Ebersson, L. (1987) *Electron Transfer Reactions in Organic Chemistry*, Springer, Berlin.
- 5 Liu, J., Wang, J., Xu, C., Jiang, H., Li, C., Zhang, L., Lin, J., Shen, Z.X. (2018) Advanced Energy Storage Devices: Basic Principles, Analytical Methods, and Rational Materials Design. *Anal. Sci.*, **5** (1), 1700322(1-19).
- 6 Gratzel, M. (ed) (1983) *Energy Resources through Photochemistry and Catalysis*, Academic Press, Inc, New York.
- 7 Tippins, H.H. (1970) Charge-Transfer Spectra of Transition-Meta Ions in Corundum. *Phys. Rev. B*, **1**, 126–135.
- 8 Wasielewski, M.R. (1992) Photoinduced electron transfer in supramolecular systems for artificial photosynthesis. *Chem. Rev.*, **92**, 435–461.
- 9 Marcus, R.A. (1965) On the Theory of Chemiluminescent Electron-Transfer Reactions. *J. Phys. Chem.*, **43** (8), 2654–2657.
- 10 Betz, H.D. (1972) Charge States and Charge-Changing Cross Sections of Fast Heavy Ions Penetrating Through Gaseous and Solid Media. *Rev. Mod. Phys.*, **44**, 465–539.
- 11 Bard, A.J. (1983) Chemical modification of electrodes. *J. Chem. Educ.*, **60** (4), 302.
- 12 Marcus, R. and Sutin, N. (1985) Electron transfers in chemistry and biology. *Biochim. Biophys. Acta*, **811**, 265–322.
- 13 Moilanen, J.O., Chilton, N.F., Day, B.M., Pugh, T., Layfield, R.A. (2016) Strong Exchange Coupling in a Trimetallic Radical-Bridged Cobalt(II)-Hexaazatrinaphthylene Complex. *Angew. Chem. Int. Ed.*, **55** (18), 5521–5525.
- 14 Creutz, C. and Taube, H. (1973) Binuclear complexes of ruthenium amines. *J. Am. Chem. Soc.*, **95** (4), 1086–1094.
- 15 Richardson, D.E. and Taube, H. (1984) Mixed-valence molecules: Electronic delocalization and stability. *Coord. Chem. Rev.*, **60**, 107–129.
- 16 Demadis, K.D., Hartshorn, C.M., Meyer, T.J. (2001) The Localized-to-Delocalized Transition in Mixed-Valence Chemistry. *Chem. Rev.*, **101** (9), 2655–2686.
- 17 Rocha, R.C. and Toma, H.E. (2003) Linkage isomerism and redox properties of ruthenium-polypyridine benzotriazole complexes. *Transition Met. Chem.*, **28**, 43–50.
- 18 Kundu, T., Schweinfurth, D., Sarkar, B., Mondal, T.K., Fiedler, J., Mobin, S.M., Puranik, V.G., Kaim, W., Lahiri, G.K. (2012) Strong metal-metal coupling in mixed-valent intermediates $\text{Cl(L)Ru}(\mu\text{-tppz})\text{Ru(L)Cl}^+$, $\text{L} = \beta\text{-diketonato ligands}$, $\text{tppz} = 2,3,5,6\text{-tetrakis}(2\text{-pyridyl})\text{pyrazine}$. *Dalton Trans.*, **41** (43), 13429–13440.

- 19 Piglosiewicz, I.M., Beckhaus, R., Wittstock, G., Saak, W., Haase, D. (2007) Selective oxidation and reduction of trinuclear titanium(II) hexaazatrinaphthylene complexes-synthesis, structure, and electrochemical investigations. *Inorg. Chem.*, **46** (18), 7610–7620.
- 20 Segura, J.L., Juárez, R., Ramos, M., Seoane, C. (2015) Hexaazatriphenylene (HAT) derivatives: From synthesis to molecular design, self-organization and device applications. *Chem. Soc. Rev.*, **44** (19), 6850–6885.
- 21 Moilanen, J.O., Day, B.M., Pugh, T., Layfield, R.A. (2015) Open-shell doublet character in a hexaazatrinaphthylene trianion complex. *Chem. Commun.*, **51** (57), 11478–11481.
- 22 Kitagawa, S. and Masaoka, S. (2003) Metal complexes of hexaazatriphenylene (hat) and its derivatives—from oligonuclear complexes to coordination polymers. *Coord. Chem. Rev.*, **246** (1-2), 73–88.
- 23 Fangmann, P., Schmidtman, M., Beckhaus, R. (2018) Crystal structures of 2,3,8,9,14,15-hexamethyl-5,6,11,12,17,18-hexaazatrinaphthylene and 2,3,8,9,14,15-hexaphenyl-5,6,11,12,17,18-hexaazatrinaphthylene dichloromethane disolvate. *Acta Crystallogr. E Cryst. Commun.*, **74** (2), 167–171.
- 24 Lyaskovskyy, V. and Bruin, B. de (2012) Redox Non-Innocent Ligands: Versatile New Tools to Control Catalytic Reactions. *ACS Catal.*, **2** (2), 270–279.
- 25 Chirik, P.J. (2011) Preface: Forum on redox-active ligands. *Inorg. Chem.*, **50** (20), 9737–9740.
- 26 van der Vlugt, J.I. (2012) Cooperative Catalysis with First-Row Late Transition Metals. *Eur. J. Inorg. Chem.*, **2012** (3), 363–375.
- 27 Dzik, W.I., van der Vlugt, J.I., Reek, J.N.H., Bruin, B. de (2011) Ligands that store and release electrons during catalysis. *Angew. Chem. Int. Ed.*, **50** (15), 3356–3358.
- 28 Dzik, W.I., Zhang, X.P., Bruin, B. de (2011) Redox noninnocence of carbene ligands: Carbene radicals in (catalytic) C-C bond formation. *Inorg. Chem.*, **50** (20), 9896–9903.
- 29 Ghumaan, S., Sarkar, B., Patil, M.P., Fiedler, J., Sunoj, R.B., Kaim, W., Lahiri, G.K. (2007) Multiple one-electron oxidation and reduction of trinuclear bis(2,4-pentanedionato)ruthenium complexes with substituted diquinoxalino[2,3-a:2',3'-c]phenazine ligands. *Polyhedron*, **26** (13), 3409–3418.
- 30 Roy, S. and Kubiak, C.P. (2010) Tricarbonylrhenium(I) complexes of highly symmetric hexaazatrinaphthylene ligands (HATN): Structural, electrochemical and spectroscopic properties. *Dalton Trans.*, **39** (45), 10937–10943.
- 31 Sander, P., Marković, A., Schmidtman, M., Janka, O., Wittstock, G., Beckhaus, R. (2018) Synthesis, Crystal structures, Magnetic and Electrochemical Properties of Highly Phenyl substituted Trinuclear 5,6,11,12,17,18- Hexaazatrinaphthylene (HATNPh₆)-bridged Titanium Complexes. *Inorg. Chem.*, **57**, 11165–11174.
- 32 Chidsey, C.E.D. (1991) Free energy and temperature dependence of electron transfer at the metal-electrolyte interface. *Science*, **251**, 919–922.
- 33 Miller, C., Cuendt, P., Grätzel, M. (1991) Adsorbed omega-Hydroxy Thiol Monolayers on Gold Electrodes: Evidence for Electron Tunneling to Redox Species in Solution. *J. Phys. Chem.*, **95**, 877–886.
- 34 Finklea, H.O. (1996) Electrochemistry of organized monolayers of thiols and related molecules on electrodes, in *Electroanalytical Chemistry* (eds A.J. Bard and I. Rubinstein), Marcel Dekker, Inc., New York, Basel, Hong Kong, pp. 109–335.

- 35 Finklea, H.O. (2000) Self-assembled monolayers on electrodes, in *Encyclopedia of Analytical Chemistry* (ed R.A. Meyers), John Wiley & Sons Ltd, Chichester, pp. 1–10.
- 36 Gooding, J.J. and Ciampi, S. (2011) The molecular level modification of surfaces: From self-assembled monolayers to complex molecular assemblies. *Chem. Soc. Rev.*, **40** (5), 2704–2718.
- 37 Gooding, J.J. and Darwish, N. (2012) The Rise of Self-Assembled Monolayers for Fabricating Electrochemical Biosensors-An Interfacial Perspective. *Chem. Rec.*, **12** (1), 92–105.
- 38 Gooding, J.J., Erokhin, P., Losic, D., Yang, W., Policarpio, V., Liu, J., Ho, F.M., Situmorang, M., Hibbert, D.B., Shapter, J.G. (2001) Parameters Important in Fabricating Enzyme Electrodes Using Self-Assembled Monolayers of Alkanethiols. *Anal. Sci.*, **17** (1), 3–9.
- 39 Gooding, J.J. and Hibbert, D.B. (1999) The application of alkanethiol self-assembled monolayers to enzyme electrodes. *TrAC, Trends Anal. Chem.*, **18** (8), 525–533.
- 40 Gooding, J.J., Mearn, F., Yang, W., Liu, J. (2003) Self-Assembled Monolayers into the 21st Century: Recent Advances and Applications. *Electroanalysis*, **15**, 81–96.
- 41 Gooding, J.J. (2004) Alkanethiol self-assembled monolayers. *Encycl. Nanosci. Nanotechnol.*, **1**, 17–49.
- 42 Ulman, A. (1996) Formation and Structure of Self-Assembled Monolayers. *Chem. Rev.*, **96** (4), 1533–1554.
- 43 Zhang, X., Shi, F., Niu, J., Jiang, Y., Wang, Z. (2008) Superhydrophobic surfaces: From structural control to functional application. *J. Mater. Chem. A*, **18** (6), 621–633.
- 44 Laibinis, P.E., Whitesides, G.M., Allara, D.L., Tao, Y.T., Parikh, A.N., Nuzzo, R.G. (1991) Comparison of the structures and wetting properties of self-assembled monolayers of n-alkanethiols on the coinage metal surfaces, copper, silver, and gold. *J. Am. Chem. Soc.*, **113**, 7152–7167.
- 45 Bardea, A., Katz, E., Willner, I. (2000) Biosensors with Amperometric Detection of Enzymatically Controlled pH-Changes. *Electroanalysis*, **12** (10), 731–735.
- 46 Beulen, M.W.J., van Veggel, F.C.J.M., Reinhoudt, D.N. (1999) Coupling of acid–base and redox functions in mixed sulfide monolayers on gold. *Chem. Commun.* (6), 503–504.
- 47 Hickman, J.J., Ofer, D., Labinis, P.E., Whitesides, G.M., Wrlghton, M.S. (1991) Molecular Self-Assembly of Two-Terminal, Voltammetric Microsensors with Internal References. *Science*, **252**, 688–691.
- 48 Yang, W., Jaramillo, D., Gooding, J.J., Hibbert, D.B., Zhang, R., Willett, G.D., Fisher, K.J. (2001) Sub-ppt detection limits for copper ions with Gly-Gly-His modified electrodes. *Chem. Commun.* (19), 1982–1983.
- 49 Yang, W., Gooding, J.J., Hibbert, D.B. (2001) Redox voltammetry of sub-parts per billion levels of Cu²⁺ at polyaspartate-modified gold electrodes. *Analyst*, **126** (9), 1573–1577.
- 50 Yang, W., Justin Gooding, J., Brynn Hibbert, D. (2001) Characterisation of gold electrodes modified with self-assembled monolayers of l-cysteine for the adsorptive stripping analysis of copper. *J. Electroanal. Chem.*, **516** (1-2), 10–16.

- 51 Guiomar, A.J., Guthrie, J.T., Evans, S.D. (1999) Use of Mixed Self-Assembled Monolayers in a Study of the Effect of the Microenvironment on Immobilized Glucose Oxidase. *Langmuir*, **15** (4), 1198–1207.
- 52 Christoffers, J. (2018) Diaminoterephthalate Fluorescence Dyes - Versatile Tools for Life Sciences and Materials Science. *Eur. J. Org. Chem.*, **2018** (20-21), 2366–2377.
- 53 Smith, L.I. and Abler, R.L. (1957) On the Color of Diaminopyromellitic Esters and Related Compounds*. *J. Org. Chem.*, **22**, 811–816.
- 54 Ulbricht, H., Löber, G., Kittler, L. (1979) Synthese und π -Elektronenstruktur von 2,5-Bis-alkylamino-terephthalsäurediethylestern: H. Ulbricht, G. Löber, L. Kittler, *J. Prakt. Chem.* 1979, 321, 905–912. *J. Prakt. Chem.*, **321**, 905–912.
- 55 Kauffmann, H. and Weissel, L. (1912) Die Fluoreszenz in der Terephthalsäurereihe. *Justus Liebigs Ann. Chem.*, **393** (1–29).
- 56 Leupold, S., Shokati, T., Eberle, C., Borrmann, T., Montforts, F.-P. (2008) Synthesis of Porphyrin–Fullerene Dyads and Their Spectroscopic Properties. *Eur. J. Org. Chem.*, **2008** (15), 2621–2627.
- 57 Irngartinger, H., Fettel, P.W., Escher, T., Tinnefeld, P., Nord, S., Sauer, M. (2000) Substituent Effects on Redox Properties and Photoinduced Electron Transfer in Isoxazolo-Fullerenes. *Eur. J. Org. Chem.*, **2000** (3), 455–465.
- 58 Freimut, L., Rozzi, C.A., Lienau, C., Christoffers, J. (2015) A Diaminoterephthalate C60 Dyad - a New Material for Opto-Electronic Applications. *Synthesis*, **47**, 1325–1328.
- 59 Prato, M. and Maggini, M. (1998) Fulleropyrrolidines: A Family of Full-Fledged Fullerene Derivatives: *Acc. Chem. Res. Acc. Chem. Res.*, **31**, 519–526.
- 60 Pittalis, S., Delgado, A., Robin, J., Freimuth, L., Christoffers, J., Lienau, C., Rozzi, C.A. (2015) Charge Separation Dynamics and Opto-Electronic Properties of a Diaminoterephthalate-C 60 Dyad. *Adv. Funct. Mater.*, **25** (13), 2047–2053.
- 61 Gust, D., Moore, T.A., Moore, A.L. (2001) Mimicking Photosynthetic Solar Energy Transduction. *Anal. Chem.*, **34** (1), 40–48.
- 62 Scholes, G.D., Fleming, G.R., Olaya-Castro, A., van Grondelle, R. (2011) Lessons from nature about solar light harvesting. *Nat. Chem.*, **3** (10), 763–774.
- 63 Rozzi, C.A., Falke, S.M., Spallanzani, N., Rubio, A., Molinari, E., Brida, D., Maiuri, M., Cerullo, G., Schramm, H., Christoffers, J., Lienau, C. (2013) Quantum coherence controls the charge separation in a prototypical artificial light-harvesting system. *Nat. Commun.*, **4**, 1602.
- 64 Bard, A.J. and Faulkner, L.R. (2004) *Electrochemical Methods: Fundamentals and Applications*, 2nd edn, John Wiley & Sons.
- 65 Kipnis, N. (2006) Luigi Galvani and the debate on animal electricity, 1791–1800. *Ann. Sci.*, **44** (2), 107–142.
- 66 Piccolino, M. (2006) Luigi Galvani's path to animal electricity. *C. R. Biol.*, **329** (5-6), 303–318.
- 67 Gagne, R.R., Koval, C.A., Lisensky, G.C. (1980) Ferrocene as an internal standard for electrochemical measurements. *Inorg. Chem.*, **19**, 2854–2855.
- 68 Nicholson, R.S. (1965) Theory and Application of Cyclic Voltammetry for Measurement of Electrode Reaction Kinetics. *Anal. Chem.*, **37**, 1351–1355.
- 69 Wang, J. (2006) *Analytical electrochemistry*, 3rd edn, WILEY-VCH, Hoboken, NJ.

- 70 Echegoyen, L. and Echegoyen, L.E. (1998) Electrochemistry of Fullerenes and Their Derivatives. *Anal. Chem.*, **31** (9), 593–601.
- 71 Bard, A.J. and Rubinstein, I. (eds) (1996) *Electroanalytical Chemistry*, Marcel Dekker, Inc., New York, Basel, Hong Kong.
- 72 Maleki, A. and Nematollahi, D. (2013) Mechanism diversity in anodic oxidation of N,N-dimethyl-p-phenylenediamine by varying pH. *J. Electroanal. Chem.*, **704**, 75–79.
- 73 Adams, R.N., Hawley, M.D., Feldberg, S.W. (1967) Nuances of the E.C.E. mechanism. II. Addition of hydrochloric acid and amines to electrochemically generated o-benzoquinones. *J. Phys. Chem.*, **71**, 851–855.
- 74 Lawrence, N.S., Jiang, L., Jones, T.G.J., Compton, R.G. (2003) Voltammetric characterization of a N,N'-diphenyl-p-phenylenediamine-loaded screen-printed electrode: A disposable sensor for hydrogen sulfide. *Anal. Chem.*, **75** (9), 2054–2059.
- 75 Pandurangappa, M., Lawrence, N.S., Jiang, L., Jones, T.G.J., Compton, R.G. (2003) Physical adsorption of N,N'-diphenyl-p-phenylenediamine onto carbon particles: Application to the detection of sulfide. *Analyst*, **128** (5), 473–479.
- 76 Thompson, M., Lawrence, N.S., Davis, J., Jiang, L., Jones, T.G.J., Compton, R.G. (2002) A reagentless renewable N,N'-diphenyl-p-phenylenediamine loaded sensor for hydrogen sulfide. *Sens. Actuator B-Chem.*, **87** (1), 33–40.
- 77 Atkins, P.W., Overton, T.L., Rourke, J.P., Weller, M.T., Armstrong, F.A. (2010) *Shriver and Atkins' Inorganic Chemistry*, 5th edn, Oxford University Press, Oxford.
- 78 Murray, R.W. (1980) Chemically modified electrodes. *Acc. Chem. Res.*, **13**, 135–141.
- 79 Novak, M., Ebel, A., Meyer-Friedrichsen, T., Jedaa, A., Vieweg, B.F., Yang, G., Voitchovsky, K., Stellacci, F., Spiecker, E., Hirsch, A., Halik, M. (2011) Low-voltage p- and n-type organic self-assembled monolayer field effect transistors. *Nano Lett.*, **11** (1), 156–159.
- 80 Alkire, R.C., Kolb, D.M., Lipkowsky, J., Ross, P.N. (2009) *Advances in electrochemical science and engineering: Volume 11: Chemically modified electrodes*, WILEY-VCH, Weinheim.
- 81 Sagiv, J. (1980) Organized monolayers by adsorption. 1. Formation and structure of oleophobic mixed monolayers on solid surfaces. *J. Am. Chem. Soc.*, **102** (1), 92–98.
- 82 Nuzzo, R.G. and Allara, D.L. (1983) Adsorption of bifunctional organic disulfides on gold surfaces. *J. Am. Chem. Soc.*, **105**, 4481–4483.
- 83 Wang, M., Liechti, K.M., Wang, Q., White, J.M. (2005) Self-assembled silane monolayers: Fabrication with nanoscale uniformity. *Langmuir*, **21** (5), 1848–1857.
- 84 Nicosia, C. and Huskens, J. (2014) Reactive self-assembled monolayers: From surface functionalization to gradient formation. *Mater. Horiz.*, **1** (1), 32–45.
- 85 Choi, I., Kim, Y.K., Min, D.H., Lee, S.W., Yeo, W.S. (2011) On-demand electrochemical activation of the click reaction on self-assembled monolayers on gold presenting masked acetylene groups. *J. Am. Chem. Soc.*, **133** (42), 16718–16721.
- 86 Chaki, N.K. and Vijayamohan, K. (2002) Self-assembled monolayers as a tunable platform for biosensor applications. *Biosens. Bioelectron.*, **17** (1-2), 1–12.

- 87 Carroll, G.T., Pollard, M.M., van Delden, R., Feringa, B.L. (2010) Controlled rotary motion of light-driven molecular motors assembled on a gold film. *Chem. Sci.*, **1** (1), 97.
- 88 Ishizaki, T., Okido, M., Masuda, Y., Saito, N., Sakamoto, M. (2011) Corrosion resistant performances of alkanolic and phosphonic acids derived self-assembled monolayers on magnesium alloy AZ31 by vapor-phase method. *Langmuir*, **27** (10), 6009–6017.
- 89 Hosseinpour, S., Forslund, M., Johnson, C.M., Pan, J., Leygraf, C. (2016) Atmospheric corrosion of Cu, Zn, and Cu–Zn alloys protected by self-assembled monolayers of alkanethiols. *Surf. Sci.*, **648**, 170–176.
- 90 Halik, M. and Hirsch, A. (2011) The Potential of Molecular Self-Assembled Monolayers in Organic Electronic Devices. *Adv. Mater.*, **23** (22-23), 2689–2695.
- 91 Ahn, Y., Hong, S., Jang, J. (2006) Growth dynamics of self-assembled monolayers in dip-pen nanolithography. *J. Phys. Chem. B*, **110** (9), 4270–4273.
- 92 Gavutis, M., Navikas, V., Rakickas, T., Vaitekoniš, Š., Valiokas, R. (2016) Lipid dip-pen nanolithography on self-assembled monolayers. *J. Micromech. Microeng.*, **26** (2), 25016.
- 93 Eckermann, A.L., Feld, D.J., Shaw, J.A., Meade, T.J. (2010) Electrochemistry of redox-active self-assembled monolayers. *Coord. Chem. Rev.*, **254** (15-16), 1769–1802.
- 94 Laviron, E. (1979) General expression of the linear potential sweep voltammogram in the case of diffusionless electrochemical systems. *J. Electroanal. Chem.*, **101** (1), 19–28.
- 95 Yang, Z., Frey, W., Oliver, T., Chilkoti, A. (2000) Light-Activated Affinity Micropatterning of Proteins on Self-Assembled Monolayers on Gold. *Langmuir*, **16** (4), 1751–1758.
- 96 Frutos, A.G., Brockman, J.M., Corn, R.M. (2000) Reversible Protection and Reactive Patterning of Amine- and Hydroxyl-Terminated Self-Assembled Monolayers on Gold Surfaces for the Fabrication of Biopolymer Arrays. *Langmuir*, **16** (5), 2192–2197.
- 97 Kim, K., Yang, H., Kim, E., Han, Y.B., Kim, Y.T., Kang, S.H., Kwak, J. (2002) Electrochemical Deprotection for Site-Selective Immobilization of Biomolecules. *Langmuir*, **18** (5), 1460–1462.
- 98 Kim, K., Yang, H., Jon, S., Kim, E., Kwak, J. (2004) Protein patterning based on electrochemical activation of bioinactive surfaces with hydroquinone-caged biotin. *J. Am. Chem. Soc.*, **126** (47), 15368–15369.
- 99 Yousaf, M.N. and Mrksich, M. (1999) Diels–Alder Reaction for the Selective Immobilization of Protein to Electroactive Self-Assembled Monolayers. *J. Am. Chem. Soc.*, **121** (17), 4286–4287.
- 100 Kwon, Y. and Mrksich, M. (2002) Dependence of the Rate of an Interfacial Diels–Alder Reaction on the Steric Environment of the Immobilized Dienophile: An Example of Enthalpy–Entropy Compensation. *J. Am. Chem. Soc.*, **124** (5), 806–812.
- 101 Gawalt, E.S. and Mrksich, M. (2004) A substituent effects study reveals the kinetic pathway for an interfacial reaction. *J. Am. Chem. Soc.*, **126** (47), 15613–15617.
- 102 Shamsipur, M., Kazemi, S.H., Alizadeh, A., Mousavi, M.F., Workentin, M.S. (2007) Self-assembled monolayers of a hydroquinone-terminated alkanethiol onto

- gold surface. Interfacial electrochemistry and Michael-addition reaction with glutathione. *J. Electroanal. Chem.*, **610** (2), 218–226.
- 103 Vickerman, J.C. and Gilmore, I.S. (2009) *Surface analysis: the principal techniques*, Wiley Online Library.
- 104 The Nobel Prize in Physics 1901.
<https://www.nobelprize.org/prizes/physics/1901/summary/> (2 November 2018).
- 105 The Nobel Prize in Physics 1914.
<https://www.nobelprize.org/prizes/physics/1914/summary/> (2 November 2018).
- 106 The Nobel Prize in Physics 1981.
<https://www.nobelprize.org/prizes/physics/1981/summary/> (2 November 2018).
- 107 The Nobel Prize in Physics 1924.
<https://www.nobelprize.org/prizes/physics/1924/siegbahn/facts/> (17 November 2018).
- 108 The Nobel Prize in Physics 1921.
<https://www.nobelprize.org/prizes/physics/1921/summary/> (2 November 2018).
- 109 Koopmans T. (1934) Über die Zuordnung von Wellenfunktionen und Eigenwerten zu den Einzelnen Elektronen eines Atoms. *Physica*, **1**, 104–113.
- 110 Scofield, J.H. (1976) Hartree-Slater subshell photoionization cross-sections at 1254 and 1487 eV. *J. Electron Spectros. Relat. Phenomena*, **8**, 129–137.
- 111 Yamamoto, H., Butera, R.A., Gu, Y., Waldeck, D.H. (1999) Characterization of the Surface to Thiol Bonding in Self-Assembled Monolayer Films of C₁₂H₂₅SH on InP(100) by Angle-Resolved X-ray Photoelectron Spectroscopy. *Langmuir*, **15** (25), 8640–8644.
- 112 Dannenberger, O., Weiss, K., Wöll, C., Buck, M. (2000) Reactivity of self-assembled monolayers: Formation of organized amino functionalities. *Phys. Chem. Chem. Phys.*, **2** (7), 1509–1514.
- 113 Clegg, R.S. and Hutchison, J.E. (1999) Control of Monolayer Assembly Structure by Hydrogen Bonding Rather Than by Adsorbate–Substrate Templating. *J. Am. Chem. Soc.*, **121** (22), 5319–5327.
- 114 Paul E. Laibinis, Colin D. Bain, and George M. Whitesides (1991) Attenuation of photoelectrons in monolayers of n-alkanethiols adsorbed on copper, silver, and gold. *J. Phys. Chem.*, **95**, 7017–7021.
- 115 Lamont, C.L.A. and Wilkes, J. (1999) Attenuation Length of Electrons in Self-Assembled Monolayers of n -Alkanethiols on Gold. *Langmuir*, **15** (6), 2037–2042.
- 116 Tamada, K., Ishida, T., Knoll, W., Fukushima, H., Colorado, R., Graupe, M., Shmakova, O.E., Lee, T.R. (2001) Molecular Packing of Semifluorinated Alkanethiol Self-Assembled Monolayers on Gold: Influence of Alkyl Spacer Length. *Langmuir*, **17** (6), 1913–1921.
- 117 Ishida, T., Mizutani, W., Tokumoto, H., Choi, N., Akiba, U., Fujihira, M. (2000) Insertion process and electrical conduction of conjugated molecules in n-alkanethiol self-assembled monolayers on Au(111). *J. Vac. Sci. Technol. A*, **18** (4), 1437–1442.
- 118 Harder, P., Grunze, M., Dahint, R., Whitesides, G.M., Laibinis, P.E. (1998) Molecular Conformation in Oligo(ethylene glycol)-Terminated Self-Assembled Monolayers on Gold and Silver Surfaces Determines Their Ability To Resist Protein Adsorption. *J. Phys. Chem. B*, **102** (2), 426–436.

- 119 Laibinis, P.E., Graham, R.L., Biebuyck, H.A., Whitesides, G.M. (1991) X-ray Damage to CF₃CO₂-Terminated Organic Monolayers on Si/Au: Principal Effect of Electrons. *Science*, **254**, 981–983.
- 120 Graham, R.L., Bain, C.D., Biebuyck, H.A., Laibinis, P.E., Whitesides, G.M. (1993) Damage to trifluoroacetamido-terminated organic self-assembled monolayers (SAMs) on aluminum, titanium, copper and Au by Al K_α X-rays is due principally to electrons. *J. Phys. Chem.*, **97**, 9456–9464.
- 121 Wirde, M., Gelius, U., Dunbar, T., Allara, D.L. (1997) Modification of self-assembled monolayers of alkanethiols on gold by ionizing radiation. *Nucl. Instr. Meth. Phys. Res. B*, **131** (1-4), 245–251.
- 122 Müller, H.U., Zharnikov, M., Völkel, B., Schertel, A., Harder, P., Grunze, M. (1998) Low-Energy Electron-Induced Damage in Hexadecanethiolate Monolayers. *J. Phys. Chem. B*, **102** (41), 7949–7959.
- 123 Murty, K.V.G.K., Venkataramanan, M., Pradeep, T. (1998) Self-assembled Monolayers of 1,4-Benzenedimethanethiol on Polycrystalline Silver and Gold Films: An Investigation of Structure, Stability, Dynamics, and Reactivity. *Langmuir*, **14**, 5446–5456.
- 124 Zharnikov, M., Geyer, W., Götzhäuser, A., Frey, S., Grunze, M. (1999) Modification of alkanethiolate monolayers on Au-substrate by low energy electron irradiation: Alkyl chains and the S/Au interface. *Phys. Chem. Chem. Phys.*, **1**, 3163–3171.
- 125 Heister, K., Frey, S., Götzhäuser, A., Ulman, A., Zharnikov, M. (1999) An Enhanced Sensitivity of Alkanethiolate Self-Assembled Monolayers to Electron Irradiation through the Incorporation of a Sulfide Entity into the Alkyl Chains. *J. Phys. Chem. B*, **103** (50), 11098–11104.
- 126 Zharnikov, M., Frey, S., Rong, H., Yang, Y.-J., Heister, K., Buck, M., Grunze, M. (2000) The effect of sulfur–metal bonding on the structure of self-assembled monolayers. *Phys. Chem. Chem. Phys.*, **2** (15), 3359–3362.
- 127 Castner, D.G., Hinds, K., Grainger, D.W. (1996) X-ray Photoelectron Spectroscopy Sulfur 2p Study of Organic Thiol and Disulfide Binding Interactions with Gold Surfaces. *Langmuir*, **12** (21), 5083–5086.
- 128 Zubrägel, C., Deuper, C., Schneider, F., Neumann, M., Grunze, M., Schertel, A., Wöll, C. (1995) The presence of two different sulfur species in self-assembled films of n-alkanethiols on Au and Ag surfaces. *Chem. Phys. Lett.*, **238** (4-6), 308–312.
- 129 Heister, K., Zharnikov, M., Grunze, M., Johansson, L.S.O., Ulman, A. (2001) Characterization of X-ray Induced Damage in Alkanethiolate Monolayers by High-Resolution Photoelectron Spectroscopy. *Langmuir*, **17** (1), 8–11.
- 130 Bruns, M., Barth, C., Brüner, P., Engin, S., Grehl, T., Howell, C., Koelsch, P., Mack, P., Nagel, P., Trouillet, V., Wedlich, D., White, R.G. (2012) Structure and chemical composition of mixed benzylguanine- and methoxy-terminated self-assembled monolayers for immobilization of biomolecules. *Surf. Interface Anal.*, **44** (8), 909–913.
- 131 Lippert, R.J., Lamp, B.D., Porter, M.D. (1998) Specular Reflection Spectroscopy, in *Modern techniques in Applied Molecular Spectroscopy* (ed F.M. Mirabella), John Wiley and Sons, Inc., New York, pp. 83–126.
- 132 Greenler, R.G. (1969) Reflection Method for Obtaining the Infrared Spectrum of a Thin Layer on a Metal Surface. *J. Chem. Phys.*, **50** (5), 1963–1968.

- 133 Francis, S.A. and Ellison, A. H. (1959) Infrared Spectra of Monolayers on Metal Mirrors. *J. Opt. Soc. Am.*, **49**, 131–138.
- 134 Hayden B.E. (1987) *Reflection Absorption Infrared Spectroscopy*, Springer, Boston, MA.
- 135 Pearce, H.A. and Sheppard, N. (1976) Possible importance of a "metal-surface selection rule" in the interpretation of the infrared spectra of molecules adsorbed on particulate metals; infrared spectra from ethylene chemisorbed on silica-supported metal catalysts. *Surf. Sci.*, **59** (1), 205–217.
- 136 Ulrich, W.-P. and Vogel, H. (1999) Polarization-Modulated FTIR Spectroscopy of Lipid/Gramicidin Monolayers at the Air/Water Interface. *Biophys. J.*, **76** (3), 1639–1647.
- 137 McIntyre, J.D.E. and Aspnes, D.E. (1971) Differential reflection spectroscopy very thin surface films. *Surf. Sci.*, **24**, 417–434.
- 138 Buffeteau, T., Desbat, B., Turlet, J.M. (1991) Polarisation Modulation FT-IR Spectroscopy of Surfaces and Ultra-thin Films: Experimental Procedure and Quantitative Analysis. *Appl. Spectrosc.*, **45** (3), 380–388.
- 139 Armarego, W.L.F. and Perrin, D.D. (1988) *Purification of Laboratory Chemicals*, Pergamon Press, Oxford.
- 140 Buschbeck, L. (2018) Diaminoterephthalsäurederivate als bifunktionelle Fluoreszenzfarbstoffe. Carl von Ossietzky University of Oldenburg. PhD thesis.
- 141 Freimuth, L. (2016) Studien zur Synthese von fluoreszierenden Diaminoterephthalsäurederivaten zur Anwendung in den Life Sciences und der Materials Science. Carl von Ossietzky University of Oldenburg. PhD thesis.
- 142 Ahlers, M. (2013) Electrochemical and Spectroscopic Analysis of Collagen Films and Lipid Bilayers on Biomaterial Surfaces. Carl von Ossietzky University of Oldenburg. PhD Thesis.
- 143 S. Herzog, S. and Taube, R. (1960) Über Komplexverbindungen des 2,2'-Dipyridyls mit bisher unbekanntem niedrigen Oxydationsstufen des Titans: Ti(0) und Ti(-I). *Z. Anorg. Allg. Chem.*, **306**, 159–179.
- 144 Hush, N.S. (1985) Distance dependence of electron transfer rates. *Coord. Chem. Rev.*, **64**, 135–167.
- 145 Madoz, J., Kuznetsov, B.A., Medrano, F.J., Garcia, J.L., Fernandez, V.M. (1997) Functionalization of Gold Surfaces for Specific and Reversible Attachment of a Fused β -Galactosidase and Choline-Receptor Protein. *J. Am. Chem. Soc.*, **119** (5), 1043–1051.
- 146 Burke, L.D. and Nugent, P.F. (1997) The electrochemistry of gold: I the redox behaviour of the metal in aqueous media. *Gold Bulletin*, **30** (2), 43–53.
- 147 Desimoni, E. and Brunetti, B. (2015) X-Ray Photoelectron Spectroscopic Characterization of Chemically Modified Electrodes Used as Chemical Sensors and Biosensors: A Review. *Chemosensors*, **3** (2), 70–117.
- 148 Gardella, J.A., Ferguson, S.A., Chin, R.L. (1986) $\pi^* \leftarrow \pi$ Shakeup Satellites for the Analysis of Structure and Bonding in Aromatic Polymers by X-Ray Photoelectron Spectroscopy. *Appl Spectrosc*, **40** (2), 224–232.
- 149 Lopez, G.P., Castner, D.G., Ratner, B.D. (1991) XPS O 1s binding energies for polymers containing hydroxyl, ether, ketone and ester groups. *Surf. Interface Anal.*, **17**, 267–277.

- 150 Zhang, X. and Ptasinska, S. (2014) Dissociative Adsorption of Water on an H₂O/GaAs(100) Interface: In Situ Near-Ambient Pressure XPS Studies. *J. Phys. Chem. C*, **118** (8), 4259–4266.
- 151 Duwez, A.-S. (2004) Exploiting electron spectroscopies to probe the structure and organization of self-assembled monolayers: A review. *J. Electron Spectros. Relat. Phenomena*, **134** (2-3), 97–138.
- 152 Han, M.G. and Im, S.S. (2000) X-ray photoelectron spectroscopy study of electrically conducting polyaniline/polyimide blends. *Polymer*, **41** (9), 3253–3262.
- 153 Günzler, H. and Gremlich, H.-U. (2002) *IR Spectroscopy: An Introduction*, WILEY-VCH, Weinheim.
- 154 Hesse, M., Meier, H., Zeeh, B. (1991) *Spektroskopische Methoden in der organischen Chemie*, 4th edn, Georg Thieme Verlag, Stuttgart, New York.
- 155 Lee, S., Shon, Y.-S., Colorado, R., Guenard, R.L., Lee, T.R., Perry, S.S. (2000) The Influence of Packing Densities and Surface Order on the Frictional Properties of Alkanethiol Self-Assembled Monolayers (SAMs) on Gold: A Comparison of SAMs Derived from Normal and Spiroalkanedithiols. *Langmuir*, **16** (5), 2220–2224.
- 156 Arnold, R., Terfort, A., Wöll, C. (2001) Determination of Molecular Orientation in Self-Assembled Monolayers Using IR Absorption Intensities: The Importance of Grinding Effects. *Langmuir*, **17** (16), 4980–4989.
- 157 Vericat, C., Vela, M.E., Benitez, G., Carro, P., Salvarezza, R.C. (2010) Self-assembled monolayers of thiols and dithiols on gold: New challenges for a well-known system. *Chem. Soc. Rev.*, **39** (5), 1805–1834.
- 158 Park, J.-S., Vo, A.N., Barriet, D., Shon, Y.-S., Lee, T.R. (2005) Systematic control of the packing density of self-assembled monolayers using bidentate and tridentate chelating alkanethiols. *Langmuir*, **21** (7), 2902–2911.
- 159 Colorado, R., Villazana, R.J., Lee, T.R. (1998) Self-Assembled Monolayers on Gold Generated from Aliphatic Dithiocarboxylic Acids. *Langmuir*, **14** (22), 6337–6340.
- 160 Premkumar, S., Jawahar, A., Mathavan, T., Kumara Dhas, M., Sathe, V.G., Milton Franklin Benial, A. (2014) DFT calculation and vibrational spectroscopic studies of 2-(tert-butoxycarbonyl (Boc) -amino)-5-bromopyridine. *Spectrochim. Acta A*, **129**, 74–83.
- 161 Korppi-Tommola, J. (1978) Tert-butyl alcohol-matrix i.r. spectra and vibrational assignment. *Spectrochim. Acta*, **34A**, 1077–1085.
- 162 Longhi, G., Zerbi, G., Ricard, L., Abbate, S. (1988) Electric dipole moment functions from vibrational absorption intensities of fundamental and overtone transitions. *J. Chem. Phys.*, **88** (11), 6733–6741.
- 163 van Meervelt, L., Wael, K. de, Zeegers-Huyskens, V. (1995) X-ray and IR studies of N-(tert-butoxycarbonyl)-L-alanine. Comparison with N-(tert-butoxycarbonyl)glycine. *J. Mol. Struct.*, **356**, 183–190.
- 164 Chinwangso, P., Lee, H.J., Lee, T.R. (2015) Self-Assembled Monolayers Generated from Unsymmetrical Partially Fluorinated Spiroalkanedithiols. *Langmuir*, **31** (49), 13341–13349.
- 165 Robinson, G.N., Freedman, A., Graham, R.L. (1995) Reactions of Fluorine Atoms with Self-Assembled Monolayers of Alkanethiolates. *Langmuir*, **11**, 2600–2608.

- 166 Ford, K., Battersby, B.J., Wood, B.J., Gentle, I.R. (2012) The production and verification of pristine semi-fluorinated thiol monolayers on gold. *J. Colloid Interface Sci.*, **370** (1), 162–169.
- 167 Ishida, A. and Majima, T. (2000) Surface plasmon enhanced fluorescence measurement on flat and constructed gold surfaces. *Analyst*, **125** (3), 535–540.
- 168 Imahori, H., Norieda, H., Ozawa, S., Ushida, K., Yamada, H., Azuma, T., Tamaki, K., Sakata, Y. (1998) Chain Length Effect on Photocurrent from Polymethylene-Linked Porphyrins in Self-Assembled Monolayers. *Langmuir*, **14** (19), 5335–5338.

Ich versichere hiermit, dass ich diese Arbeit selbstständig verfasst und nur die angegebenen Quellen und Hilfsmittel benutzt habe. Während der Dissertation sind die unter "Publications" aufgelisteten Veröffentlichungen entstanden. Die Dissertation hat weder zu Teilen noch in Gänze einer anderen wissenschaftlichen Hochschule zur Begutachtung in einem Promotionsverfahren vorgelegen.

Oldenburg, den 27.03.2019

Aleksandra Marković